



AFRL-RB-WP-TR-2008-3033

A HIGH-ORDER COMPACT FINITE-DIFFERENCE SCHEME FOR LARGE-EDDY SIMULATION OF ACTIVE FLOW CONTROL

Donald P. Rizzetta, Miguel R. Visbal, and Philip E. Morgan

**Computational Sciences Branch
Aeronautical Sciences Division**

**JANUARY 2008
Final Report**

Approved for public release; distribution unlimited.

See additional restrictions described on inside pages

STINFO COPY

**AIR FORCE RESEARCH LABORATORY
AIR VEHICLES DIRECTORATE
WRIGHT-PATTERSON AIR FORCE BASE, OH 45433-7542
AIR FORCE MATERIEL COMMAND
UNITED STATES AIR FORCE**

NOTICE AND SIGNATURE PAGE

Using Government drawings, specifications, or other data included in this document for any purpose other than Government procurement does not in any way obligate the U.S. Government. The fact that the Government formulated or supplied the drawings, specifications, or other data does not license the holder or any other person or corporation; or convey any rights or permission to manufacture, use, or sell any patented invention that may relate to them.

This report was cleared for public release by the Air Force Research Laboratory Wright-Patterson Air Force Base (AFRL/WPAFB) Public Affairs Office and is available to the general public, including foreign nationals. Copies may be obtained from the Defense Technical Information Center (DTIC) (<http://www.dtic.mil>).

AFRL-RB-WP-TR-2008-3033 HAS BEEN REVIEWED AND IS APPROVED FOR PUBLICATION IN ACCORDANCE WITH ASSIGNED DISTRIBUTION STATEMENT.

//Signature//

MIGUEL R. VISBAL, Technical Area Leader
Computational Sciences Branch
Aeronautical Sciences Division

//Signature//

REID B. MELVILLE, Chief
Computational Sciences Branch
Aeronautical Sciences Division

//Signature//

MATTHEW BURKINSHAW, Technical Advisor
Computational Sciences Branch
Aeronautical Sciences Division

This report is published in the interest of scientific and technical information exchange, and its publication does not constitute the Government's approval or disapproval of its ideas or findings.

*Disseminated copies will show “//Signature//” stamped or typed above the signature blocks.

REPORT DOCUMENTATION PAGE				<i>Form Approved</i> OMB No. 0704-0188				
The public reporting burden for this collection of information is estimated to average 1 hour per response, including the time for reviewing instructions, searching existing data sources, gathering and maintaining the data needed, and completing and reviewing the collection of information. Send comments regarding this burden estimate or any other aspect of this collection of information, including suggestions for reducing this burden, to Department of Defense, Washington Headquarters Services, Directorate for Information Operations and Reports (0704-0188), 1215 Jefferson Davis Highway, Suite 1204, Arlington, VA 22202-4302. Respondents should be aware that notwithstanding any other provision of law, no person shall be subject to any penalty for failing to comply with a collection of information if it does not display a currently valid OMB control number. PLEASE DO NOT RETURN YOUR FORM TO THE ABOVE ADDRESS.								
1. REPORT DATE (DD-MM-YY) January 2008		2. REPORT TYPE Final		3. DATES COVERED (From - To) 22 April 1997 – 23 April 2005				
4. TITLE AND SUBTITLE A HIGH-ORDER COMPACT FINITE-DIFFERENCE SCHEME FOR LARGE-EDDY SIMULATION OF ACTIVE FLOW CONTROL				5a. CONTRACT NUMBER In-house				
				5b. GRANT NUMBER				
				5c. PROGRAM ELEMENT NUMBER 0601102				
6. AUTHOR(S) Donald P. Rizzetta, Miguel R. Visbal, and Philip E. Morgan				5d. PROJECT NUMBER A04Y				
				5e. TASK NUMBER				
				5f. WORK UNIT NUMBER 0B				
7. PERFORMING ORGANIZATION NAME(S) AND ADDRESS(ES) Computational Sciences Branch (AFRL/RBAC) Aeronautical Sciences Division Air Force Research Laboratory, Air Vehicles Directorate Wright-Patterson Air Force Base, OH 45433-7542 Air Force Materiel Command, United States Air Force				8. PERFORMING ORGANIZATION REPORT NUMBER AFRL-RB-WP-TR-2008-3033				
9. SPONSORING/MONITORING AGENCY NAME(S) AND ADDRESS(ES) Air Force Research Laboratory Air Vehicles Directorate Wright-Patterson Air Force Base, OH 45433-7542 Air Force Materiel Command United States Air Force				10. SPONSORING/MONITORING AGENCY ACRONYM(S) AFRL/RBAC				
				11. SPONSORING/MONITORING AGENCY REPORT NUMBER(S) AFRL-RB-WP-TR-2008-3033				
12. DISTRIBUTION/AVAILABILITY STATEMENT Approved for public release; distribution unlimited.								
13. SUPPLEMENTARY NOTES PAO Case Number: WPAFB 07-0786, 27 Dec 2007. Report contains color.								
14. ABSTRACT A computational approach for performing large-eddy simulation (LES) of flows with active control is summarized. Simulation of these problems typically characterized by small-scale fluid structures cannot be carried out accurately by methods less sophisticated than LES. The numerical scheme is predicated upon an implicit time-marching algorithm, and utilizes a high order compact finite-difference approximation to represent spatial derivatives. Robustness of the scheme is maintained by employing a low-pass Pade-type non-dispersive spatial filter, which also serves as an implicit sub-grid turbulent model. Geometrically complex applications are accommodated by a high order overset grid technique. Utility of the method is illustrated by steady and pulsed approaches to suppression of acoustic resonance in supersonic cavity flow, leading-edge vortex control of a delta wing, efficiency enhancement of a transitional highly loaded low-pressure turbine blade, and separation control of a wall-mounted hump model. Where available, comparisons are also made with experimental data.								
15. SUBJECT TERMS								
16. SECURITY CLASSIFICATION OF: <table border="1" style="width: 100%; border-collapse: collapse; margin-top: 5px;"> <tr> <td style="padding: 2px;">a. REPORT Unclassified</td> <td style="padding: 2px;">b. ABSTRACT Unclassified</td> <td style="padding: 2px;">c. THIS PAGE Unclassified</td> </tr> </table>			a. REPORT Unclassified	b. ABSTRACT Unclassified	c. THIS PAGE Unclassified	17. LIMITATION OF ABSTRACT: SAR		18. NUMBER OF PAGES 108
a. REPORT Unclassified	b. ABSTRACT Unclassified	c. THIS PAGE Unclassified						
19a. NAME OF RESPONSIBLE PERSON (Monitor) Miguel R. Visbal 19b. TELEPHONE NUMBER (Include Area Code) N/A								

Table of Contents

List of Figures	iv
List of Tables	v
Acknowledgements	vi
1 Introduction	1
2 The Governing Equations	2
3 The Numerical Method	4
3.1 The Time Marching Scheme	4
3.2 The Compact Finite-Difference Scheme	4
3.3 The Compact Filtering Scheme	6
3.4 The Overset Grid Approach	7
3.5 The LES Approach	9
3.6 Validation of the Numerical Method	9
4 Empirical Plasma Model	11
5 Acoustic Suppression of Supersonic Cavity Flow	12
5.1 Features of the Time-Mean Flowfields	13
5.2 Features of the Unsteady Flowfields	13
5.3 Comparison with Experimental Data	14
6 Leading-Edge Vortex Control on a Delta Wing	16
6.1 Results for AOA=34 deg	16
6.2 Results for AOA=38 deg	17
7 Efficiency Enhancement for Highly Loaded Low-Pressure Turbine Blades	18
7.1 Results for Vortex-Generating Jets	19
7.2 Results for Plasma-Based Control	20
8 Separation Control for a Wall-Mounted Hump Model	23
8.1 Features of the Time-Mean Flowfields	23
8.2 Features of the Unsteady Flowfields	24
9 Summary and Conclusion	25
10 References	92
List of Symbols	97

List of Figures

1	Dispersion-error characteristics of various spatial discretizations for one-dimensional periodic functions.	26
2	Dissipation-error characteristics of various filters for one-dimensional periodic functions. . . .	27
3	Dissipation-error characteristics with various values of the implicit coefficient α_f and a 10th-order filter for one-dimensional periodic functions.	28
4	Schematic illustration of five-point mesh overlap.	29
5	Schematic representation of plasma actuator.	30
6	Geometry for the empirical plasma-force model.	31
7	Schematic representation of the cavity configuration.	32
8	Experimental cavity configuration.	33
9	Spanwise-averaged time-mean pressure coefficient contours.	34
10	Spanwise-averaged time-mean pressure coefficient distributions on the cavity floor.	35
11	Spanwise-averaged time-mean steamwise velocity contours.	36
12	Spanwise-averaged time-mean steamwise velocity profiles.	37
13	Spanwise-averaged time-mean turbulent kinetic energy contours.	38
14	Time-mean turbulent kinetic energy spanwise wave-number spectra at $x = 0.2, 0.5, 0.8$ and $y = 0.2\delta_0/l$	39
15	Spanwise-averaged time-mean fluctuating pressure contours.	40
16	Spanwise-averaged time-mean fluctuating pressure profiles.	41
17	Instantaneous Mach number contours at the midspan location.	42
18	Instantaneous spanwise vorticity contours at the midspan location for $t = t_1$	43
19	Instantaneous spanwise vorticity contours at the midspan location for $t = t_2$	44
20	Instantaneous spanwise vorticity contours at the midspan location for $t = t_3$	45
21	Instantaneous spanwise vorticity contours at the midspan location for $t = t_4$	46
22	Spanwise-averaged turbulent kinetic energy frequency spectra at $x = 0.2, 0.5, 0.8$ and $y = 0.2\delta_0/l$	47
23	Instantaneous total pressure coefficient contours and iso-surface.	48
24	Spanwise-averaged fluctuating pressure frequency spectra on the cavity rear bulkhead at $y = -0.04$	49
25	Spanwise-averaged fluctuating pressure frequency spectra on the cavity floor at $x = 0.2$	50
26	Spanwise-averaged fluctuating pressure frequency spectra on the cavity floor at $x = 0.5$	51
27	Spanwise-averaged fluctuating pressure frequency spectra on the cavity floor at $x = 0.8$	52
28	Schematic representation of delta wing actuator locations and flow features.	53
29	Time history of vortex breakdown location for $Re=25,000$ and $AOA=34$ deg.	54
30	Instantaneous planar contours through the vortex core for $Re=25,000$ and $AOA=34$ deg: (a) and (d) pressure coefficient, (b) and (e) streamwise velocity, (c) and (f) streamwise vorticity.	55
31	Instantaneous planar contours for $Re=25,000$ and $AOA=34$ deg: (a) streamwise vorticity, (b) streamwise velocity.	56
32	Instantaneous iso-surfaces for $Re=25,000$ and $AOA=34$ deg: (a), (b), (d), and (e) streamwise vorticity, (c) and (f) total pressure.	57
33	Time-mean flow quantities for $Re=25,000$ and $AOA=34$ deg: (a) and (d) planar contours of streamwise velocity through the vortex core, (b) and (e) planar contours of rms streamwise velocity fluctuations through the vortex core, (c) and (f) iso-surface of streamwise vorticity.	58
34	Instantaneous planar contours through the vortex core for $Re=25,000$ and $AOA=38$ deg: (a) and (c) streamwise velocity, (b) and (d) streamwise vorticity.	59
35	Instantaneous iso-surfaces at $AOA=38$ deg: (a) and (c) streamwise vorticity for $Re=25,000$, (b) and (d) total pressure for $Re=9,200$	60
36	Schematic representation of the turbine blade configuration.	61
37	Turbine blade computational mesh system.	62
38	Duty cycle amplitude time history.	63
39	Vortex generator jet geometry and mesh system.	64
40	Time-mean surface pressure coefficient distributions for vortex-jet control.	65
41	Time-mean planar contours for vortex-jet control: a) streamwise velocity, b) spanwise vorticity.	66

42	Time-mean turbulent kinetic energy spanwise wave-number spectra for vortex-jet control. . .	67
43	Instantaneous planar contours for vortex-jet control: a) streamwise velocity, b) spanwise vorticity.	68
44	Turbulent kinetic energy frequency spectra for vortex-jet control.	69
45	Instantaneous iso-surfaces of vorticity magnitude in the trailing-edge region for vortex-jet control.	70
46	Plasma actuator configurations.	71
47	Time-mean surface pressure coefficient distributions for plasma control.	72
48	Time-mean results for plasma control: contours of streamwise velocity (top row), streamlines (middle row), contours of C_p (bottom row).	73
49	Time-mean turbulent kinetic energy spanwise wave-number spectra for plasma control.	74
50	Instantaneous streamlines at the midspan for plasma control with configuration A	75
51	Instantaneous contours for plasma control: streamwise velocity (top row), spanwise vorticity (middle row), spanwise vorticity on the blade surface (bottom row).	76
52	Turbulent kinetic energy frequency spectra for plasma control.	77
53	Instantaneous iso-surfaces of vorticity magnitude colored by streamwise velocity in the trailing-edge region for plasma control.	78
54	Computational mesh system for wall-mounted hump.	79
55	Time-mean surface pressure coefficient distributions.	80
56	Time-mean streamwise velocity contours for the baseline case: LES (top), RANS (middle), experiment (bottom).	81
57	Time-mean streamwise velocity contours for the suction case: LES (top), RANS (middle), experiment (bottom).	82
58	Time-mean streamwise velocity contours for the oscillating blowing/suction case: LES (top), RANS (middle), experiment (bottom).	83
59	Time-mean Reynolds stress contours for the baseline case: LES (top), RANS (middle), experiment (bottom).	84
60	Time-mean Reynolds stress contours for the suction case: LES (top), RANS (middle), experiment (bottom).	85
61	Time-mean Reynolds stress contours for the oscillating blowing/suction case: LES (top), RANS (middle), experiment (bottom).	86
62	Phase-averaged spanwise vorticity contours at $\Theta=0$ deg for the oscillating blowing/suction case: LES (top), RANS (middle), experiment (bottom).	87
63	Phase-averaged spanwise vorticity contours at $\Theta=90$ deg for the oscillating blowing/suction case: LES (top), RANS (middle), experiment (bottom).	88
64	Phase-averaged spanwise vorticity contours at $\Theta=180$ deg for the oscillating blowing/suction case: LES (top), RANS (middle), experiment (bottom).	89
65	Phase-averaged spanwise vorticity contours at $\Theta=270$ deg for the oscillating blowing/suction case: LES (top), RANS (middle), experiment (bottom).	90
66	Instantaneous contours of streamwise velocity and iso-surface of vorticity magnitude for the oscillating blowing/suction case.	91

List of Tables

1	Cavity flow conditions	12
2	Hump flow reattachment locations	23

Acknowledgements

All of the work reported here was sponsored by the U. S. Air Force Office of Scientific Research. Computational resources were supported in part by grants of supercomputer time from the U. S. Department of Defense Major Shared Resource Centers at Wright-Patterson AFB, OH, Vicksburg, MS, Stennis Space Center, MS, and Aberdeen Proving Ground, MD. The authors are indebted to a number of their co-workers for assistance provided in this effort, who include D. V. Gaitonde, J. Poggie, and S. E. Sherer.

1 Introduction

Due to severe resolution requirements resulting in excessive expenditure of computational resources, direct numerical simulation (DNS) of turbulent flows is generally limited to relatively low Reynolds numbers and to simple geometric configurations. In order to reduce these demands, particularly for practical applications, it is desirable to model certain aspects of the turbulence in some manner. This has been difficult because the large-scale structures, which contain most of the turbulent energy, vary considerably from one flow to another, thereby precluding a general description. In large-eddy simulation, only the finest structures are left under-resolved, and their dominant effect must be accounted for through some other means. Since fine-scale structures are believed to be homogeneous and possess a universal character, their effect may be more easily and reliably modeled. Additionally, the fine structures contain only a fraction of the total turbulent kinetic energy, and it is therefore generally assumed that they may be accounted for without unduly affecting larger turbulent eddies. This may be done through use of an SGS stress model to provide the dissipation supplied by the fine-scale structures, or by the dissipation inherent in the numerical solving procedure. In the latter case, care must be taken that implicit dissipation of the computational scheme does not dominate that intrinsic to an explicitly added SGS model approach.

Applications of LES to increasingly practical configurations of engineering interest, is motivated by the need to provide more realistic characterizations of the complex unsteady and separated flows that are encountered in areas of aeroacoustics, aero-optics, fluid/structure interactions, and active flow control. In these situations, accurate prediction of the flowfields requires that the large-scale dynamics must be properly captured, which is a requirement beyond the capabilities of traditional Reynolds-averaged Navier-Stokes (RANS) methodology. Particularly for control applications, the baseline case that is sought to be modified, may contain large regions of highly unsteady separated flow that are not in turbulent equilibrium. Small-scale fluid structures may be present, and portions of the flowfield may also be transitional. For these reasons, descriptions by RANS models are highly inadequate. In addition, control techniques are often predicated upon unsteady forcing which can generate additional small-scale structures, enhance mixing, and create supplemental turbulent kinetic energy. Unsteady forcing may also be used to perturb unstable shear layers, or as a “tripping” mechanism to promote bypass transition. Because more recently developed hybrid procedures[1, 2, 3] that combine RANS modeling with large-eddy simulation have not been shown to be generally satisfactory for active flow control applications, numerical techniques at least as sophisticated as LES are more commonly required for this class of problems.

The purpose of this paper is to describe a computational method for performing large-eddy simulation, that has been developed over an approximately ten year period. As the method has matured during that time, a number of active flow control applications have been considered, some of which are summarized here. There are several features of the general approach which make it attractive for performing active flow control simulations. It is based upon an implicit time-marching algorithm[4], so that it is suitable for wall-bounded flows. High-order spatial accuracy is achieved by use of an implicit compact finite-difference scheme[5], making LES resolution attainable, with a minimal expenditure of computational resources. Robustness is enhanced by employing a low-pass Pade-type non-dispersive spatial filter[6] that regularizes the solution in flow regions where the computational mesh is not sufficient to fully resolve the smallest captured structures. Due to the spectral-like dissipation properties of the filter, it also serves the same function as that of an SGS model without additional computational expense. In order to accommodate geometrically complex configurations, an overset grid technique is adopted, with high-order interpolation[7, 8] to maintain spatial accuracy at overlapping mesh interfaces. Details of these features are described in sections that follow. To illustrate application for active flow control simulations, several separate computations are considered. These consist of acoustic resonance suppression in supersonic cavity flow, leading-edge vortex control of a delta wing, efficiency enhancement of a transitional highly-loaded low-pressure turbine blade, and separation control of a wall-mounted hump model. Control techniques represented in these examples are comprised of both steady and pulsed mass injection or removal, as well as plasma-based actuation. Features of the flowfield are elucidated for each case, and comparisons are made with baseline situations where no control was enforced, and with experimental data where available.

2 The Governing Equations

The governing fluid equations are taken as the unsteady three-dimensional compressible unfiltered Navier-Stokes equations. Although these computations are considered to be large-eddy simulations, it will be subsequently explained why the unfiltered equations are solved. After introducing a transformation from Cartesian coordinates to a general time-dependent body-fitted curvilinear system, the equations are cast in the following nondimensional conservative form

$$\frac{\partial}{\partial t} \left(\frac{1}{\mathcal{J}} \mathbf{Q} \right) + \frac{\partial}{\partial \xi} \left(\mathbf{F} - \frac{1}{Re} \mathbf{F}_v \right) + \frac{\partial}{\partial \eta} \left(\mathbf{G} - \frac{1}{Re} \mathbf{G}_v \right) + \frac{\partial}{\partial \zeta} \left(\mathbf{H} - \frac{1}{Re} \mathbf{H}_v \right) = D_c q_c \mathbf{S}. \quad (1)$$

Here t is the time, ξ, η, ζ the computational coordinates, \mathbf{Q} the vector of dependent variables, $\mathbf{F}, \mathbf{G}, \mathbf{H}$ the inviscid flux vectors, and $\mathbf{F}_v, \mathbf{G}_v, \mathbf{H}_v$ the viscous flux vectors. A source vector \mathbf{S} has been included in the formulation, and is used to represent the body force induced by an electric field for examples which utilized plasma-based control. The vector of dependent variables is given as

$$\mathbf{Q} = \left[\rho \quad \rho u \quad \rho v \quad \rho w \quad \rho E \right]^T \quad (2)$$

the vector fluxes by

$$\mathbf{F} = \frac{1}{\mathcal{J}} \begin{bmatrix} \rho U \\ \rho u U + \xi_x p \\ \rho v U + \xi_y p \\ \rho w U + \xi_z p \\ \rho E U + \xi_{x_i} u_i p \end{bmatrix}, \quad \mathbf{G} = \frac{1}{\mathcal{J}} \begin{bmatrix} \rho V \\ \rho u V + \eta_x p \\ \rho v V + \eta_y p \\ \rho w V + \eta_z p \\ \rho E V + \eta_{x_i} u_i p \end{bmatrix}, \quad \mathbf{H} = \frac{1}{\mathcal{J}} \begin{bmatrix} \rho W \\ \rho u W + \zeta_x p \\ \rho v W + \zeta_y p \\ \rho w W + \zeta_z p \\ \rho E W + \zeta_{x_i} u_i p \end{bmatrix} \quad (3)$$

$$\mathbf{F}_v = \frac{1}{\mathcal{J}} \begin{bmatrix} 0 \\ \xi_{x_i} \tau_{i1} \\ \xi_{x_i} \tau_{i2} \\ \xi_{x_i} \tau_{i3} \\ \xi_{x_i} (u_j \tau_{ij} - Q_i) \end{bmatrix}, \quad \mathbf{G}_v = \frac{1}{\mathcal{J}} \begin{bmatrix} 0 \\ \eta_{x_i} \tau_{i1} \\ \eta_{x_i} \tau_{i2} \\ \eta_{x_i} \tau_{i3} \\ \eta_{x_i} (u_j \tau_{ij} - Q_i) \end{bmatrix}, \quad \mathbf{H}_v = \frac{1}{\mathcal{J}} \begin{bmatrix} 0 \\ \zeta_{x_i} \tau_{i1} \\ \zeta_{x_i} \tau_{i2} \\ \zeta_{x_i} \tau_{i3} \\ \zeta_{x_i} (u_j \tau_{ij} - Q_i) \end{bmatrix} \quad (4)$$

with the source term

$$\mathbf{S} = \frac{1}{\mathcal{J}} \begin{bmatrix} 0 \\ E_x \\ E_y \\ E_z \\ u E_x + v E_y + w E_z \end{bmatrix} \quad (5)$$

and

$$D_c = \frac{\rho_c e_c E_r l}{\rho_\infty u_\infty^2} \quad (6)$$

where

$$U = \xi_t + \xi_{x_i} u_i, \quad V = \eta_t + \eta_{x_i} u_i, \quad W = \zeta_t + \zeta_{x_i} u_i \quad (7)$$

$$E = \frac{T}{\gamma(\gamma-1)M_\infty^2} + \frac{1}{2} (u^2 + v^2 + w^2). \quad (8)$$

In the preceding expressions, u, v, w are the Cartesian velocity components, ρ the density, p the pressure, and T the temperature. All length scales have been nondimensionalized by the characteristic length l , and dependent variables have been normalized by their reference values except for p which has been nondimensionalized by $\rho_\infty u_\infty^2$. Components of the stress tensor and heat flux vector are expressed as

$$Q_i = - \left[\frac{1}{(\gamma-1)M_\infty^2} \right] \left(\frac{\mu}{Pr} \right) \frac{\partial \xi_j}{\partial x_i} \frac{\partial T}{\partial \xi_j} \quad (9)$$

$$\tau_{ij} = \mu \left(\frac{\partial \xi_k}{\partial x_j} \frac{\partial u_i}{\partial \xi_k} + \frac{\partial \xi_k}{\partial x_i} \frac{\partial u_j}{\partial \xi_k} - \frac{2}{3} \delta_{ij} \frac{\partial \xi_l}{\partial x_k} \frac{\partial u_k}{\partial \xi_l} \right). \quad (10)$$

The Sutherland law for the molecular viscosity coefficient μ and the perfect gas relationship

$$p = \frac{\rho T}{\gamma M_\infty^2} \quad (11)$$

were also employed, and Stokes' hypothesis for the bulk viscosity coefficient has been invoked.

During development of the computational procedure, the use of traditional SGS stress models was explored, and had been employed for one of the example problems presented below (supersonic cavity). In that circumstance, the filtered version of the governing equations was considered. The filtered form is similar to the one presented above, but includes additional SGS stress and heat flux terms which necessarily must be modeled. Principal effects of these terms are embodied in modified values of the molecular viscosity coefficient μ and the Prandtl number Pr , which are augmented to include contributions due to the SGS model.

3 The Numerical Method

3.1 The Time Marching Scheme

Time-accurate solutions to Eq. (1) were obtained numerically by the implicit approximately-factored finite-difference algorithm of Beam and Warming[4] employing Newton-like subiterations,[9] which has evolved as an efficient tool for generating solutions to a wide variety of complex fluid flow problems. The algorithm is used to advance the solution in time, and may be written in “delta” form as

$$\begin{aligned} & \left[\frac{1}{\mathcal{J}} + \left(\frac{2\Delta t}{3} \right) \delta_{\xi^2} \left(\frac{\partial \mathbf{F}^p}{\partial \mathbf{Q}} - \frac{1}{Re} \frac{\partial \mathbf{F}_v^p}{\partial \mathbf{Q}} \right) \right] \mathcal{J} \times \left[\frac{1}{\mathcal{J}} + \left(\frac{2\Delta t}{3} \right) \delta_{\eta^2} \left(\frac{\partial \mathbf{G}^p}{\partial \mathbf{Q}} - \frac{1}{Re} \frac{\partial \mathbf{G}_v^p}{\partial \mathbf{Q}} \right) \right] \mathcal{J} \times \\ & \left[\frac{1}{\mathcal{J}} + \left(\frac{2\Delta t}{3} \right) \delta_{\zeta^2} \left(\frac{\partial \mathbf{H}^p}{\partial \mathbf{Q}} - \frac{1}{Re} \frac{\partial \mathbf{H}_v^p}{\partial \mathbf{Q}} \right) \right] \Delta \mathbf{Q} = - \left(\frac{2\Delta t}{3} \right) \left[\left(\frac{1}{2\Delta t} \right) \left(\frac{3\mathbf{Q}^p - 4\mathbf{Q}^n + \mathbf{Q}^{n-1}}{\mathcal{J}} \right) \right. \\ & \left. + \delta_{\xi n} \left(\mathbf{F}^p - \frac{1}{Re} \mathbf{F}_v^p \right) + \delta_{\eta n} \left(\mathbf{G}^p - \frac{1}{Re} \mathbf{G}_v^p \right) + \delta_{\zeta n} \left(\mathbf{H}^p - \frac{1}{Re} \mathbf{H}_v^p \right) - D_{cqc} \mathbf{S}^p \right]. \end{aligned} \quad (12)$$

In this expression, \mathbf{Q}^{p+1} is the $p+1$ approximation to \mathbf{Q} at the $n+1$ time level \mathbf{Q}^{n+1} , and $\Delta \mathbf{Q} = \mathbf{Q}^{p+1} - \mathbf{Q}^p$. For $p = 1$, $\mathbf{Q}^p = \mathbf{Q}^n$. Second-order-accurate backward-implicit time differencing was used to obtain temporal derivatives.

The implicit segment of the algorithm incorporates second-order-accurate centered differencing for all spatial derivatives. Nonlinear artificial dissipation terms[10, 11] are also appended to the implicit operators to augment stability, but for simplicity have not been shown explicitly in Eq. (12). Efficiency is enhanced by solving this implicit portion of the factorized equations in diagonalized form.[12] Temporal accuracy, which can be degraded by use of the diagonal form, is maintained by utilizing subiterations within a time step. This technique has been commonly invoked in order to reduce errors due to factorization, linearization, diagonalization, and explicit application of boundary conditions. It is useful for achieving temporal accuracy on overset zonal mesh systems, and for a domain decomposition implementation on parallel computing platforms. Any deterioration of the solution caused by use of artificial dissipation and by lower-order spatial resolution of implicit operators is also reduced by the procedure. From a large number of previous computations, it was found that three subiterations per time step were sufficient to preserve second-order temporal accuracy. Because temporal accuracy is limited by the backward approximation in Eq. (12), further subiterations do not improve the solution. For all of the examples considered here, three subiterations per time step have been applied.

3.2 The Compact Finite-Difference Scheme

The compact difference scheme employed to obtain spatial derivatives on the right-hand side of Eq. (12) is based upon the pentadiagonal system of Lele,[5] and is capable of attaining spectral-like resolution. This is achieved through the use of a centered implicit difference operator with a compact stencil, thereby reducing the associated discretization error. The scheme is illustrated here in one spatial dimension on a uniformly spaced mesh for the general function $\phi(x)$ as

$$\begin{aligned} & \beta \left(\frac{\partial \phi}{\partial x} \right)_{i-2} + \alpha \left(\frac{\partial \phi}{\partial x} \right)_{i-1} + \left(\frac{\partial \phi}{\partial x} \right)_i + \alpha \left(\frac{\partial \phi}{\partial x} \right)_{i+1} + \beta \left(\frac{\partial \phi}{\partial x} \right)_{i+2} = \\ & a \left(\frac{\phi_{i+1} - \phi_{i-1}}{2\Delta x} \right) + b \left(\frac{\phi_{i+2} - \phi_{i-2}}{4\Delta x} \right) + c \left(\frac{\phi_{i+3} - \phi_{i-3}}{6\Delta x} \right). \end{aligned} \quad (13)$$

Equation (13) can be used to define families of both explicit ($\alpha = \beta = 0$) and implicit difference approximations by proper choice of the coefficients α, β, a, b, c . Because all of these schemes retain the central-difference formulation, there is no dissipation error associated with any of them. Following Lele[5] however, it is useful to examine their dispersion characteristics. This is done by performing a spatial wave number analysis on

the Fourier components of the function $\phi(x)$. For the analysis, we assume $\phi(x)$ is periodic on the interval $0 \leq x \leq L$ and let

$$\phi(x) = \sum_{m=-M/2}^{m=+M/2} \tilde{\phi}_m \exp\left(\frac{2\pi i m x}{L}\right) \quad \text{where } i = \sqrt{-1}, \quad \Delta x = L/M, \quad (14)$$

and $\tilde{\phi}_m$ are the Fourier coefficients. It is then convenient to define the scaled wave number Ω and the scaled coordinate S by

$$\Omega = \frac{2\pi m \Delta x}{L} \quad \text{and} \quad S = \frac{x}{\Delta x} \quad \text{respectively,} \quad (15)$$

$$\text{so that } \phi(S) = \sum_{m=-M/2}^{m=+M/2} \tilde{\phi}_m \exp(i\Omega S), \quad (16)$$

and to denote $d\phi/dS = \dot{\phi}$. From Eq. (16), it follows that

$$\dot{\phi} = \sum_{m=-M/2}^{m=+M/2} i\Omega \tilde{\phi}_m \exp(i\Omega S), \quad (17)$$

and upon comparing Eq. (16) with Eq. (17) it is seen that the exact derivative of ϕ generates Fourier coefficients that are simply related to those of the original function by the expression

$$\dot{\tilde{\phi}}_m = i\Omega \tilde{\phi}_m. \quad (18)$$

By direct substitution of Eq. (16) into the difference formula Eq. (13), the numerical approximation to the derivative $(\dot{\phi})_n$ results in Fourier coefficients with the relationship

$$(\dot{\tilde{\phi}}_m)_n = i\Omega' \tilde{\phi}_m \quad (19)$$

where Ω' is a modified wave number satisfying the expression

$$\Omega' = \frac{a \sin(\Omega) + (b/2) \sin(2\Omega) + (c/3) \sin(3\Omega)}{1 + 2\alpha \cos(\Omega) + 2\beta \cos(2\Omega)}. \quad (20)$$

Shown in Fig. 1 is a plot of the modified wave number Ω' as a function of the wave number Ω for a number of explicit and implicit schemes. For the function ϕ , $2\pi/\Omega$ indicates the number of points per period that are represented locally. The exact solution is given by $\Omega' = \Omega$. It is seen that the compact implicit schemes are able to better approximate the exact solution at much higher wave numbers. This is equivalent to requiring fewer points per period in order to achieve the same resolution. Lele[5] defined a resolving efficiency for comparing the various methods. From this criterion, it was shown that the sixth-order tridiagonal ($\beta = c = 0$) subset of Eq. (13) has 5-10 times better resolution than the traditional 2nd-order explicit approach ($\alpha = \beta = b = c = 0, a = 1.0$). It was further shown, as can be inferred from Fig. 1, that the resolving power of the 10th-order pentadiagonal formulation was not appreciably better than that of the sixth-order tridiagonal subset. We therefore restrict our spatial differencing scheme to a 4th-order or 6th-order tridiagonal implicit approximation, where

$$\alpha = 1/4, \quad \beta = 0, \quad a = 3/2, \quad b = c = 0 \quad \text{for the 4th-order scheme} \quad (21)$$

$$\text{and } \alpha = 1/3, \quad \beta = 0, \quad a = 14/9, \quad b = 1/9, \quad c = 0 \quad \text{for the 6th-order scheme.} \quad (22)$$

Based upon our experience, the tridiagonal subset of Eq. (13) increases the computational time by about a factor of two over that of a standard 2nd-order explicit scheme for solution of Eq. (1). But because of superior resolving capability, fewer computational resources need be expended with the high-order method, than are required with the standard approach, in order to attain the same level of resolution. Solution of the tridiagonal system of Eq. (13) is about 50% computationally less expensive than the pentadiagonal

counterpart. Thus the 4th-order and 6th-order compact difference schemes provide a somewhat optimal balance between efficiency and accuracy.

The compact difference schemes described above are used to obtain spatial derivatives of any scalar variable, such as a flux component, flow quantity, or metric coefficient appearing on the right-hand side of Eq. (12). Derivatives of inviscid fluxes are computed by forming flux quantities at grid points, and then applying the above formulas to each component. Viscous derivatives are obtained by first computing high-order derivatives of primitive variables. Components of the viscous fluxes are then constructed, and the compact difference scheme is applied a second time. Although this technique is not formally as accurate as a high-order scheme employed directly for evaluation of second derivatives, it requires less computational effort. It has also been demonstrated to produce accurate and stable results for for LES computations.[13] A description of high-order one-sided difference formulas for use near boundaries may be found in Ref. [14].

The compact difference scheme is also used to evaluate metric coefficients and the Jacobian of the coordinate transformation indicated in Eq. (12). This is done for example, in the relationship

$$\xi_x = y_\eta z_\zeta - y_\zeta z_\eta \quad (23)$$

by applying difference formulas to the analytic equivalent conservative form

$$\xi_x = (y_\eta z)_\zeta - (y_\zeta z)_\eta. \quad (24)$$

Use of Eq. (24) follows the development from Refs. [15] and [16] which are based upon the treatment by Thomas and Lombard[17] for low-order methods. The technique is used to preserve the metric identities

$$(\xi_x)_\xi + (\eta_x)_\eta + (\zeta_x)_\zeta = 0, \quad (\xi_y)_\xi + (\eta_y)_\eta + (\zeta_y)_\zeta = 0, \quad (\xi_z)_\xi + (\eta_z)_\eta + (\zeta_z)_\zeta = 0 \quad (25)$$

which were implicitly invoked for the derivation of Eq. (12). Reference [18] gives additional details about the treatment of time-dependent metric coefficients and the Jacobian for deforming mesh applications.

3.3 The Compact Filtering Scheme

As noted previously, the compact central difference approximation is nondissipative, and therefore can be susceptible to numerical instabilities which arise due to unrestricted growth of high-frequency spatial modes. Such instabilities originate from several sources, that include mesh nonuniformities, approximate boundary conditions, and nonlinear flow behavior. In order to extend the compact discretization to practical applications, a high-order low-pass Pade-type non-dispersive spatial filtering technique[13, 6] is incorporated as part of the numerical methodology. This low-pass filter provides dissipation at high spatial wave numbers, only where the resolution already exhibits significant dispersion error.

A general expression for a family of implicit filters applied to the function ϕ may be written as

$$\beta_f \hat{\phi}_{i-2} + \alpha_f \hat{\phi}_{i-1} + \hat{\phi}_i + \alpha_f \hat{\phi}_{i+1} + \beta_f \hat{\phi}_{i+2} = \sum_{n=0}^N \frac{a_n}{2} (\phi_{i-n} + \phi_{i+n}) \quad (26)$$

where $\hat{\phi}$ is the filtered value of ϕ . Equation (26) can be used to define unique filter representations with accuracy of order $2N+6$. These filters provide no dispersion, and once more following Lele[5], their dissipation properties may be characterized from a wave number analysis. Assuming again that ϕ is periodic and may be expressed in terms of the Fourier series given by Eq. (16), it follows from Eq. (26) that

$$\hat{\phi} = \sum_{m=-M/2}^{m=+M/2} \mathcal{T}(\Omega) \tilde{\phi}_m \exp(i\Omega S) \quad (27)$$

$$\text{where } \mathcal{T}(\Omega) = \frac{\sum_{n=0}^N a_n \cos(n\Omega)}{1 + 2\alpha_f \cos(\Omega) + 2\beta_f \cos(2\Omega)}. \quad (28)$$

Equation (27) illustrates that Fourier components of the filtered function $\widetilde{\phi}_m$ are related to those of the original function by

$$\widetilde{\phi}_m = \mathcal{T}(\Omega)\widetilde{\phi}_m \quad (29)$$

where $\mathcal{T}(\Omega)$ is the spectral transfer function. We find it practical to restrict consideration to tridiagonal subsets of Eq.(26) ($\beta_f = 0$). Although it is then possible to achieve a unique description of order $2N + 4$ using a $2N + 1$ stencil, we choose to limit the order to $2N$. This allows freedom to enforce two additional constraints upon the filter operator through the choice of the coefficients α_f, a_n 's. One of these is supplied by requiring

$$\mathcal{T}(\pi) = 0 \quad (30)$$

which fully damps all contributions with resolution less than two points per period. The other condition allows the implicit coefficient α_f to remain a free parameter, which may be adjusted for specific applications. For proper behavior of the transfer function $\mathcal{T}(\Omega)$, the adjustable coefficient α_f must lie in the range $-0.5 < \alpha_f < 0.5$, where higher values correspond to less dissipative filters. Explicit filter formulas are obtained with $\alpha_f = 0$. On uniform meshes, these symmetric filters are non-dispersive ($\mathcal{T}(\Omega)$ is real), do not amplify waves ($\mathcal{T}(\Omega) \leq 1$), preserve constant functions ($\mathcal{T}(\Omega) = 1$), and preclude odd-even mode decoupling ($\mathcal{T}(\pi) = 0$).

Because the finite-difference approximation is limited to at most sixth-order accuracy, we consider filters no higher than 10th-order, having an 11 point stencil, so that our filtering formula is given by

$$\alpha_f \widehat{\phi}_{i-1} + \widehat{\phi}_i + \alpha_f \widehat{\phi}_{i+1} = \sum_{n=0}^N \frac{a_n}{2} (\phi_{i-n} + \phi_{i+n}) \quad N \leq 5. \quad (31)$$

It is required that accuracy of the filter should be at least two orders higher than that of the differencing scheme employed for any large-eddy simulation. Presented in Fig. 2 is a plot of the transfer function $\mathcal{T}(\Omega)$ for several different filters. The exact result corresponds to the unfiltered form with $\mathcal{T}(\Omega) = 1$. As expected, lower-order filters provide more dissipation at lower wave numbers. Also, for filters of the same order, explicit formulations are more dissipative than implicit ones (see 6th-order results in Fig. 2). The effect of varying the implicit coefficient α_f for the 10th-order tridiagonal subset is illustrated in Fig. 3. With $\alpha_f = 0.49$, the spectral-like behavior is demonstrated.

Unlike numerical methods which employ the use of explicitly added artificial dissipation, thereby modifying the original governing equations, the filtering operation is a post processing technique. It is applied to the evolving solution in order to regularize features that are captured but poorly resolved. Filtering is carried out on the conserved variables successively along each of the transformed coordinate directions. For the example applications subsequently to be described, filtering was imposed once following every subiteration. In general however, it may be invoked repeatedly or less frequently depending on the nature of specific problems. Numerical values for the explicit coefficients a_n 's as a function of the implicit coefficient α_f may be found in Ref. [14].

A tenth-order central filter having an 11-point stencil cannot be applied within a distance of five grid points from a computational boundary. In this region, a centered stencil may be retained only if the order-of-accuracy of the filter is reduced, and/or one-sided filter formulations are employed. As opposed to the central formulation, one-sided filters may generate amplification in certain ranges of wave number. Amplification levels become larger as the order of the filter is increased, corresponding to a more one-sided filter. The region over which this amplification occurs however, shifts to higher wave numbers with increasing order, thus improving spectral behavior in the resolved wave space region. Spurious waves that may be amplified by high-order one-sided boundary filters tend to be removed by interior filters as they propagate away from boundaries. Increasing the value of the filter coefficient α_f for near-boundary points can also reduce amplification associated with one-sided filters. Filtering strategies for the treatment of near-boundary points appear in Refs. [13] and [15]. The impact of filtering on the accuracy and stability of the high-order approach has been investigated by Visbal and Gaitonde[13, 15, 16] for a number of flow situations, which address nonuniform grids, approximate boundary treatments, and nonlinear governing equations.

3.4 The Overset Grid Approach

An overset grid approach[19] is employed in order to provide flexibility for treating complex geometric configurations. This allows structured grid formulations of the compact differencing and filtering schemes

to be adapted for practical simulations. In addition, the technique also allows local grid refinement which may be necessary to capture physical details arising from a large-eddy simulation. It is particularly useful for consideration of active flow control, that may require modeling of actuation devices, or may locally generate small-scale fluid structures. Furthermore, local refinement can be used to reduce overall resource requirements for computationally demanding simulations.

Although the overset grid approach is fundamentally motivated by its ability to describe geometric complexity, it is also employed to enable domain decomposition for processing on parallel computing platforms. Individual unique mesh entities may be sub-divided into any number of smaller grid systems, each of which are then operated on by a single processor. To maintain high-order accuracy, all grid systems are required to overlap with their adjoining neighbors. This is true for both sub-divided meshes and geometrically distinct grids. It has been shown in previous studies[20], that an overlap of five-planes in the region between respective meshes, is sufficient to maintain the interior high-order differencing and filtering schemes. The overlap region consists of two levels (contiguous planes) of donor/receiver planes of grid points which are overset into adjacent domains on each side of the overlap. This arrangement is typically employed for decomposed grids with coincident mesh points, but a somewhat larger overlap may necessarily be utilized for general overset domains due to variations in grid topology.

An example of the five-point overlap for domain decomposition is shown in Fig. 4. The figure illustrates details of the overlap for the simple schematic representation of a vortex convecting between two sub-domains separated by a vertical interface. The vortex located in mesh 1, is traveling from left to right. It passes through the five point overlap and into mesh 2. Information is transferred between the two sub-domains, which are distributed on different processors, via the five-point overlap using message-passing interface (MPI) communications.[21] The expanded view of the overlap region in the figure shows the two sets of five vertical lines, each denoted by its I index, which are used for communication between the grids. Although the overlap points are coincident, they have been shown slightly staggered for clarity. Data is exchanged between adjacent subdomains at the end of each sub-iteration of the time-marching scheme. The values of flow variables at points 1 and 2 of mesh 2 are set to be equal to those of the corresponding updated values at points $IL - 4$ and $IL - 3$ of mesh 1. Similarly, reciprocal information is transferred through points 4 and 5 of mesh 2 which “inject” the solution into points $IL - 1$ and IL of mesh 1. Point 3 in mesh 1 and $IL - 2$ in mesh 2 are solved independently, and not updated with the solution from the adjacent domain. Use of these dual solutions, facilitates detecting any disparity between results in the respective domains.

Connectivity between donor/receiver pairs is establish as a pre-processing step prior to computation, using automated software. For each receiver grid point, the PEGASUS[22] utility is used to identify a donating stencil. PEGASUS also defines second-order accurate interpolation coefficients. In the case of sub-divided grids with coincident points in the overlap region, these coefficients degenerate to “direct injection” so that there is no interpolation error. When the overlap region consists of non-coincident grid points, high-order interpolation must be implemented in order to maintain the overall accuracy of the numerical methodology. This is achieved with a second pre-processing utility BELLERO[23], that is employed to modify second-order interpolation stencils in order to accommodate a more accurate approximation. If $\check{\phi}_p$ denotes the interpolated value of the flowfield variable ϕ at grid point p using known information of ϕ on another grid at the donor stencil defined by point (I_p, J_p, K_p) , then the high-order explicit Lagrangian formula

$$\check{\phi}_p = \sum_{i=0}^{\sigma-1} \sum_{j=0}^{\sigma-1} \sum_{k=0}^{\sigma-1} R_i^1 R_j^2 R_k^3 \phi_{I_p+i, J_p+j, K_p+k} \quad (32)$$

is applied. In Eq.(32), σ is the formal order-of-accuracy of the interpolated approximation and R_i^1, R_j^2, R_k^3 are coefficients given by the analytic expressions

$$R_i^1 = \frac{(-1)^{\sigma+i-1}}{[\sigma - (i-1)!] i!} \prod_{\substack{n=0 \\ n \neq i}}^{\sigma-1} (\Delta_1 - n) \quad (33)$$

$$R_j^2 = \frac{(-1)^{\sigma+j-1}}{[\sigma - (j-1)!] j!} \prod_{\substack{n=0 \\ n \neq j}}^{\sigma-1} (\Delta_2 - n) \quad (34)$$

$$R_k^3 = \frac{(-1)^{\sigma+k-1}}{[\sigma - (k-1)!] k!} \prod_{\substack{n=0 \\ n \neq k}}^{\sigma-1} (\Delta_3 - n) \quad (35)$$

where $0 \leq i, j, k \leq \sigma - 1$ and $\Delta_1, \Delta_2, \Delta_3$ are interpolation offsets in the ξ, η, ζ directions, representing distances from the base donor point (I_p, J_p, K_p) to the interpolation point in the computational space of the donor grid ($0 \leq \Delta_1, \Delta_2, \Delta_3 \leq \sigma - 1$). The base donor point location (I_p, J_p, K_p) and interpolation offsets $(\Delta_1, \Delta_2, \Delta_3)$ are obtained from PEGASUS/BELLERO.

Once donating stencils and interpolation coefficients are defined, inter-node communication among various processors is established through MPI library routines,[21] which are used to transfer information between the various grids at domain boundaries, as previously mentioned. We note that the BELLERO utility has a number of additional useful capabilities. It can be employed as “stand alone” software (without PEGASUS) for the partitioning of single grid systems, where domain decomposition is enforced only for parallel processing and no true interpolation is required. BELLERO can also generate connectivity for application of periodic boundary conditions, and may be employed for the treatment of “holes” or “blanked out” regions. The flowfield in these “holes” or “blanked out” regions are then described by overset background grids, which is a commonly employed technique in overset methods.

3.5 The LES Approach

With a traditional LES approach, physical dissipation at the Kolmogorov scale is not represented. For spatially nondissipative numerical schemes, without use of SGS models, this leads to an accumulation of energy at high mesh wave numbers, and ultimately to numerical instability. Explicitly added SGS models are then employed as a means to dissipate this energy. In the present methodology, the effect of the smallest fluid structures is accounted for by an implicit large-eddy simulation (ILES) technique, which has been successfully utilized for a number of turbulent and transitional computations, some of which will subsequently be described. The ILES approach was first introduced by Visbal et al. [18, 24] as a formal alternative to conventional methodologies, and is predicated upon the high-order compact differencing and low-pass spatial filtering schemes, without the inclusion of additional SGS modeling. This technique is similar to monotonically integrated large-eddy simulation (MILES)[25] in that it relies upon the numerical solving procedure to provide the dissipation that is typically supplied by traditional SGS models. Unlike MILES however, dissipation is contributed only at high spatial wavenumbers where the solution is poorly resolved, by the aforementioned high-order Pade-type low-pass filter. This allows a mechanism for the turbulence energy to be dissipated at scales that cannot be accurately resolved on a given mesh system, in a fashion similar to subgrid modeling. For purely laminar flows, filtering may be required to maintain numerical stability and preclude a transfer of energy to high-frequency spatial modes due to spurious numerical events. The ILES methodology thereby permits a seamless transition from large-eddy simulation to direct numerical simulation as the resolution is increased. In the ILES approach, the unfiltered governing equations may be employed, and the computational expense of evaluating subgrid models, which can be substantial, is avoided. This procedure also enables the unified simulation of flowfields where laminar, transitional, and turbulent regions simultaneously coexist.

It should also be noted that the ILES technique may be interpreted as an approximate deconvolution SGS model[26], which is based upon a truncated series expansion of the inverse filter operator for the unfiltered flowfield equations. Mathew et al.[27] have shown that filtering provides a mathematically consistent approximation of unresolved terms arising from any type of nonlinearity. Filtering regularizes the solution, and generates virtual subgrid model terms that are equivalent to those of approximate deconvolution.

3.6 Validation of the Numerical Method

The aforementioned features of the numerical algorithm are embodied in a parallel version of the time-accurate three-dimensional computer code FDL3DI,[14] which has proven to be reliable for steady and unsteady fluid flow problems, including vortex breakdown,[28, 29] transitional wall jets,[30] synthetic jet actuators,[31] roughness elements,[32] plasma flows,[33, 34, 35, 36] and direct numerical and large-eddy simulations of subsonic[37, 38] and supersonic flowfields.[39, 40] The procedure employed for parallelization has been demonstrated to be portable, due to the use of the standardized MPI library. FDL3DI has been

utilized successfully on a number of different computing platforms, and has maintained a parallel efficiency of 90% for up to 320 processors.

During development of this code, many aspects of the above cited numerical procedure were largely validated for a number of canonical and fundamental fluid flow problems. Among these are the simulation of decaying compressible isotropic turbulence[18, 38, 41], for which it was shown that better results were realized with use of the compact differencing/filtering scheme than could be obtained with either a constant coefficient[42] or dynamic Smagorinsky[43] SGS model[18]. For turbulent channel flows[18, 38, 8, 41], the use of local grid refinement indicated that high accuracy was achieved with a minimal number of grid points, if the mesh system was distributed properly. It was also found[41] that the numerical approach attained DNS level resolution for high-Reynolds channels.

Simulations for subsonic transitional flow past a circular cylinder[38, 8, 41] again illustrated the benefit of local grid refinement, and properly captured the correct experimentally measured behavior, which was not possible when SGS models were employed. Computations for a spatially evolving supersonic flat-plate boundary layer[44] also compared well with experimental data, and performed better than simulations that utilized SGS models.

4 Empirical Plasma Model

Two of the computational examples to be considered subsequently (delta wing, low-pressure turbine blade), utilized plasma-based actuation to administer active flow control. The following section describes the approach for simulating this situation. Many quantitative aspects of the fundamental processes governing plasma/fluid interactions remain unknown or computationally prohibitive, particularly for transitional and turbulent flows. These circumstances have given rise to the development of a wide spectrum of models with varying degrees of sophistication, that may be employed for more practical computations. Among the simplified methods focused specifically on discharge/fluid coupling is that of Roth et al., [45, 46] who associated transfer of momentum from ions to neutral particles based upon the gradient of electric pressure. A more refined approach, suitable for coupling with fluid response was an empirical model proposed by Shyy et al., [47] using separate estimates for the charge distribution and electric field. Known plasma physics parameters were linked to experimental data. This representation has been successfully employed for several previous simulations of plasma-controlled flows, [33, 34, 35, 36] and was also adopted in the present examples.

A schematic representation of a typical single asymmetric dielectric-barrier-discharge (DBD) plasma actuator is depicted in Fig. 5. The actuator consists of two electrodes that are separated by a thin dielectric insulator, and mounted on a body surface. An oscillating voltage, in the 10-15 kHz frequency range, is applied to the electrodes, developing an electric field about the actuator. When the imposed voltage is sufficiently high, the dielectric produces a barrier discharge, that weakly ionizes the surrounding gas. Momentum acquired by the resulting charged particles from the electric field, is transferred to the primary neutral molecules by a combination of electrodynamic body forces and poorly understood complex collisional interactions. Because the bulk fluid cannot respond rapidly to the high frequency alternating voltage, the dominant effect of actuation is to impose a time-mean electric field on the external flow. In the numerical simulation of plasma-based control, the entire process was modeled as a body force vector acting on the net fluid adjacent to the actuator, which produces a flow velocity.

The model for the geometric extent of the plasma field generated by such an actuator is indicated in Fig. 6. The triangular region defined by the line segments AB , BC , and AC constitutes the plasma boundary. Outside of this region the electric field is not considered strong enough to ionize the air. [47] The electric field has its maximum value on segment AC , and varies linear within ABC . The peak value of the electric field is obtained from the applied voltage and the spacing between the electrodes. Along the segment AB , the electric field diminishes to its threshold value, which was taken as 30 kV/cm. [47] The electric body force is equal to $q_e \mathbf{E}$ and provides coupling from the plasma to the fluid, resulting in the source vector \mathbf{S} appearing in Eq. (1). The direction of the force vector depends upon the ratio AC/BC , but for the simulations presented here, the vector was assumed to be tangential to the actuator surface. Within the region ABC , the charge density q_e is taken to be constant. The plasma scale parameter D_e arises from nondimensionalization of the governing equations, and represents the ratio of the electrical force of the plasma to the inertial force of the fluid.

Some specific details of the plasma model incorporated in the example simulations, were specified similar to those of the original experiment of Shyy et al.[47] Referring to Fig. 6, the distances BC and AC nondimensionalized by the characteristic length l (delta wing root chord, turbine blade chord) were taken as $BC = 0.018$ and $AC = 0.024$ for the delta wing and $BC = 0.0125$ and $AC = 0.0250$ for the turbine blade respectively. For the purposes of these computations, it was assumed that actuators were mounted flush with the configuration surface and did not protrude above it. Due to empiricism of the formulation, there is some ambiguity regarding the value of the scale parameter D_e .

Operationally, DBD actuators are inherently unsteady devices. Within the context of the empirical model however, the body force imposed on the fluid is assumed to be steady, owing to the high frequency of the applied voltage (typically 10-15 kHz). These devices may also be operated in a pulsed manner as described by Corke and Post, [48] thereby reducing total power consumption. The pulsed mode of operation also introduces low-frequency forcing to the flow, which may be more receptive to control, and offers the potential of improved effectiveness. These actuators have no moving parts, can be surface conforming, and provide on demand control with low power utilization.

Table 1: Cavity flow conditions

	Re	$Re_{\delta 0}$	$Re_{\theta 0}$
present LES	2.00×10^5	6,774	667
experiment[49, 50, 51, 52]	3.01×10^6	51,700	5,030

5 Acoustic Suppression of Supersonic Cavity Flow

High speed flows over open cavities produce complex unsteady interactions, which are characterized by a severe acoustic environment. At high Reynolds numbers, such flowfields are comprised of both broad-band small-scale fluctuations typical of turbulent shear layers, and discrete resonance whose frequency and amplitude depend upon the cavity geometry and external flow conditions. While these phenomena are of fundamental physical interest, they also represent a number of significant concerns for aerospace applications. In the practical situation of an aircraft weapons bay, aerodynamic performance or stability may be adversely affected, structural loading may become excessive, and sensitive instrumentation may be damaged. Acoustic resonance can also pose a threat to the safe release and accurate delivery of weapons systems stored within the cavity.

Because of the intricate nature and practical significance of supersonic cavity flows, numerous experimental and numerical investigations have been conducted in order to understand their underlying physical behavior. A summary of these may be found in Ref. [40]. For the simulations presented here, we consider a deep cavity where the length to depth ratio is less than 9. In this situation, the boundary layer ahead of the upstream lip forms into a free shear layer, which then flows over the cavity and impinges upon the rear bulkhead. The undulating shear layer generates strong compression waves both external and internal to the cavity, and results in periodic addition or removal of mass from the cavity at the downstream bulkhead, thereby producing a self-sustained fluid oscillation.

The purpose of these simulations was to numerically reproduce the turbulent supersonic flow past an open rectangular cavity. In addition to the baseline flow without control, high-frequency forcing, via pulsed mass injection upstream of the forward cavity lip, was implemented numerically in order to investigate the ability of large-eddy simulation to predict acoustic resonance suppression. For both unsuppressed and suppressed cases, experimental data was available for comparative purposes in the form of instantaneous pressure measurements[49, 50, 51, 52] on interior cavity surfaces.

The cavity geometric configuration is represented schematically in Fig. 7, where the length to depth ratio $l/d = 5.0$ and the freestream Mach number is 1.19. The cavity length l was used as the reference distance for nondimensionalization. Conditions at which experimental measurements were taken[49, 50, 51, 52] correspond to a Reynolds number of 3.01×10^6 based upon the cavity length l . Because it would not be possible to numerically resolve fine-scale turbulent structures at the experimental Reynolds number, simulations were carried out for $Re = 2.0 \times 10^5$. Reference quantities in terms of the incoming boundary-layer parameters are provided in Table 1.

As previously noted, these large-eddy simulations were carried out using the dynamic Smagorinsky SGS model[43]. While an entire description of the equations governing this model is not crucial to this example, complete details are documented in Ref. [53]. The numerical scheme for the computations utilized a fourth-order compact finite-difference approximation and a sixth-order spatial filter. A mesh system consisting of two discrete domains was employed to represent the regions exterior and interior to the cavity flowfield. These consisted of $(725 \times 225 \times 101)$ and $(351 \times 121 \times 101)$ grid points respectively in the x, y, z directions, which were distributed over 254 processors for parallel computing. The mesh system is more completely described in Refs. [40] and [53]. Inflow profiles containing turbulent structures, were generated from an auxiliary flat-plate simulation (see Refs. [40] and [53] for details). The specification of all boundary condition can also be found in Refs. [40] and [53].

Active flow control, applied to produce suppression of resonant acoustic oscillatory modes within the cavity, was simulated by specifying a velocity profile exiting through the mass-ejection slot appearing Fig. 7. This profile had the following assumed functional form

$$v = A \sin(\omega_x x) \sin^2(0.5\omega_t t), \quad (36)$$

$$\omega_x = \pi \left(\frac{x - x_{j1}}{x_{j2} - x_{j1}} \right), \quad (37)$$

$$\omega_t = 2\pi l \times 5000 / u_\infty. \quad (38)$$

In the above, x_{j1} and x_{j2} are the upstream and downstream extents of the slot respectively, and A is an amplitude which could be adjusted to control the mass-flow rate. A dimensional forcing frequency of 5000 Hz corresponds to the value of ω_t , which matches that of the experiment. The assumed profile generates a fluctuating injection velocity which is always positive. At the plane of the jet exit, the pressure was obtained from the inviscid normal momentum equation, and the jet was assumed to be isothermal at the wall temperature.

Several differences exist between the computed flowfields, and the experimental configuration which they attempt to simulate, observed in Fig. 8. Evident in the figure, are sidewall surfaces which mimic weapons bay doors in the open position. The width to length ratio of the configuration is 0.2, which is about twice that of the computational domain. Mass injection was delivered by a series powered resonance tubes[49], located beneath the jet exit. These tubes were fed by a single plenum and discharged through the common slot. The expelled flow was probably neither two-dimensional nor isothermal, but the complex nature of the interior region below the slot was beyond the scope of the simulation.

5.1 Features of the Time-Mean Flowfields

Features of the time-mean cavity flowfields are described in Figs. 9-14. For all of these results, information was obtained by spatial averaging in the homogeneous direction (spanwise), as well as temporally. Displayed in Fig. 9 are contours of the mean pressure coefficient. Dark areas represent regions of low pressure, whereas high pressures are lighter. A weak oblique shock lies a distance of approximately one cavity depth upstream of the forward bulkhead in the unsuppressed case, and more than twice that distance when mass injection is active. Pressure levels within the cavity are noticeably lower (darker) in the suppressed case. Found in the unsuppressed case is a low pressure region at the mouth of the cavity upstream of the aft bulkhead. For the suppressed case, the pressure in this area is lower, and its vertical extent is much greater. A more quantitative comparison of the mean pressure levels is provided by the distributions along the cavity floor ($y = -0.2$) in Fig. 10. Reduction in the level of C_p due to suppression is apparent.

Time-mean streamwise velocity contours appear in Fig. 11. A thickening of the boundary layer upstream of mass injection can be observed in the suppressed case. Also noted in the suppressed case, is a reduction in size of the low speed region within the cavity near the rear bulkhead. Profiles of the mean streamwise velocity at three locations are shown in Fig. 12. A reduction in reversed flow for the suppressed case at $x = 0.5$ is evident.

Contours of mean turbulent kinetic energy are seen in Fig. 13. Although the level of the kinetic energy is elevated in the immediate vicinity of the injection slot due to high frequency forcing, its overall effect is to reduce the level downstream and within the cavity. Spatial statistical characteristics of the cavity acoustic resonance are illustrated by the turbulent kinetic energy spanwise wave-number spectra of Fig. 14. These spectra were generated at three streamwise locations for $y = 0.2\delta_0/l$. This position is located within the turbulent shear layer over the mouth of the cavity. The figure was produced by constructing spectra at each time step and temporally averaging the result. Here, the figure shows that the energy is higher in the suppressed case at all streamwise locations, most noticeably at $x = 0.2$. It should be noted that the locations represented in the figure lie within the shear layer where forced injection was initiated. And although the energy of the shear layer increased, peak amplitudes of the primary modes were diminished.

5.2 Features of the Unsteady Flowfields

Features of the unsteady cavity flowfields are elucidated by a series of instantaneous contours of flow variables in Figs. 15 and 17-21. In all of these figures, the contours were formed at the cavity midspan centerline. Contours of the fluctuating pressure $\overline{p'p'}$ are depicted in Fig. 15. A decrease in magnitude with suppression is most noticeable at the rear bulkhead. Fluctuating pressure profiles indicated in Fig. 16 quantify the mitigating effect of suppression. Instantaneous contours of Mach number in Fig. 17, reveal the shock wave structures that arise near the cavity rear bulkhead, and upstream of the pulsing jet. These contours

demonstrate the shear layer that spans the mouth of the cavity. Dark contours in the figure denote regions of slowly moving fluid.

Presented in Figs. 18-21 are instantaneous contours of the spanwise component of vorticity. These planar representations were generated at the midspan location, for four discrete instants in time t_1, t_2, t_3, t_4 . Dynamics of the cavity flowfield are dominated by large-scale vortical structures which form aft of the forward bulkhead, and convect downstream. These structures evolve through a “roll up” of the unstable shear layer, which is created as the boundary layer leaves the surface ahead of the cavity at the forward lip. The time sequence t_1, t_2, t_3, t_4 represents one cycle of the vortex shedding period, divided into equally spaced increments. Unsuppressed and suppressed results were synchronized, so that at each time instant, contours from both cases corresponded to the identical point within the vortex shedding cycle.

At $t = t_1$ (Fig. 18), one large vortical structure is forming in the upstream half of the cavity, while another has been destroyed as it impacted the rear cavity lip. Within the vortex, fine-scale turbulence is apparent in the vorticity contours. Fine-scale turbulence is also observed in the incoming boundary layer upstream of the forward lip. The figure shows that the vortex of the suppressed case is weaker than its unsuppressed counterpart. This is because energy has been added to the shear layer through forced mass injection, and it is better able to withstand its natural tendency to roll up. In addition, the injection has disrupted the coherence of the shear layer.

The state of the flowfield at $t = t_2$ is provided in Fig. 19. Here the vortex has moved further downstream, and now lies in the center of the cavity. This has produced a large deflection of the shear layer in the unsuppressed case. The vortex begins its impact upon the rear bulkhead at $t = t_3$ as is evident in Fig. 20. Now, the shear layer at the upstream cavity lip has returned to an almost undeflected condition. Finally, at $t = t_4$ in Fig. 21, the vortex fully impinges upon the rear bulkhead. The impingement is much less severe in the suppressed case, because the vortex is weaker and flatter. A new vortex can be seen forming downstream of the forward cavity lip, thus completing the shedding cycle. More complete discussions of the instantaneous external shock system and internal acoustic wave propagation are given in Refs. [40] and [53].

Turbulent kinetic energy frequency spectra at three streamwise locations for $y = 0.2\delta_0/l$ appear in Fig. 22. The figure displays two dominant modes, particularly in the unsuppressed case, where the frequency has been normalized by the first of these, ω_1 . A reduction in amplitude of the dominant modes is found for all streamwise stations in the suppressed case. Addition of energy due to mass injection appears for $x = 0.2, 0.5$ at $\omega/\omega_1 = 27.8$. Further downstream at $x = 0.8$, the effect of this addition has diminished. Similar to the spatial wavenumber spectra of Fig. 14, the frequency spectra were generated at each spanwise location, and then spatially averaged.

The three-dimensional cavity flowfield is depicted in Fig. 23, which provides instantaneous total pressure coefficient contours at several spanwise stations, as well as an iso-surface of total pressure that illustrates the primary vortical structure. In this representation, the spanwise (z) direction has been stretched in order to more easily view details of the flowfield. Although many aspects of the flow have a dominant two-dimensional appearance, the fine-scale features are clearly three-dimensional.

5.3 Comparison with Experimental Data

Comparison with the experimental data of Refs. [49, 50, 51, 52] is made in Figs. 24-27. This comparison consists of fluctuating pressure frequency spectra at discrete points located on the rear bulkhead and the cavity floor. As was done for the turbulent kinetic energy, frequency spectra were constructed at every z location and the results were then spanwise averaged. The amplitude of the fluctuating pressure is presented as sound pressure level (*SPL*) in dB, and the frequency ω is given in Hz, as is customary for acoustic investigations, and is compatible with the experimental data. In terms of the nondimensional fluctuating pressure, the *SPL* was obtained as

$$SPL = 20 \log_{10} \left[\frac{\rho_\infty u_\infty^2 \sqrt{p'p'}}{q} \right] \quad (39)$$

where $q = 2 \times 10^{-5}$ Pa.

The sound pressure level on the rear bulkhead ($x = 1.0$) at $y = -0.04$ is seen in Fig. 24. This location is just below the aft lip of the cavity, and experiences the highest pressures due to the oblique shock wave which

moves downstream preceding the vortex, and passes over the lip. For the unsuppressed case, amplitudes of the computed *SPL* of the two dominant modes compare well to the experiment. The corresponding frequencies of these modes from the LES are somewhat smaller than those of the measurements. This is probably because the Reynolds number of the computations is considerably lower. It should be noted that the experimental frequencies agree with the empirical relationship of Rossiter[54, 55], which is a high Reynolds number correlation. When acoustic suppression is active, both the experiment and computation indicate a 15 dB reduction in the amplitude of the dominant mode.

Figures 25-27 illustrate pressure levels at several streamwise locations along the floor of the cavity ($y = -0.2$). Amplitudes on the floor are not as high as those on the rear bulkhead. Reduction of the acoustic modes with suppression is apparent, and the large-eddy simulations compares favorably with the experiment.

The mass flux of forced injection for the suppressed case of the experimental configuration is approximately 145.6 kg/s-m². Smaller values of mass flux were also considered in the investigation, but were not effective in suppressing the acoustic resonant modes. In the large-eddy simulation, the time-mean mass flux was only 22% of the experimental value. When the full experimental value of mass flux was employed in the computation, massive separation occurred upstream of the injection slot. This resulted in a large displacement of the boundary layer, and the formation of a near normal shock wave ahead of the displaced region. The normal shock wave then caused further separation of the boundary layer, and it began to travel upstream. Eventually the shock reached the upstream boundary, and the computation was terminated. The reason for this physical behavior was because the Reynolds number ($Re_{\delta 0}$) of the computed flow was an order of magnitude lower than that of the experiment (see Table 1). Therefore, the boundary layer contained less energy and was not able to withstand the disruption of strong mass injection.

The second mode of the frequency spectra found in Figs. 25-27 which occurs at approximately 420 Hz for the LES, correlates with the shedding frequency of the vortical structure. Because an oblique shock wave is formed ahead of each vortex as it is shed, the second mode also corresponds the frequency with which the shock impinges upon the rear bulkhead. In addition however, there is a system of unsteady pressure waves which characterize the acoustic resonance of the cavity. As each vortex forms, there eventually arises a pressure wave immediately beneath the vortex core, which travels downstream at about the convective speed of the vortex. When this wave impacts the aft bulkhead, it is reflected from the wall and then travels upstream. As the wave travels upstream, it eventually passes another downstream moving wave beneath the next vortex which has formed. Eventually, the upstream moving wave impacts the forward bulkhead and is reflected as a downstream moving wave. By this time, yet another new vortex has already begun to form downstream of the forward lip. The newly reflect wave then catches up with the vortex, and is synchronized with its downstream travel. Because this entire cycle corresponds to the shedding of two vortices, its frequency is one half that of the second mode and thus represents the first mode seen in the spectra. This description, based upon our observations, is consistent with those originally given by Rossiter[54, 55], but differs in some specific details.

6 Leading-Edge Vortex Control on a Delta Wing

Control of the leading-edge vortex generated about a delta wing is a subject of both fundamental and practical interest. Many swept wing flow control studies, utilizing a variety of actuators and strategies, have been documented in the technical literature (see Refs. [56] and [57]). The use of DBD plasma actuators offers an alternative approach for the control of delta wing aerodynamics, which requires no moving parts or complex air delivery systems. At moderate Reynolds numbers, recent progress in the design of efficient plasma actuators has shown the potential for effective control of such vortex flows. In the work reported here, we describe an investigation that explored control of the complex flowfield above a slender delta wing at high angle of attack (AOA), employing the empirical plasma model to represent plasma-induced forces.

The flow about a flat-plate delta wing with the leading edge swept at 75 deg was simulated numerically at a freestream Mach number of 0.1. Computations were performed for the AOA=34 and 38 deg and $Re=25,000$, where the characteristic length l was taken as the root chord. For the AOA=38 deg, a calculation was also carried out at $Re=9,200$ in order to examine the effect of Reynolds number on the location of vortex breakdown. The grid system having an H-H topology, consisted of $247 \times 143 \times 209$ points in the streamwise, spanwise, and normal directions respectively. Solutions were obtained with a sixth-order compact finite-difference discretization, used in conjunction with an eighth-order spatial filter. In order to reduce computational resources, the flows were assumed to be symmetric about the wing midspan, so that a one half span configuration was simulated, with a symmetry plane along the centerline. A computational time step of $\Delta t = 6.25 \times 10^{-5}$ was specified in order to resolve high frequency shear-layer instabilities near the wing apex[58].

A steady (continuous) plasma actuator with the body force directed in the downstream direction, was located on the wing upper surface near the apex as depicted schematically in Fig. 28. This location was found to be most effective among those which were explored, including placement along the wing leading and in the trailing edge region. As noted previously, nondimensional actuator parameters were selected as $BC = 0.018$ and $AC = 0.024$ (see Fig. 6). The actuator was placed at $x = 0.08$, and spanned the region $0.004 \leq y \leq 0.024$. The plasma scale parameter D_c was set to 2400, which was the same value used previously by Gaitonde et al.[33] for plasma control of wing sections.

At high angles of attack, the baseline (no control) delta wing flowfield is characterized by the presence of several interesting vortical features[56, 57, 58, 59]. These include: 1) boundary-layer separation at the sharp leading edge, 2) the formation of a swept shear layer and its roll-up into the primary leading-edge vortex, and 3) vortex breakdown induced by the adverse pressure gradient near the trailing edge. Interaction of the primary vortex with the boundary layer on the wing upper surface, gives rise to secondary vortices. In addition, the three-dimensional “sheet” feeding the leading-edge vortex is known to support both steady and unsteady coherent substructures[58, 60, 61, 62] associated with shear-layer instabilities, and with unsteady boundary-layer separation and vorticity ejection on the wing upper surface.

6.1 Results for AOA=34 deg

The body force of the simulated DBD actuator has a profound impact on the vortex flow structure above the delta wing. As indicated by the time history in Fig. 29, the breakdown location moves downstream following the onset of actuation. After a period of approximately three nondimensional time units, it has traveled beyond the trailing edge of the wing.

Instantaneous flowfields for the baseline and control cases are presented in Fig. 30 as contours in a longitudinal plane passing through the center of the vortex. These include pressure coefficient, streamwise velocity (u), and the streamwise component of vorticity. In the baseline case, the vortex core is observed to burst above the wing surface (Fig. 30a-c). This process is characterized by a loss of both coherence and low pressure in the vortex core, and by the presence of a significant region of reversed streamwise flow. Although the DBD actuator is placed within the secondary vortex region, it has a significant effect on the primary leading-edge vortex. With actuation on, the vortex core remains intact over the entire length of the wing surface (Fig. 30d-f). In addition, the core exhibits higher streamwise velocities relative to the baseline case, even prior to the breakdown location.

A perspective view of the two flowfields is represented by instantaneous cross plane contours of streamwise vorticity and streamwise velocity in Fig. 31, and reveals well defined substructures and high values

of streamwise vorticity in the shear layer of the control case (Fig. 31a). It should be noted in this figure that the left and right halves of the wing solutions correspond to the baseline and control simulations respectively. The shear layer substructures are also apparent along and above the vortex core in Fig. 30f. Structural changes in the shear layer induced by the actuator are shown more clearly in Fig. 32, which provides iso-surfaces of instantaneous streamwise vorticity. In the baseline case (Fig. 32a,b), unsteady substructures are observed being shed from the leading edge just upstream of the breakdown location. They convect around the leading-edge vortex, and eventually lose their coherence through the interaction with the expanding vortex breakdown region. Under the influence of the body force due to actuation, the shear layer rearranges itself into a series of steady helical substructures which emerge downstream of the actuator location (see Fig 32d,e). As previously noted, these substructures are characterized by high values of vorticity that are comparable to those in the vortex core. The origin of steady substructures is linked to the increase in streamwise velocity within the secondary vortex, generated by the actuator. Figure 32b,e show a clear difference in the initial orientation of the shear layer substructures. The stationary structures are inclined towards the wing trailing edge in the direction of the prevailing helical flow, whereas the axes of the unsteady substructures are inclined towards the wing apex.

A comparison of the time-mean flowfields for the baseline and control cases appears in Fig. 33. On the vertical plane through the vortex center (Fig. 33a), the baseline flow exhibits reversed streamwise flow, which is approximately conical, over a significant portion of the region above the wing surface. With actuation (Fig. 33d), there is a reduction of the core streamwise velocity just upstream of the wing trailing edge, but the flow retains jet-like characteristics. Contours of the root-mean-square streamwise velocity fluctuations are displayed in Fig. 33b,e. High levels of fluctuations are present within the vortex breakdown region for the baseline flow. Although, the vortex does not experience breakdown in the control case, there is a region of significant fluctuations near the trailing edge that is associated with vortex core unsteadiness. Time-mean shear-layer structures are indicated in Fig. 33c,f. For the baseline case, these structures have a weak helical secondary pattern, resulting from the secondary breakdown of the unsteady vortices, after they are shed from the wing leading edge. These weak helical substructures correspond in the mean, to the imprint left by vorticity concentrations that were convected by the prevailing spiral flow. Since the control case is characterized by strong stationary structures, the time-mean (Fig. 33f) and instantaneous iso-surfaces (Fig. 32f) are very similar, except near the trailing where flow unsteadiness is present.

6.2 Results for AOA=38 deg

At a higher AOA=38 deg, vortex breakdown in the baseline solution is closer to the apex of the wing ($x_b \approx 0.36$) as illustrated in Fig. 34a,b. Application of the steady plasma force displaces the breakdown downstream to $x_b \approx 0.6$ (Fig. 34c,d). A comparison of iso-surfaces of streamwise vorticity in Fig. 35a,c demonstrates the transformation of the shear layer substructures under influence of the DBD actuator. Simulations at AOA=38 deg were also carried out for $Re=9,200$. Instantaneous iso-surfaces of streamwise vorticity of that computation are presented in Fig. 35b,d. An increase of the relative magnitude of viscous forces results in a smaller change of the vortex breakdown position. One intriguing aspect of this simulation is the alteration of the breakdown structure from a spiral to a bubble type. For delta wing flows, this situation is typically accompanied by a displacement of the vortex breakdown location towards the apex, which is opposite of the present situation. The abrupt nature of vortex breakdown in the control case is also evident for the higher Reynolds number simulation in Fig. 33c. The ability of plasma-based actuation to significantly modify the leading-edge vortex structure and breakdown location may open new avenues for enhanced flight control. For instance, roll control may be achieved without mechanical apparatus by activating DBD devices in an asymmetric fashion.

7 Efficiency Enhancement for Highly Loaded Low-Pressure Turbine Blades

Low-pressure turbines are commonly utilized in the propulsion systems of unmanned air vehicles employed for reconnaissance and combat purposes. Due to a decrease in atmospheric density and reduced engine speeds during high-altitude cruise, such low-pressure turbines may encounter Reynolds numbers, based upon blade axial chord and inlet conditions, below 25,000. In this situation, boundary layers along a large extent of blade surfaces can remain laminar, even in the presence of elevated freestream turbulence levels. These laminar boundary layers are then particularly susceptible to flow separation over the aft portion of blade suction surfaces, promoted by the adverse pressure gradient as the flow turns. This results in a breakdown of the flow, transition to turbulence, blockage in flow passages, and a significant reduction in turbine efficiency.

A number of experimental investigations by Bons et al. [63, 64, 65] and by Sondergaard et al. [66, 67] have explored the use of both steady and pulsed vortex generator jets, which may be actuated upon demand, as a means of flow control in low-pressure turbines. In particular, the work by Sondergaard et al. [67] considered the feasibility of increasing the inter-blade spacing, thereby raising the per blade loading. For practical applications, a higher loading can reduce the turbine part count and stage weight. Increased blade spacing however, is accompanied by more extensive boundary-layer separation on each blade due to uncovered turning, resulting in a further reduction of efficiency and additional wake losses. More highly loaded configurations are therefore only functional when used in conjunction with flow control. Rizzetta and Visbal [68, 69, 36, 70, 71] carried out a series of numerical simulations employing both vortex generator jets and plasma actuators to mitigate separation and improve efficiency for a highly loaded linear cascade of low-pressure turbine blades, that is similar to the experiments cited above. Either of these devices may be activated upon demand, remaining idle at sea level where flow along the blades is attached, and being actuated at altitude when separation occurs. Complete details of the computations are found in Refs. [68, 69, 36, 70, 71], and some of the significant results are summarized below.

Shown in Fig. 36 is a schematic representation of the turbine blade shape, given by the Pratt & Whitney “PakB” research design, which is a Mach number scaled version of geometries typically used in highly loaded low-pressure turbines. [63, 64, 65, 67, 66] This blade geometry has an inlet flow angle $\alpha_i = 35.0$ deg, and a design exit flow angle $\alpha_o = 60.0$ deg. The axial chord to spacing ratio (solidity) is 0.75, resulting in an inter-blade spacing $B = 4/3$.

To conserve computational resources, only a single turbine blade passage was considered, and periodic conditions were enforced in the vertical direction (y) to represent a single turbine stage. A mesh system consisting of several distinct overlapping grids was used to define the flowfield, which are observed in Fig. 37. Figure 37a depicts the O-grid topology of the basic grid about the turbine blade, which was comprised of 348 points in the circumferential direction (I), 189 points in the blade-normal direction (J), and 101 points in the spanwise direction (K). Periodic boundaries along $I_{1u} - I_{2u}$ and $I_{1l} - I_{2l}$ are apparent in the figure. Periodic conditions were also enforced in the spanwise direction. An embedded locally refined region (Fig. 37b) of $(313 \times 185 \times 101)$ grid points in (I, J, K) respectively, was used to capture the correct fluid physics in the actuator and near-wall regions. In order to facilitate application of inflow and outflow conditions to the turbine blade domain, overset grids were utilized upstream and downstream of the blade region, and are provided in Fig. 37c. The total number of grid points in all domains was approximately 12.0×10^6 .

The planar grids appearing in Fig. 37 were uniformly distributed across the span, where the nondimensional spanwise extent of the computational domain is s . In the case of vortex-generating jets, s was taken as the inter-jet spacing of 0.112. For the baseline (no control) and plasma-based control simulations, $s=0.2$. This value of s was found to be adequate to capture the transitional flowfield in the prior investigation of Ref. [37]. Flow variables in the overlapping mesh regions of Fig. 37 were obtained from the aforementioned explicit Lagrangian interpolation formulae, with sixth-order spatial accuracy. The turbine blade axial chord was selected as the characteristic reference length, and the reference Mach number was 0.1. Blockage in the flow passage caused the flow to be retarded, lowering the Mach number at the inflow boundary. The reference Reynolds was then iteratively determined in order to match conditions at the inflow, which corresponded to previous experiments and computations. A more thorough explanation of this procedure, and details of all boundary conditions, can be found in Refs. [68, 69, 36, 70, 71]. The Reynolds number based upon inflow conditions was approximately 25,000.

All solutions were obtained using a fourth-order compact differencing scheme and a sixth-order spatial

filter, with a nondimensional time step $\Delta t = 1.5 \times 10^{-4}$. Unsteady actuation, either vortex-generating jets or plasma control, consisted of a period of time when devices were active, followed by an interval when they were idle. The duty cycle represents the portion of the total duration over which control is active, and was 50% for all results presented here. The analytical description for an amplitude function employing the 50% duty cycle consisted of a series of piecewise continuous cubic and linear functions, and is displayed in Fig. 38. Here, t_d is the portion of the fundamental period t_p over which the device is active. The duty cycle is given by the ratio $t_d/t_p \times 100$ expressed as a percentage. This amplitude function is then appended as a factor to the vortex jet exit velocity or plasma force magnitude in order to create pulsed control. It should be noted that the applied waveform introduces multiple harmonics of the primary frequency, as was demonstrated in Refs. [72] and [35]. The period illustrated in Fig. 38 was represented by 1300 time steps, corresponding to a nondimensional frequency of 7.56.

From computed time-mean flowfields, control effectiveness was quantified by calculation of the integrated wake total pressure loss coefficient C_w , defined as

$$C_w = \frac{1}{s(y_{\max} - y_{\min})} \int_0^s \int_{y_{\min}}^{y_{\max}} \left(\frac{P_{ti} - \bar{P}_{to}}{P_{ti} - \bar{p}_i} \right) dy dz. \quad (40)$$

Equation 40 was evaluated along the upstream boundary of the downstream mesh in Fig. 37c, which is located 0.67 chords downstream of the blade trailing edge.

7.1 Results for Vortex-Generating Jets

In the above-mentioned experimental studies[63, 64, 65, 66, 67], jets were created by blowing air through holes which had been drilled in the blade surface at a pitch angle of 30 deg and a skew angle of 90 deg. The jets were situated at the time-mean separation location, and the geometry is indicated in Fig. 39. Here, the pitch is defined as the angle the jet makes with the local surface, and the skew is the angle of the projection of the jet on the surface, relative to the “local freestream” direction.[65] The size of the drill used to develop the holes is commonly referred to as the jet diameter, which was 0.001 m. Because of the orientation however, the jet exit geometric shape is elliptic as seen in Fig. 39, and the jet exit velocity vector has components only in the blade-normal and spanwise (z) directions. In order to simulate the flow within the jet nozzle, additional overset meshes were employed in the jet exit region, and interior to the blade geometry. These are evident in Fig. 39. A description of inflow conditions to the jet nozzle is given in Refs. [68] and [69].

Time-mean surface pressure coefficient distributions for the baseline (no control) and flow control computations are presented in Fig. 40. For the flow control cases, these distributions were obtained at the spanwise location of the periodic boundary between two jets. As indicated in the figure, the jet was positioned at $x = 0.37$, which coincides with the separation point of the baseline solution. The large plateau region in the baseline distribution is characteristic of massively separated flow. Because of reduced blockage and increased inflow velocity, the effect of flow control is to decrease the pressure on the upstream portion of the suction surface, while increasing it downstream, relative to the baseline case. Separation occurs at $x = 0.56$ for the steady blowing result, and at $x = 0.58$ for pulsed injection. Only minor differences, most noticeable near the jet, are observed between the two flow control solutions. Also seen in the figure, is a coarse-mesh distribution for the baseline case, which indicates little sensitivity to grid resolution, except near the trailing-edge region. More extensive results of the grid resolution study for the baseline case are found in Ref. [73].

Time-mean contours of the streamwise component of velocity and spanwise component of vorticity are shown in Fig. 41. Contours for the flow control results were taken at the plane of the periodic boundary between jets, while those of the baseline case have been spanwise averaged. An increased region of attached flow due to flow control is apparent, resulting in a decrease of the wake thickness. Maintaining attached flow and decreasing the extent of the wake are exhibited by the flow control results.

Spanwise turbulent kinetic energy wave-number spectra are provided in Fig. 42. These spectra were generated along lines in the z direction at a nondimensional distance of $n = 0.03$ from the blade surface. This location ($n = 0.03$) is approximately equal to one half of the boundary-layer thickness of the time-mean velocity profile upstream of separation. At the two most upstream stations ($x = 0.50, 0.70$), E_{k_z} is higher for the flow control cases than that of the baseline due to energy being added to the flow. In the downstream region ($x = 0.90$), flow control has mitigated separation and the associated breakdown into a more chaotic

situation, so that the turbulent kinetic energy of the baseline case is higher. Because of the low Reynolds number, only a small portion of the spectrum at low wave number lies in the inertial range.

Instantaneous contours of the streamwise velocity component and spanwise vorticity appear in Fig. 43. Once again, the baseline result was extracted at the midspan location, while those of the flow control cases were situated between control jets. Similar to the time-mean contours of Fig. 41, it is noted that flow control maintains attached flow and decreases the vertical extent of the wake relative to the baseline case. Unsteady structures are visible in separated flow regions. It is seen in the flow control cases that vorticity (Fig. 43b) is being generated in the boundary layer in close proximity to the blade surface. When the boundary layers separate in these situations, it is much less dramatic than in the uncontrolled case. For the baseline solution, the extensive unsteady separated flow region has a richer content of small scale structures due to breakdown and a transition to a more complex situation.

Turbulent kinetic energy frequency spectra are observed in Fig. 44. The data used to generate these spectra was collected at $n = 0.03$, similar to that of Fig. 42. Like the spanwise wave number spectra of Fig. 42, the frequency spectra for the flow control cases is substantially higher than that of the baseline result at the upstream stations ($x = 0.50, 0.70$) because of energy addition. At $x = 0.50$, the discrete peaks in E_ω for the pulsed injection case correspond to harmonics of the forcing frequency. The occurrence of this behavior was described in detail in Ref. [73]. As noted previously, turbulent energy of the baseline case exceeds that of the flow control results near the blade trailing edge ($x = 0.90$).

A three-dimensional representation of the flow is depicted by iso-surfaces of vorticity magnitude in the trailing-edge region seen in Fig. 45. The value of iso-surfaces correspond approximately to that at the edge of the shear layer upstream of separation. Both the vertical and spanwise extent of the turbulent structures are visible for each case.

For both the steady and pulsed cases, the fundamental effect of vortex-generating jets was to energize the blade boundary layer due to the transfer of fluid momentum and mixing. This helped maintain attached flow along the blade surface for a distance of 19-21% greater than that of the baseline case. As a result, wake total pressure losses were decreased by 53-56%. In the pulsed case, mixing was enhanced through unsteady forcing. Although no forcing was employed with the steady case, the jet was inherently unstable, and broke down shortly after exiting the nozzle. This behavior also served to increase mixing. Because of the 50% duty cycle, the pulsed case required less mass flow than the steady jet to achieve a similar improvement in efficiency.

7.2 Results for Plasma-Based Control

Extensive simulations for the highly loaded low-pressure turbine blade were performed by Rizzetta and Visbal[36, 70, 71] in order to explore plasma-based flow control strategies. During the study, many aspects of control were investigated including the magnitude of the plasma force required to establish control, the use of both continuous and pulsed actuation, the effect of forcing frequency and duty cycle for pulsing, the location for the placement of actuators, the use of both full span and finite distributed arrays of actuators, and the direction of the plasma-induced force. For the later of these, the actuators were oriented such that the force was directed in the coflowing, counterflowing, or spanwise directions. A primary objective of these studies was to determine effective plasma-control arrangements which required minimal power usage. Some results of these efforts are reported below, all of which were obtained for pulsed actuation with a value of the plasma scale parameter $D_c = 25$, that represents a low energy demand.

Configurations considered in these results are represented in Fig. 46, where the arrows indicate the actuation direction. It can be noted in the figure, that cases **A**, **B**, **C**, and **D** correspond to counterflow actuation, while cases **E** and **F** have spanwise oriented actuators. Because configurations **E** and **F** were less effective arrangements, no results for those cases will be presented here.

Time-mean surface pressure coefficient distributions are displayed in Fig. 47. These results were obtained along the centerline of the computational domain for each solution. The large plateau region in the baseline distribution is characteristic of a massively separated flow, as was noted in Fig. 40 for the vortex-generating jet solutions. Again, the dominant effect of flow control is to reduce separation of the time-mean flowfield on the blade suction surface. Cases **A**, **B**, and **C** effectively maintained attached flow to the blade trailing edge, thus completely eliminating the plateau. Although the finite-span case (configuration **D**) reduced the extent of separation, a smaller plateau is still present.

A composite visual comparison of the flowfields for these cases is exhibited in Fig. 48. Contours of streamwise velocity are displayed in the top row of the figure, streamlines in the middle row, and pressure coefficient (C_p) at the bottom. Massive separation in the baseline case is apparent. Results depicted here are consistent with those of the surface pressure distributions (Fig. 47). Streamlines illustrate the massively separated flow of the baseline case. Completely attached time-mean flow for cases **A**, **B**, and **C** is apparent in the figure. A reduction of the separated flow region is evident for case **D**. The thin wakes for cases **A**, **B**, and **C**, relative to the baseline flow, are visible in the streamwise velocity contours. The effect of separated flow regions occurring for the baseline case and configuration **D**, is reflected in the C_p contours.

Spanwise turbulent kinetic energy wave-number spectra are shown in Fig. 49. These spectra were generated at $n = 0.03$, similar to those of Fig. 42. Because the spectra for configuration **B** was identical to that of **C**, and case **D** was similar to the baseline, those results are not presented. At the most upstream station ($x = 0.5$), case **C** contains more energy than either the baseline or configuration **A** solutions. This is also true further downstream at $x = 0.7$. And although energy is being added to the flow, it is believed this situation reflects an early transition to turbulence. Near the trailing edge ($x = 0.9$), all situations are similar, toward the end of the transition process. It should be noted that these comparisons are performed at a location very close to the blade surface. Away from the blade, the total energy contained in the large structures of the massively separated region for the baseline case is very large. As noted previously, only a small portion of the spectrum at low wave number for $x = 0.9$ lies in the inertial range due to the low Reynolds number.

Provided in Fig. 50 are instantaneous streamlines at the blade midspan for configuration **A**. Seen in the figure, is the flowfield near the actuator location at four frames during the pulsing cycle. For $t/t_p = 0.0$, control has been inactive for one half of the pulsing cycle, and the flow is attached. At $t/t_p = 0.2$, actuation has taken place for 20% of the cycle, creating a small separation bubble at the blade surface. By $t/t_p = 0.4$, the region of reversed flow has grown in size. Finally, when $t/t_p = 0.6$ the active portion of the cycle has ended, and the separation bubble begins to convect downstream.

A composite representation of the instantaneous flowfields for these cases appears in Fig. 51. Contours of streamwise velocity and spanwise vorticity along the centerline plane are observed in the top and middle rows of the figure respectively, while spanwise vorticity on the blade surface viewed from above, is at the bottom. The middle row of spanwise vorticity is particularly useful for understanding the control mechanisms. It was shown in Ref. [36] for configuration **A**, that control was imposed by modifying the inherently unstable boundary layer near its separation point. The plasma actuator forced the boundary layer to roll up into small vortices just downstream of the actuator location. These vortices were shed at a frequency one half that of the pulsed control, and convected downstream at a distance from the blade surface which was not large. This greatly enhanced mixing, and brought higher momentum fluid into the boundary layer, thereby maintaining time-mean attached flow and reducing wake losses. The fairly coherent vortical structures are visible in the spanwise vorticity contours (middle row). Dark portions of the surface vorticity (bottom row) signify regions of attached flow.

For configuration **B**, actuation was applied further upstream from separation than in configuration **A**, and expedited transition. As a result, no coherent vortices evolved, and the flowfield was dominated by fine-scale fluid structures. Configuration **C** was specifically designed to eliminate fluid coherence. It was believed that coherence could promote structural fatigue, and be detrimental to instrumentation and acoustic signature for turbine applications. The approach with configuration **C** was to apply a second counterflow actuator downstream of the first, to help break down coherent structures. In addition, the second actuator was of finite span, so as to reduce two-dimensional effects. It is noted for configuration **C** in Fig. 51 that only fine-scale structures are present. Both configurations **B** and **C** have wake total pressure loss coefficients that are slightly less than that of configuration **A**.

Configuration **D** considered only a single finite-span counterflow actuator, at the same location as that of configuration **A**. Although some control was exerted in this situation, the actuation was less effective. The arrangement failed to manipulate the boundary layer in a useful manner, or to generate transition. Effectiveness arose only through enhanced mixing.

Turbulent kinetic energy frequency spectra at $n = 0.03$ for configurations **A** and **B** are displayed in Fig. 52. As occurred for pulsed vortex-jet control, discrete peaks in E_ω near the actuator location ($x = 0.5$) with plasma actuation, correspond to harmonics of the pulsing frequency. At $x = 0.7$, sub-harmonics of the pulsing frequency have been excited in the spectra of configuration **A**. This phenomenon was caused by the

small vortices generated in the boundary layer, downstream of the actuator. No sub-harmonics are apparent for configuration **B** (or configuration **C**, not shown), as the small coherent vortical structures have been suppressed. Turbulence levels of configuration **A** are higher than the baseline at $x = 0.5$ and $x = 0.7$ due to energy being added to the flowfield. Peak levels of configuration **B** are higher than those of configuration **A** at these location, although the broadband content is lower. Farther downstream in the trailing-edge region ($x = 0.9$), all spectra attain a similar level. Peaks associated with actuation in configuration **A** at this location, are not present for configurations **B** (or configuration **C**, not shown). A small inertial range in the spectra can be observed in all results.

A three-dimensional representation of the flow in the trailing-edge region for configurations **A** and **C** is depicted in Fig. 53 by isosurfaces of vorticity magnitude, which have been colored by the streamwise velocity. The value of the isosurfaces corresponds approximately to that at the edge of the shear layer upstream of separation. Massive separation is evident in the baseline flow, as are two-dimensional coherent structures for configuration **A**. The elimination of these structures in configuration **C** is noticeable. Configurations **A**, **B**, and **C** were able to achieve a reduction in wake total pressure losses of 81-86%. This was better than that attained with vortex generating jets. For configuration **D**, losses were only lowered by 39%.

Table 2: Hump flow reattachment locations

case	experiment[75, 76]	LES	RANS
baseline	1.11 ± 0.003	1.139	1.23
suction	0.94 ± 0.005	0.978	1.14
blowing/suction	0.98	1.097	1.29

8 Separation Control for a Wall-Mounted Hump Model

The control of separation for wall-bounded flows is an important and challenging area for numerical simulation. In order to define some of these challenges and assess current capabilities, the CFD Validation on Synthetic Jets and Turbulent Separation Control Workshop, sponsored by NASA Langley Research Center, was held at Williamsburg, VA in March of 2004.[74] The main objective of the workshop was to develop a comprehensive database of experiments employing flow control for subsequent validation and comparison with various computational simulation techniques. One of the cases at this workshop corresponded to flow over a wall-mounted hump model, which was investigated experimentally[75, 76] with and without flow control. In the control cases, both steady suction and zero net mass flux blowing/suction were considered.

The hump geometry simulates the upper surface of a 20% thick Glauert-Goldschmied airfoil, with a chord of 0.4200 meters, a maximum height of 0.0537 meters, and a span of 0.5842 meters. A slot was situated at the 65% chord location, and connected to an internal plenum for control purposes. The geometry of the configuration and overset mesh system are illustrated in Fig. 54. The hump portion of the computational domain was described by $(818 \times 151 \times 165)$ points in the (I, J, K) directions, while a grid of $(41 \times 133 \times 165)$ defined the plenum. Both steady suction and oscillatory blowing/suction flow control were applied via boundary conditions enforced at the inlet to the plenum. Complete details of the simulations are documented in Refs. [77, 78, 79].

Experimental measurements were conducted at $Re = 9.36 \times 10^5$, but the simulations were performed for $M_\infty = 0.10$ and $Re = 2.0 \times 10^5$, where the model chord was used as the characteristic length. A lower Reynolds number was employed in the computations to maintain LES resolution with acceptable levels of resource requirements. The large-eddy simulations utilized a fourth-order compact difference scheme and a sixth-order spatial filter. Although not central to the main purpose of the computations, RANS simulations were also carried out and are shown below for comparison. A full description of the RANS approach can be found in Refs. [80] and Morgan:AIAAJ2006.

8.1 Features of the Time-Mean Flowfields

A comparison of the time-mean surface pressure coefficients is presented in Fig. 55. The experimental data, LES, and RANS solutions all display a large peak near the mid-chord of the hump, which is associated with flow acceleration. A small plateau region downstream of the flow control slot is characteristic of flow separation. All simulations compare well with the experiment upstream of the control slot, where the flow is attached. The LES solutions compare reasonable well with the experiment in the separated flow and wake regions. Deficiencies of the RANS computations are particularly evident for the suction and oscillatory cases.

Comparisons of time-mean streamwise velocity contours are indicated in Figs. 56-58. For the baseline case (Fig. 56), the LES and experiment have stronger reverse flow than the RANS, in the near-wall region for $0.8 < x < 1.0$. The main difference between the LES and the experiment, is that the region of fastest reverse flow occurs 5% of the chord further upstream for the LES than is observed in the experiment. The RANS solution clearly shows a longer separation bubble than either the experimental or LES results. Reduction of the separated flow region by applying suction is apparent in Fig. 57. Control appears less effective with blowing/suction in Fig. 58. For both control cases, the RANS solution predicts a larger separated flow region than either the LES or the experiment, which compare favorably. Locations of the time-mean flow reattachment points are provided in Table 2.

8.2 Features of the Unsteady Flowfields

Contour plots comparing the time-mean Reynolds stresses are shown in Figs. 59-61. For the baseline case (Fig. 59), it can be clearly seen that the LES developed a smaller, thinner region of minimum Reynolds stress which was located further upstream than in the experiment. The RANS solution does not reach the same levels of Reynolds stress as that of the experiment and LES. The region of minimum magnitude of the Reynolds stresses for the RANS result is significantly smaller and is located further downstream. Reynolds stress profiles for steady suction are compared in Fig. 60. Overall the LES and experimental contours have the same qualitative shape and magnitude. The LES however, did not develop the lowest magnitude of Reynolds stress that occurred in the experiment. Contours of the RANS solution display generally lower values of Reynolds stress. Exhibited in Fig. 61 are contour plots of Reynolds stress for the blowing/suction case. Here, the LES fails to attain the same minimum levels of the experiment. This is attributed to the circumstance that the same magnitudes of blowing/suction were employed for the LES as that of the experiment, but the Reynolds number was considerably lower.

In order to represent characteristics of the unsteady flowfield for the oscillatory blowing/suction case, phase-averaged planar contours of the spanwise component of vorticity were collected experimentally. These are compared with the computations for four values of the phase angle in Figs. 62-65. The phase angle $\Theta=90$ deg corresponds to the maximum blowing rate and $\Theta=270$ deg to maximum suction in the oscillatory cycle. Overall, both the LES and RANS solutions have good agreement with the experiment in the general behavior of the flow, including size and locations of the vortex generated by the pulsing. The RANS results display more coherent structures throughout the blowing and suction cycle, which do not dissipate as rapidly in the wake.

Instantaneous streamwise velocity contours in the $x - y$ plane and iso-surfaces of vorticity magnitude for the blowing/suction case are seen in Fig. 66. We note that this figure has been stretched by a factor of two in the spanwise direction to enhance visualization. The turbulent boundary layer with multiple spanwise structures can be seen in the upstream region. These turbulent structures diminish as the flow accelerates over the hump. After separation, the effect of pulsing is evident in the large spanwise structures that convect downstream.

9 Summary and Conclusion

The description of a high-order finite-difference scheme, suitable for large-eddy simulations which consider active flow control, has been presented. The numerical method is predicated upon an implicit approximately-factored time-marching approach, employing Newton-like subiterations, that is efficient for wall-bounded flows. Spatial derivatives are evaluated via an implicit compact approximation, thereby reducing the associated dispersion error. The differencing technique is used in conjunction with a similar implicit high-order low-pass Pade-type spatial filter, that augments robustness by adding dissipation only for under-resolved high-frequency spatial modes of the solution. Because of this selective nature of the filtering process, it also serves as an implicit subgrid-scale stress model. Flexibility of the method for application to geometrically complex configurations is provided by an overset grid approach. This allows structured meshes to be utilized and high-order spatial accuracy to be achieved. A high-order Lagrangian interpolation procedure maintains accuracy at overlapping grid boundaries. Domain decomposition is applied for processing on parallel computing platforms.

Several computational examples of active flow control simulations have been provided to illustrate utility of the scheme. These include suppression of acoustic resonance in supersonic cavity flowfields, the control of the leading-edge vortex of a delta wing, the enhancement of efficiency for a transitional highly loaded low-pressure turbine blade, and separation control for a wall-mounted hump model. Active control devices considered in these simulations consisted of both steady and pulsed blowing, plasma actuators, vortex generating jets, continuous suction, and oscillatory blowing/suction. The variety of these mechanisms serve to indicate a general applicability of the methodology.

A number of “pacing” items which require additional development, and that can extend the potential of the scheme to other applications, are enumerated here. The most problematic of these is the ability of simulations to capture shock waves, and still maintain both stability and high-order spatial accuracy. Although the external flowfield of the cavity computation presented above was supersonic, the Mach number was sufficiently low ($M_\infty=1.19$) that it did not adversely impact the high-order techniques. Large-eddy simulations of supersonic compression ramp flows carried out by Rizzetta and Visbal[39] with $M_\infty=3.0$ employed a hybrid shock capturing approach. Although this technique worked well for a single shock and a two-dimensional geometry, it was not deemed to be flexible enough for more general applications. Recent investigations by Visbal and Gaitonde[81] and by Croker and Gaitonde[82] have explored alternative methods.

The current implementation for communicating information at overset boundaries is by a pre-processing operation to obtain interpolation stencils. This is true for situations where data is exchanged by direct injection which is used to accommodate domain decomposition for parallel processing, as well as the more general circumstance of overlapping topologically distinct grids. The ability to represent translating and/or deforming meshes that alter their donor and receiver stencils during the course of a simulation, is precluded by this approach. One of the features considered for future development is the capability of “on the fly” interpolation, that would allow simulation of relative motion between bodies.

Finally, it may also be possible to provide an adaptive component to the numerical scheme, and in particular to the spatial filter. This would permit the order of the filter to increase locally, and enhanced resolution which responds as features in the solution evolve. And unlike adaptive meshing, no improved grids would need to be generated as part of the process.

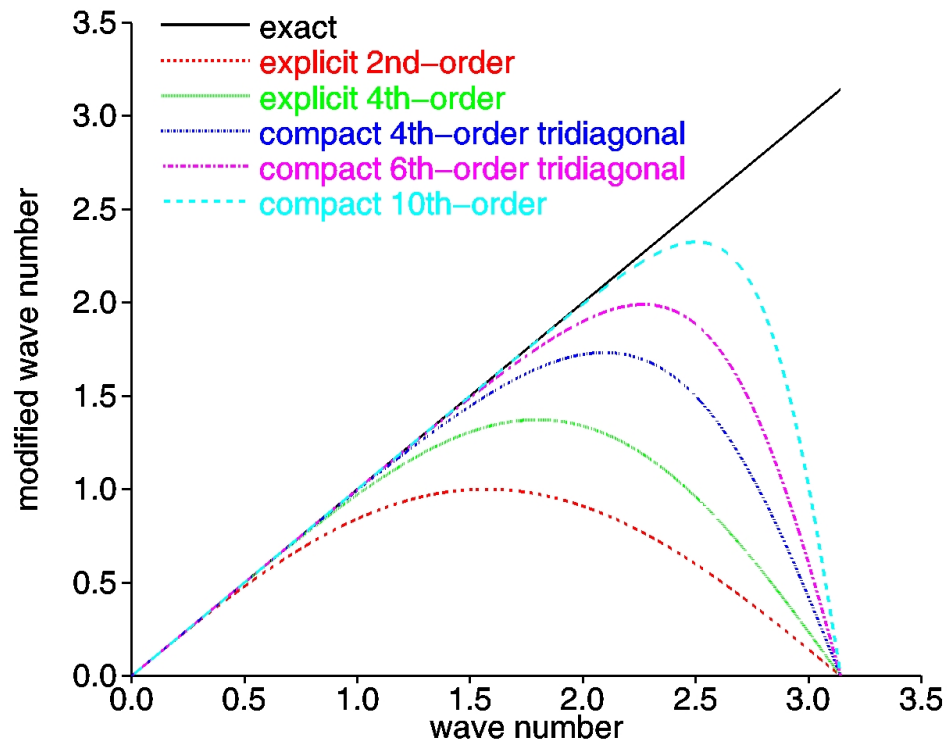


Figure 1: Dispersion-error characteristics of various spatial discretizations for one-dimensional periodic functions.

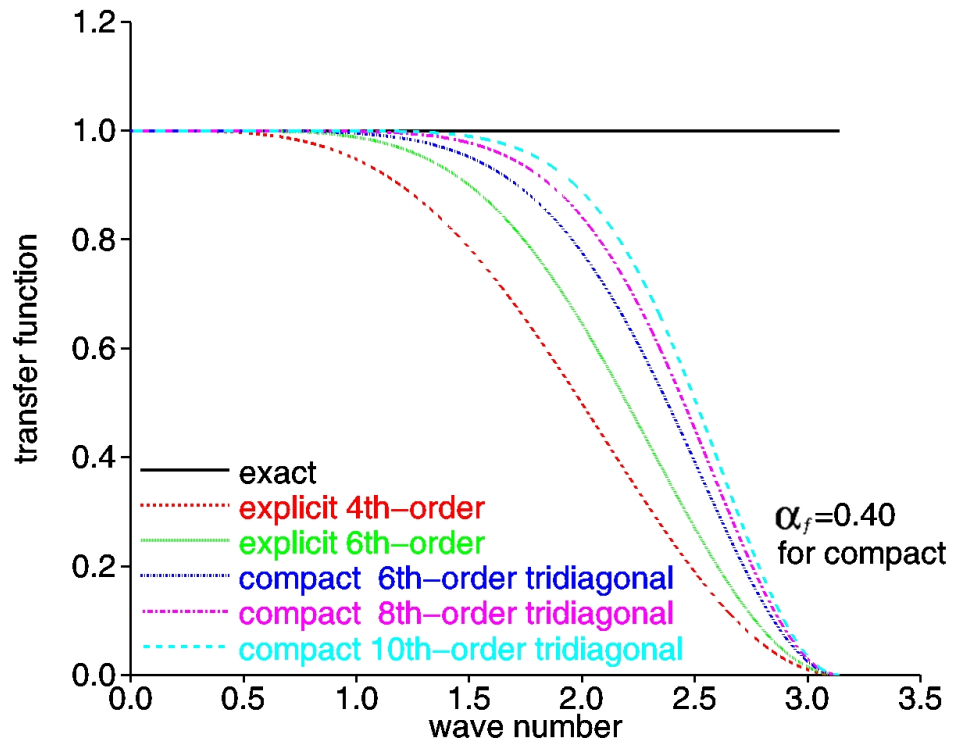


Figure 2: Dissipation-error characteristics of various filters for one-dimensional periodic functions.

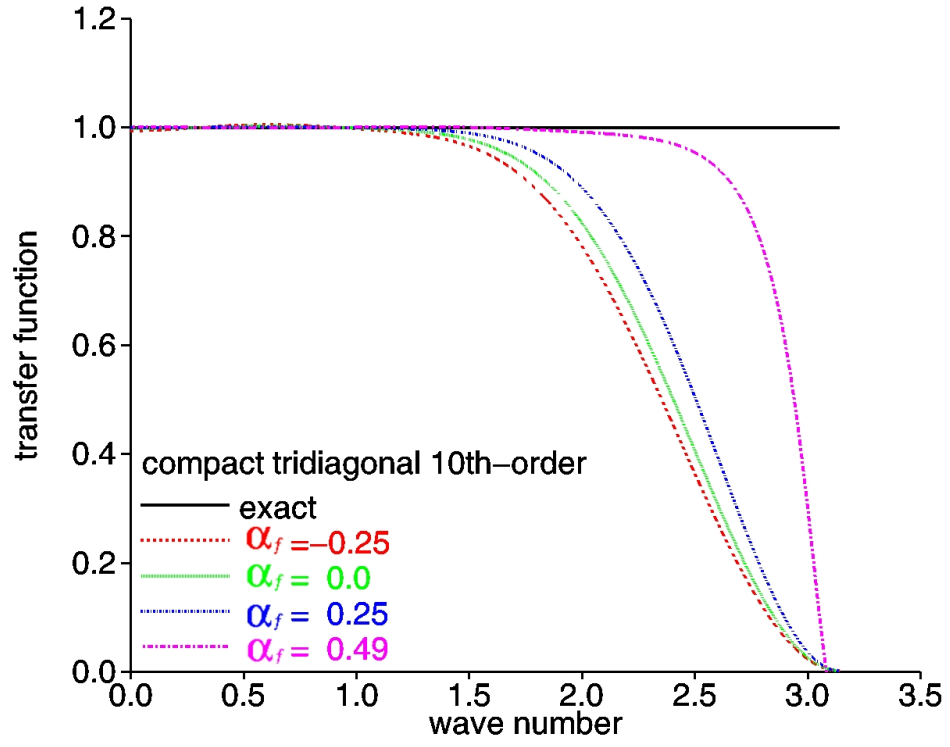


Figure 3: Dissipation-error characteristics with various values of the implicit coefficient α_f and a 10th-order filter for one-dimensional periodic functions.

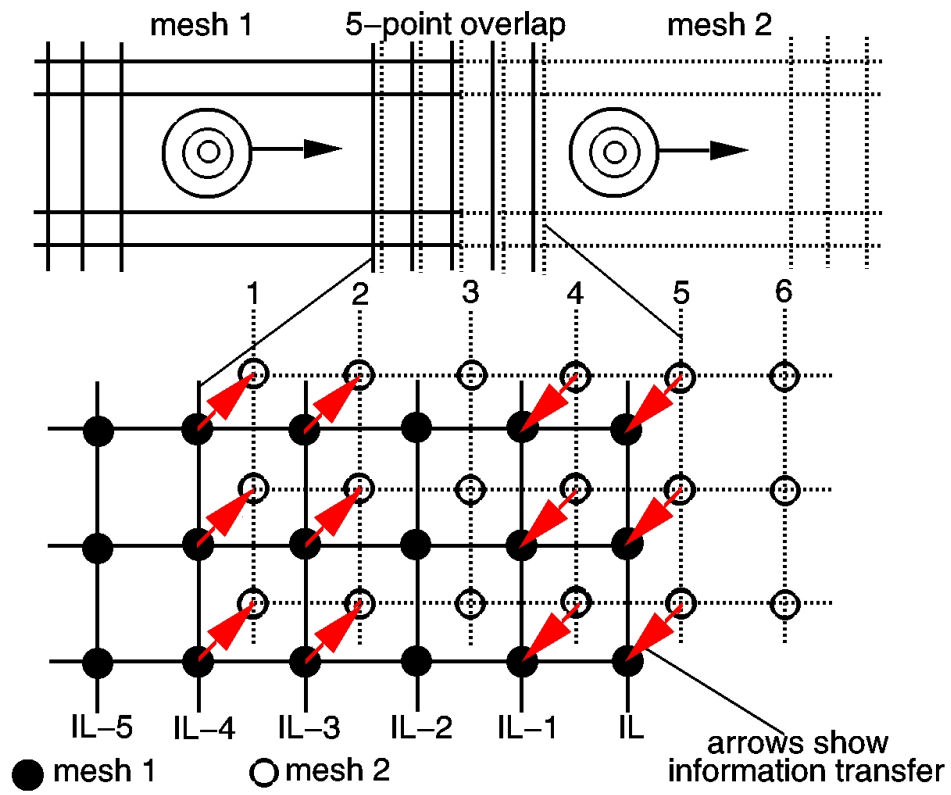


Figure 4: Schematic illustration of five-point mesh overlap.

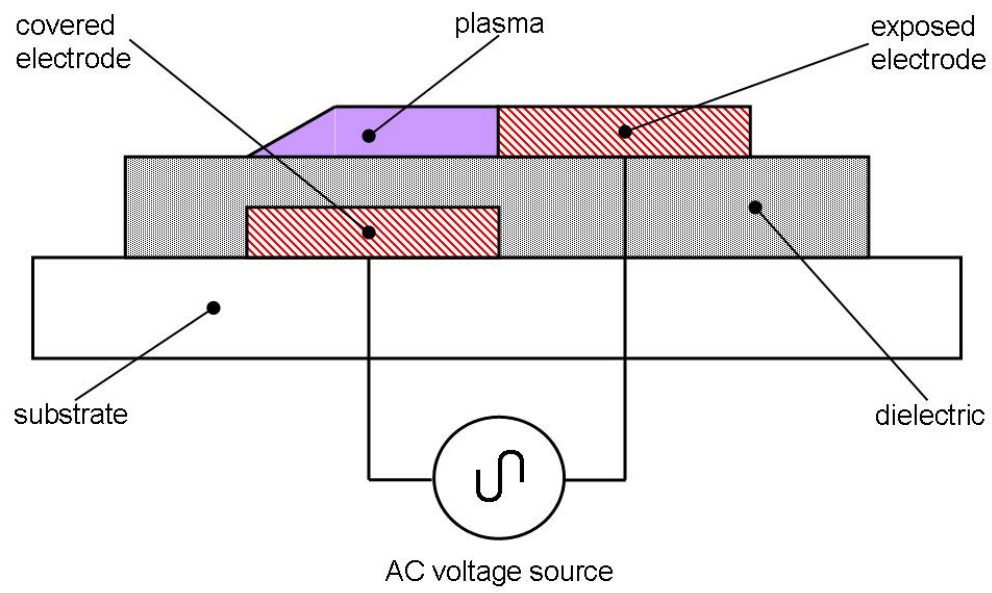


Figure 5: Schematic representation of plasma actuator.

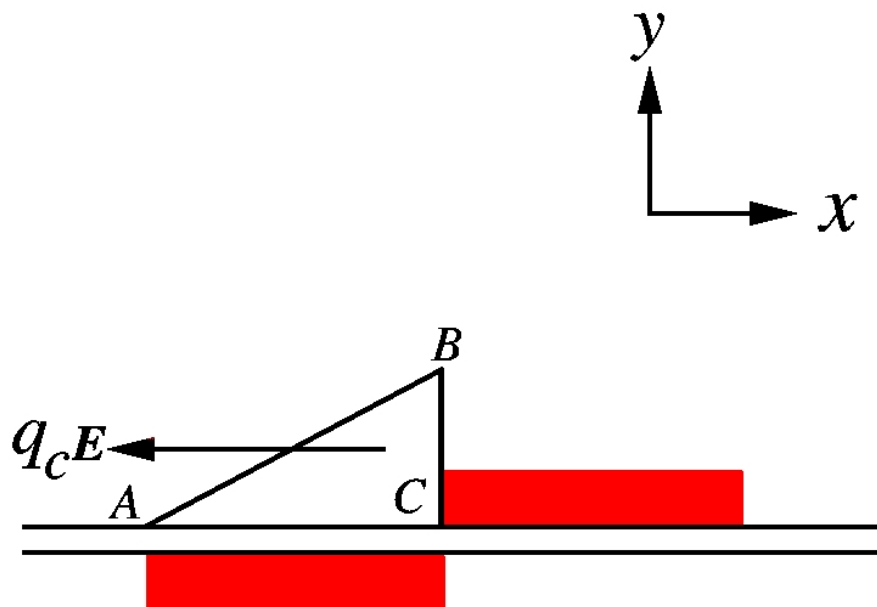


Figure 6: Geometry for the empirical plasma-force model.

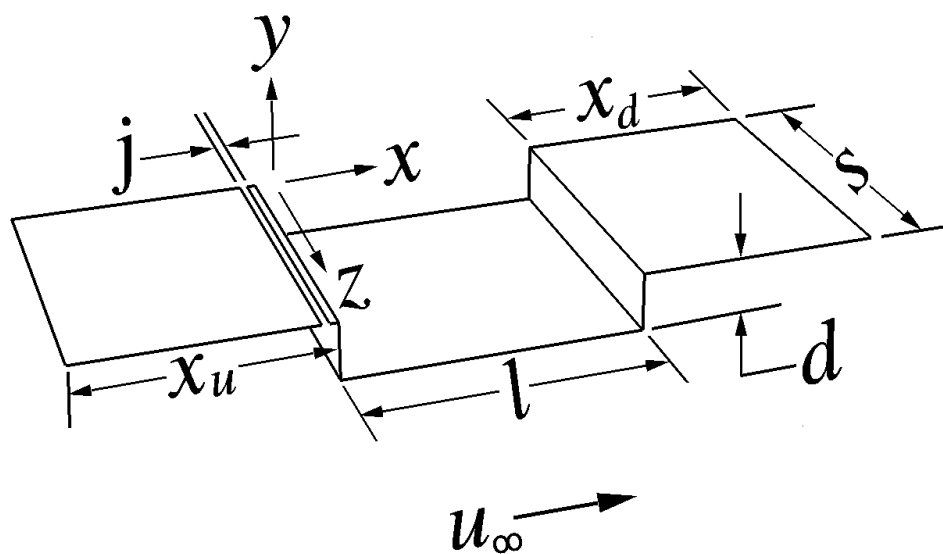


Figure 7: Schematic representation of the cavity configuration.

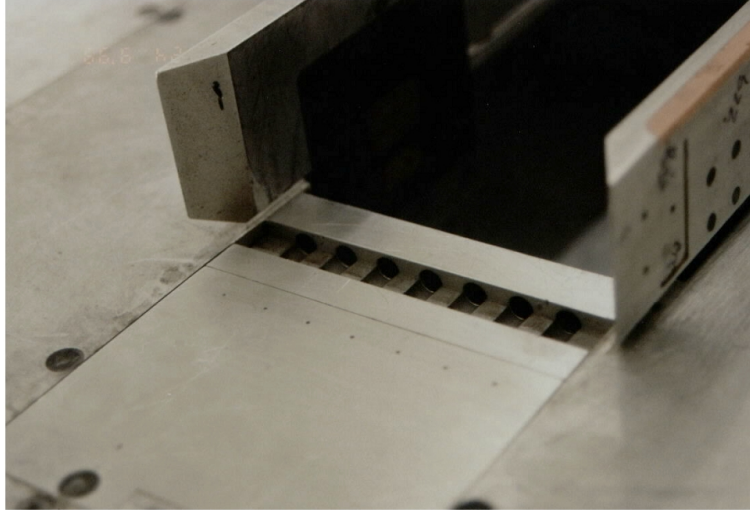


Figure 8: Experimental cavity configuration.

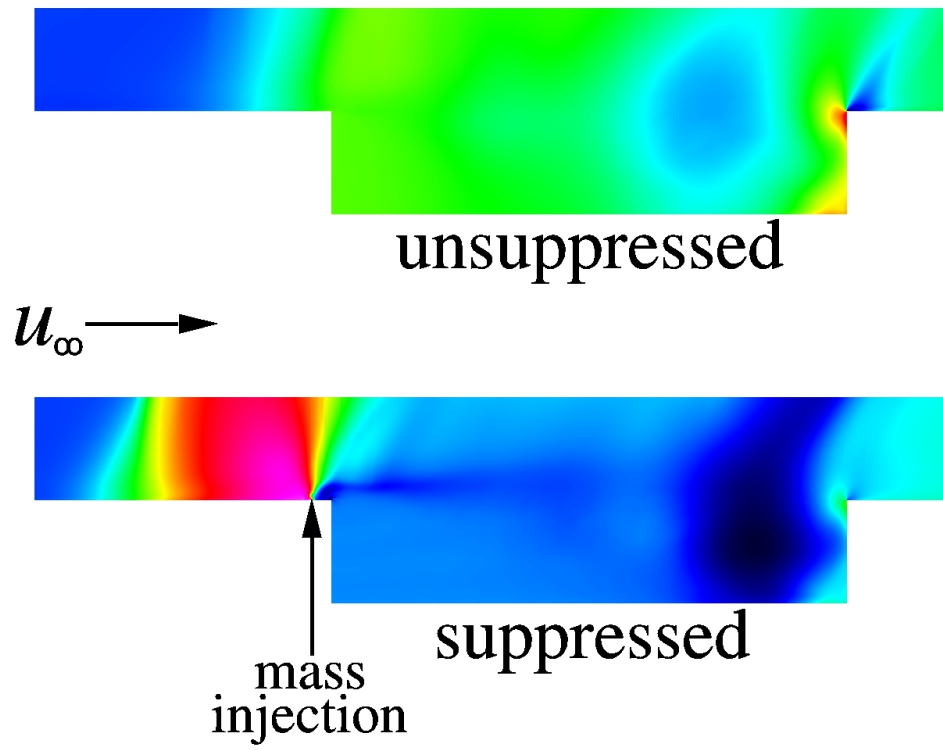


Figure 9: Spanwise-averaged time-mean pressure coefficient contours.

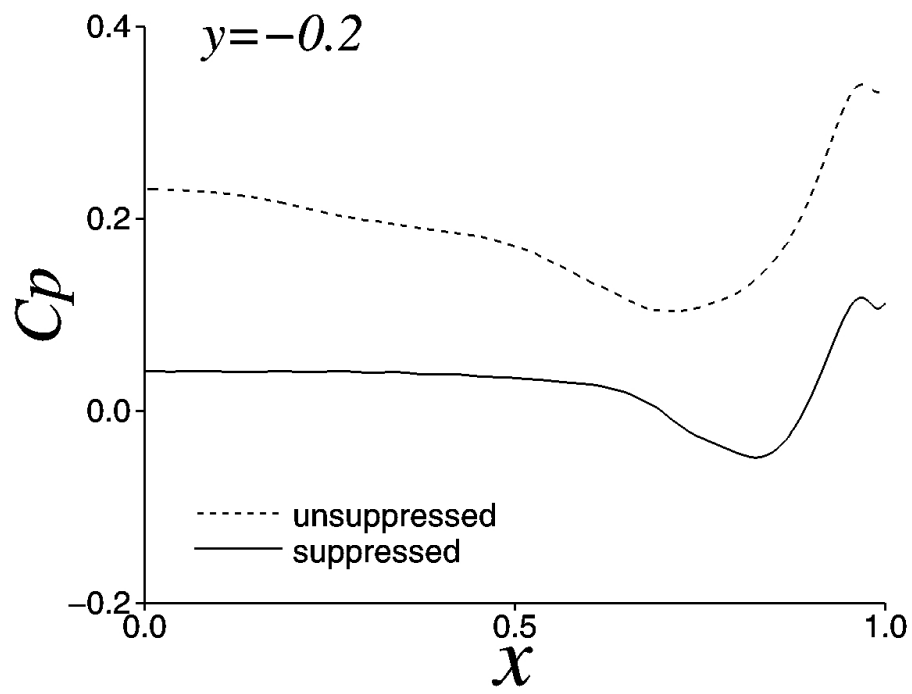


Figure 10: Spanwise-averaged time-mean pressure coefficient distributions on the cavity floor.

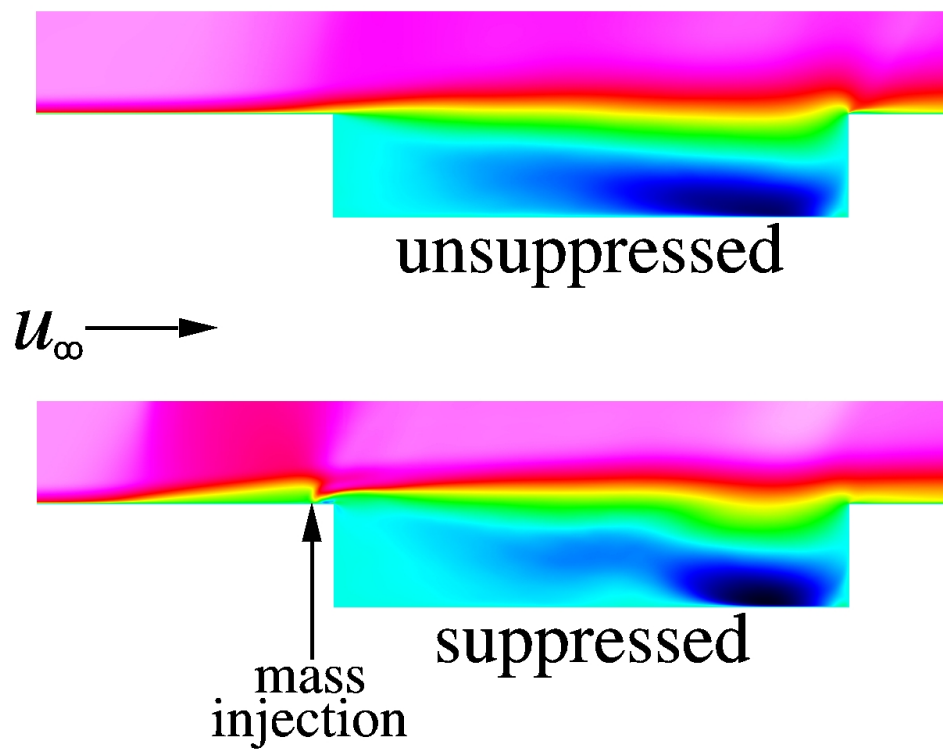


Figure 11: Spanwise-averaged time-mean streamwise velocity contours.

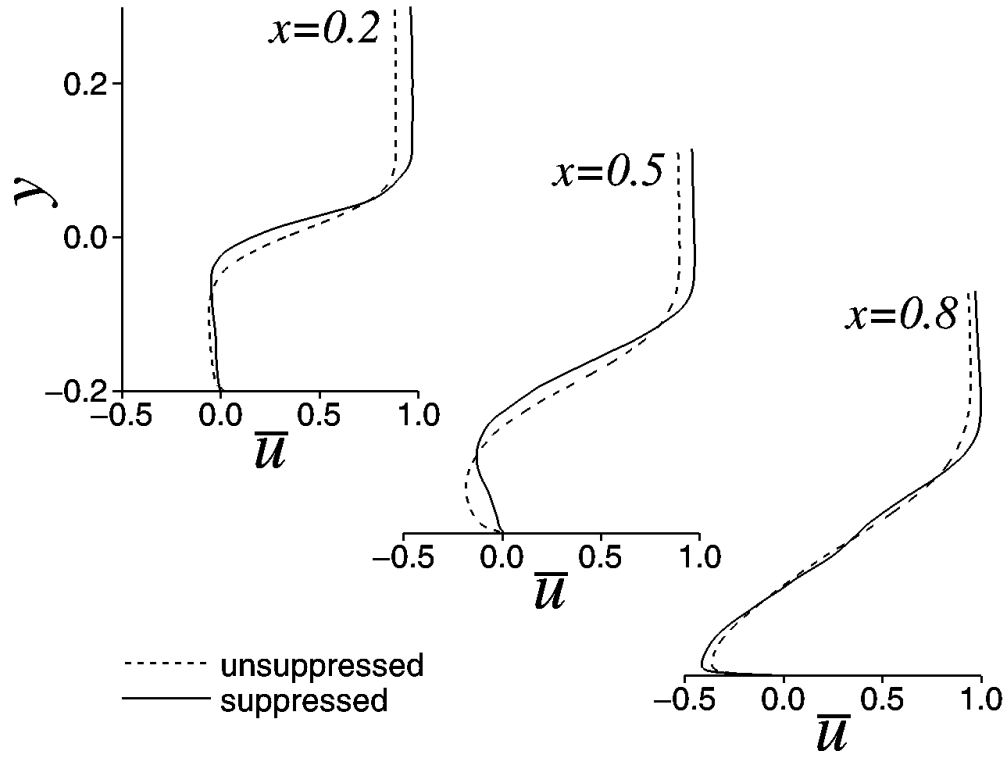


Figure 12: Spanwise-averaged time-mean steamwise velocity profiles.

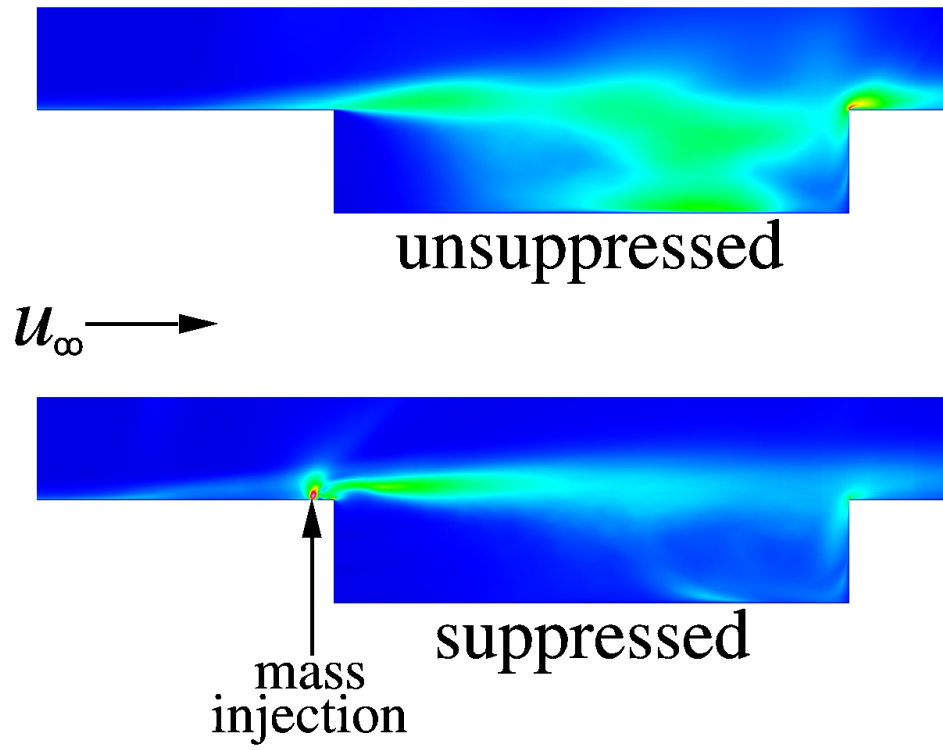


Figure 13: Spanwise-averaged time-mean turbulent kinetic energy contours.

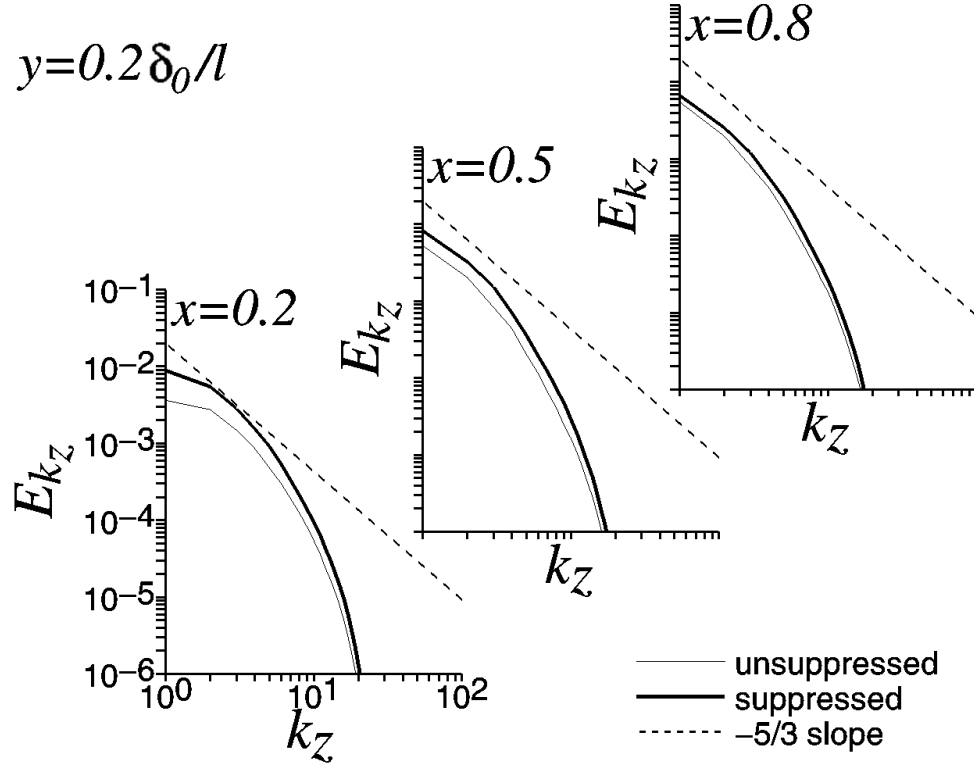


Figure 14: Time-mean turbulent kinetic energy spanwise wave-number spectra at $x = 0.2, 0.5, 0.8$ and $y = 0.2\delta_0/l$.

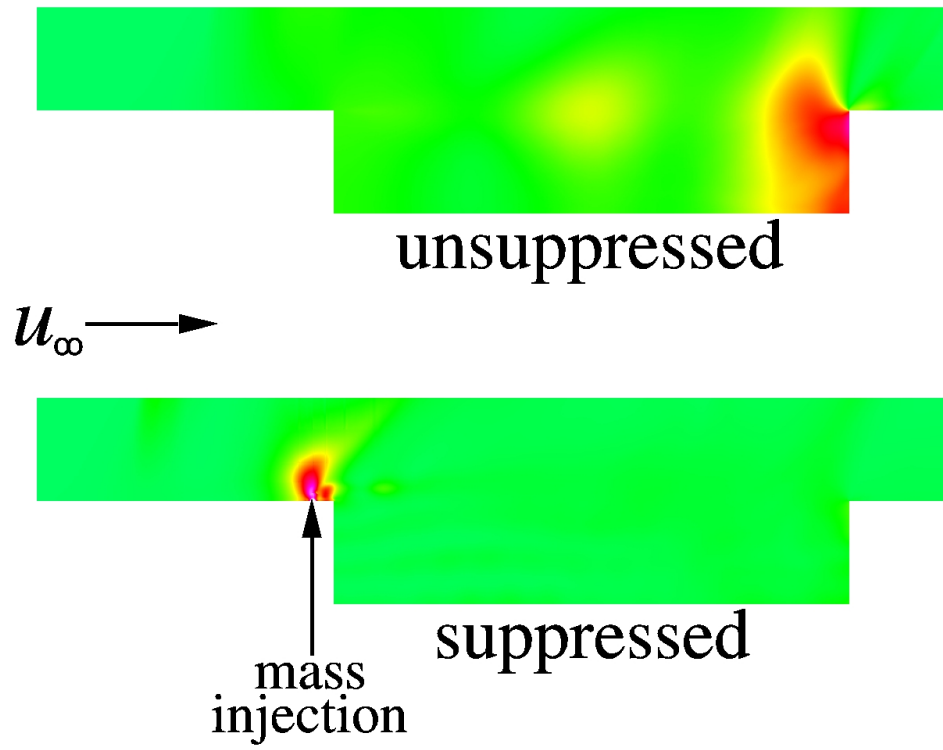


Figure 15: Spanwise-averaged time-mean fluctuating pressure contours.

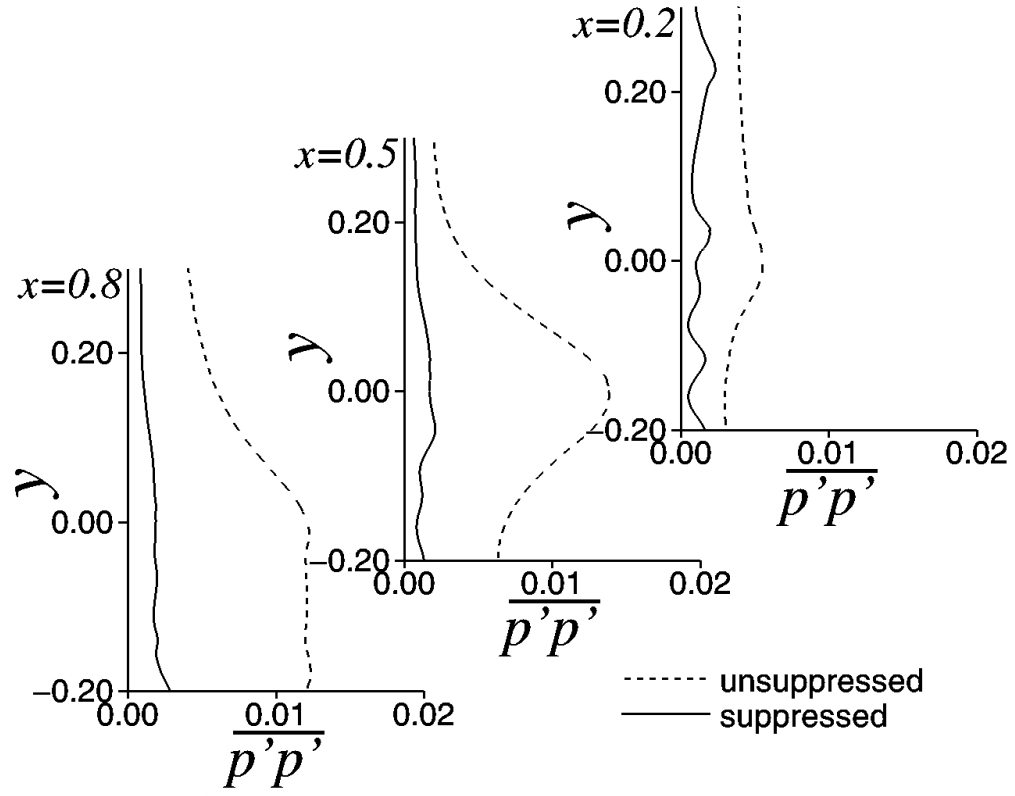


Figure 16: Spanwise-averaged time-mean fluctuating pressure profiles.

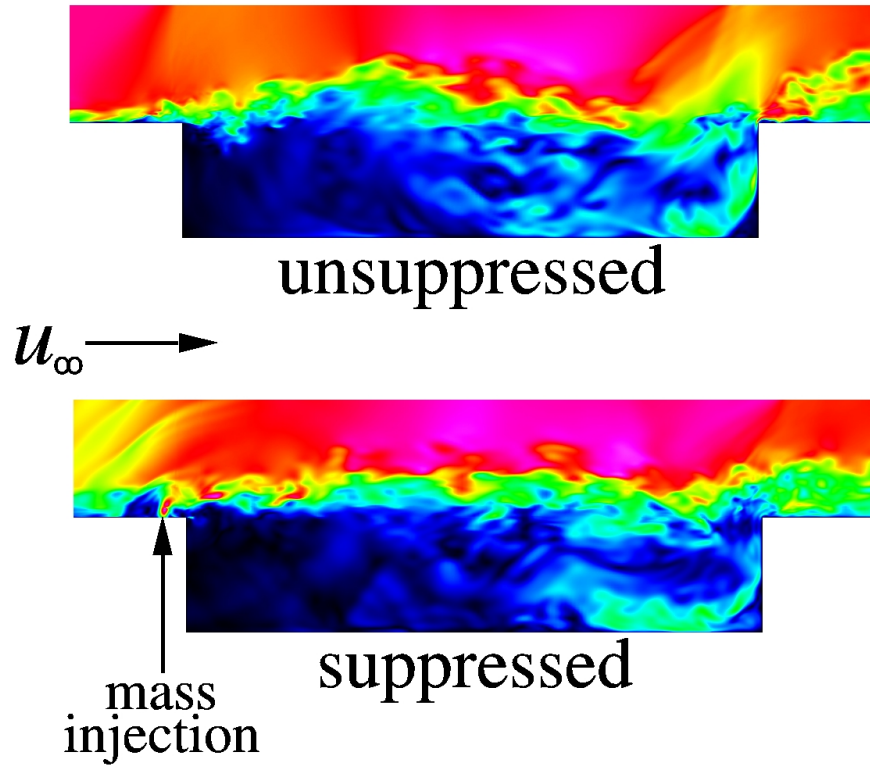


Figure 17: Instantaneous Mach number contours at the midspan location.

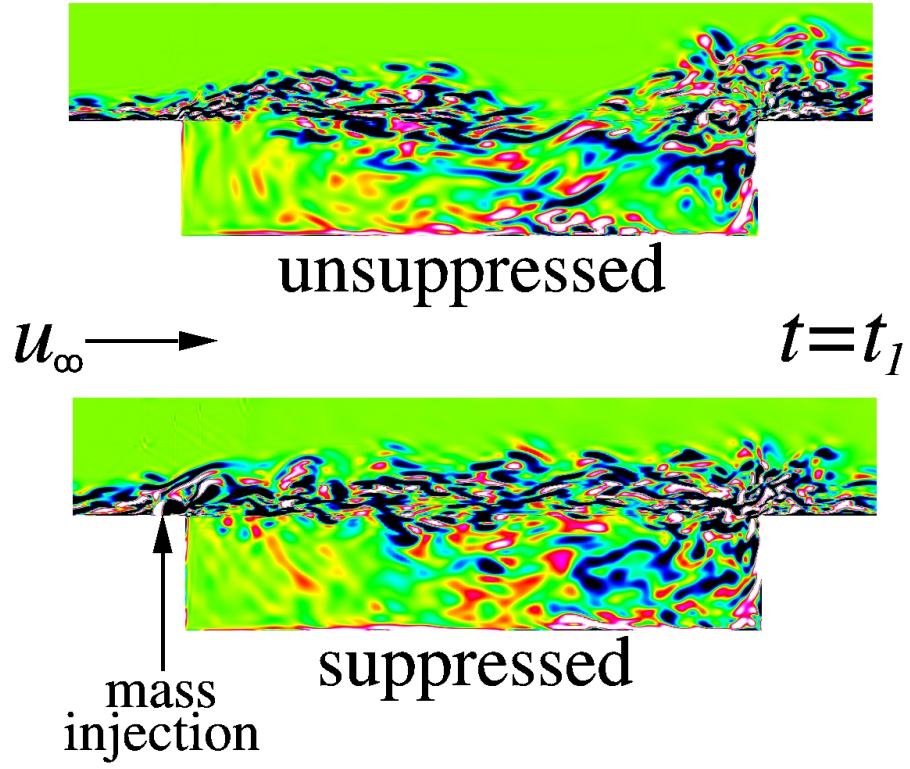


Figure 18: Instantaneous spanwise vorticity contours at the midspan location for $t = t_1$.

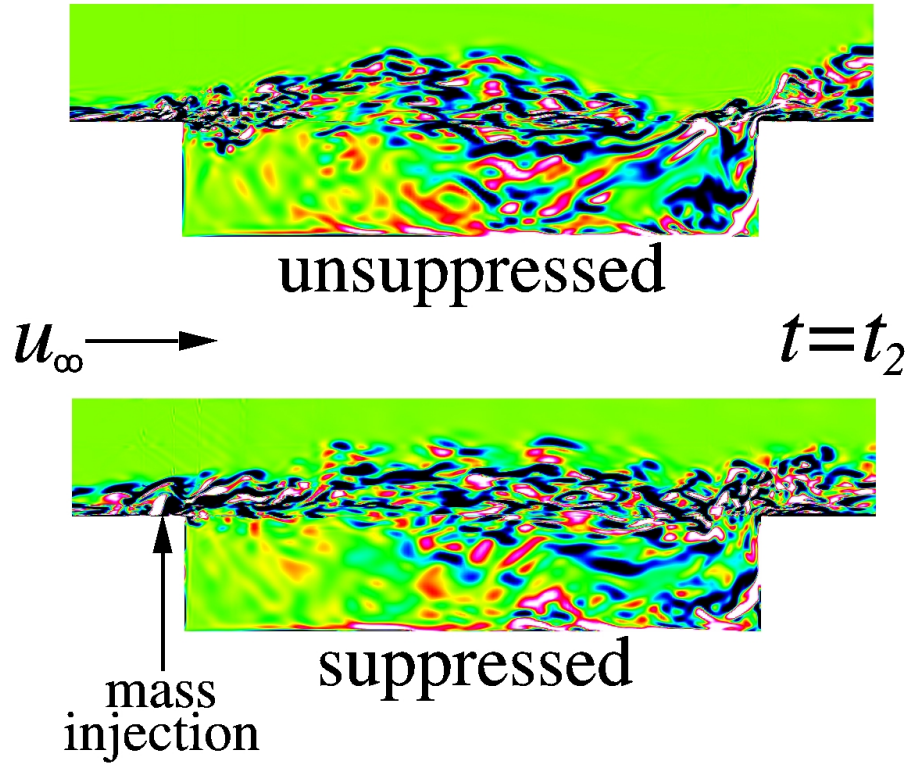


Figure 19: Instantaneous spanwise vorticity contours at the midspan location for $t = t_2$.

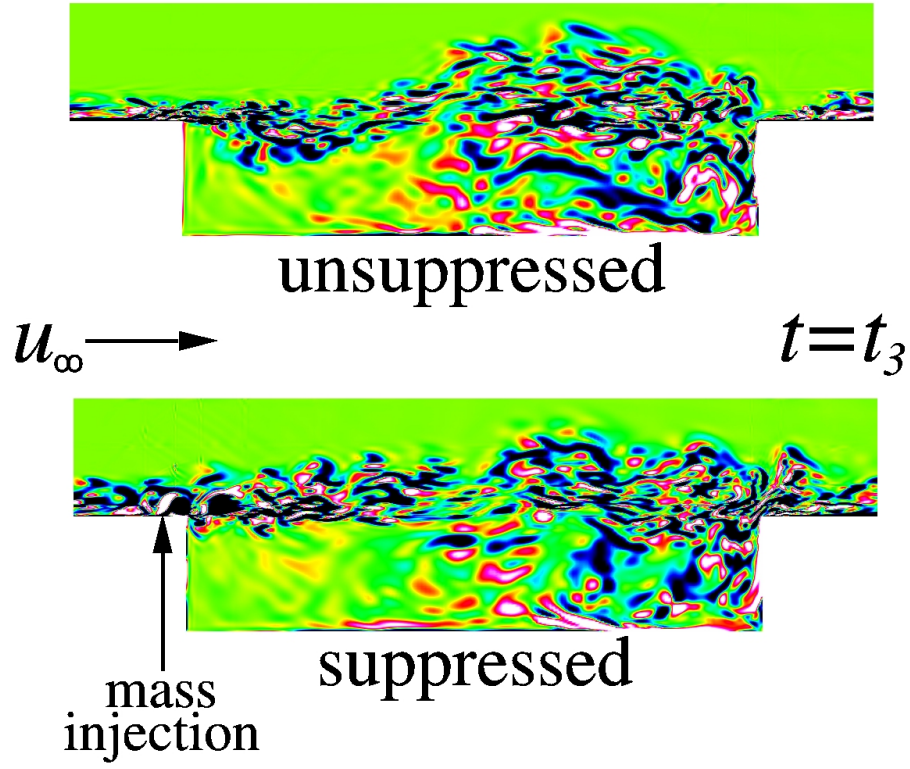


Figure 20: Instantaneous spanwise vorticity contours at the midspan location for $t = t_3$.

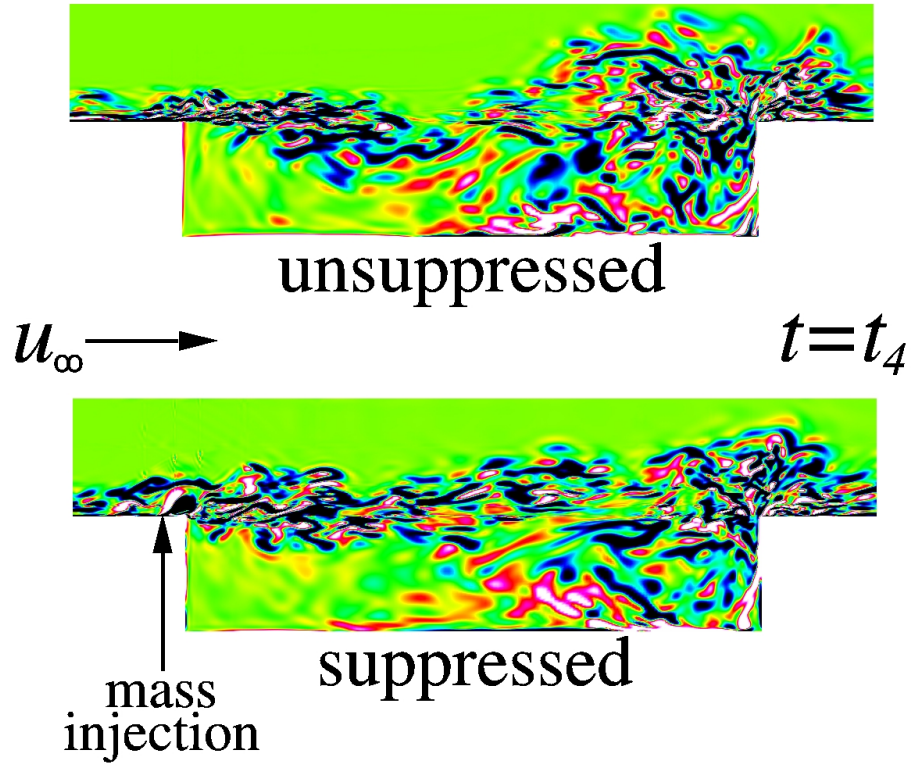


Figure 21: Instantaneous spanwise vorticity contours at the midspan location for $t = t_4$.

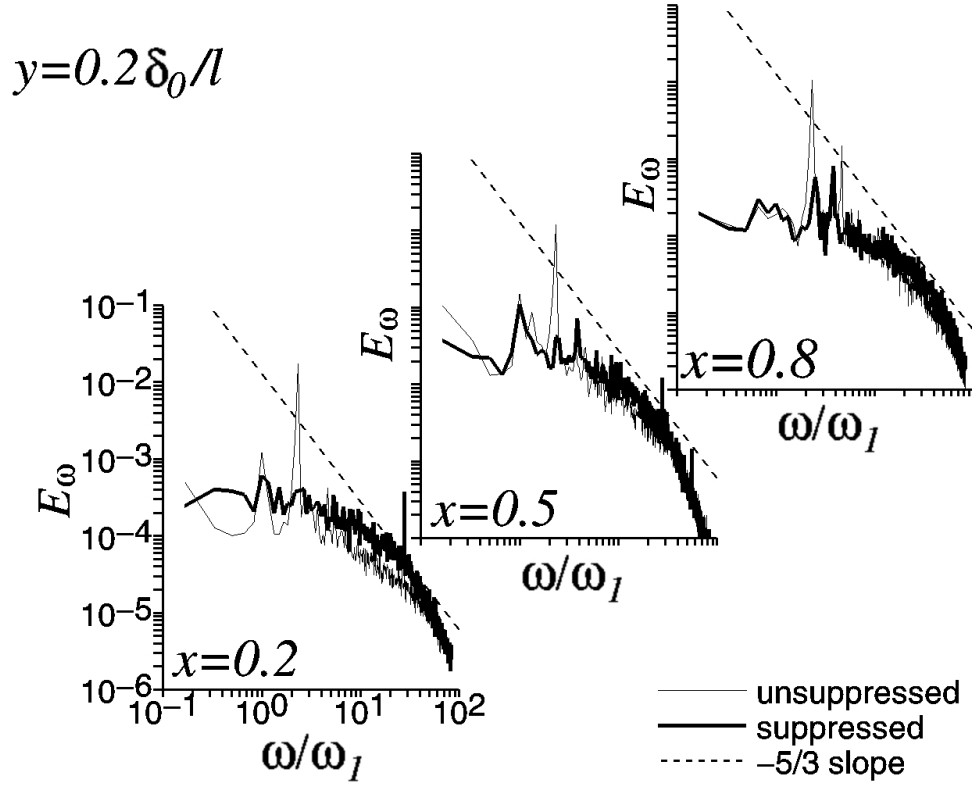


Figure 22: Spanwise-averaged turbulent kinetic energy frequency spectra at $x = 0.2, 0.5, 0.8$ and $y = 0.2\delta_0/l$.

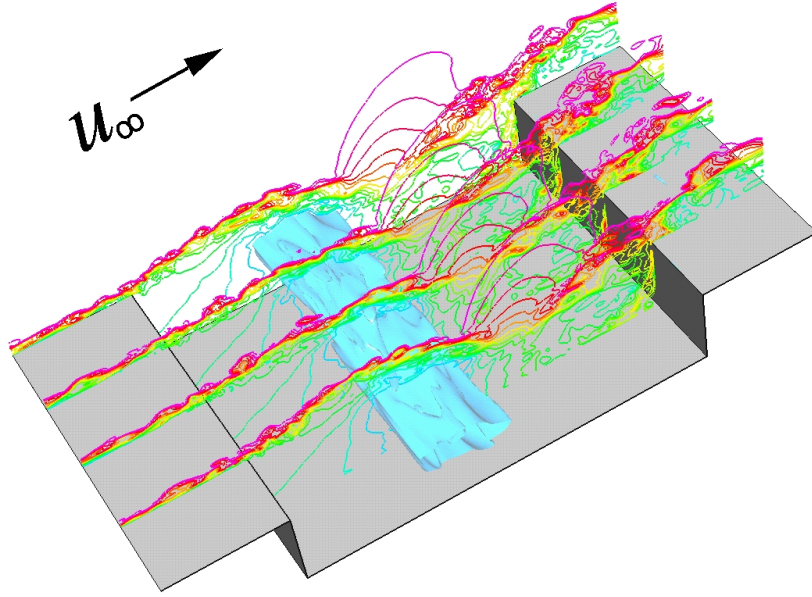


Figure 23: Instantaneous total pressure coefficient contours and iso-surface.

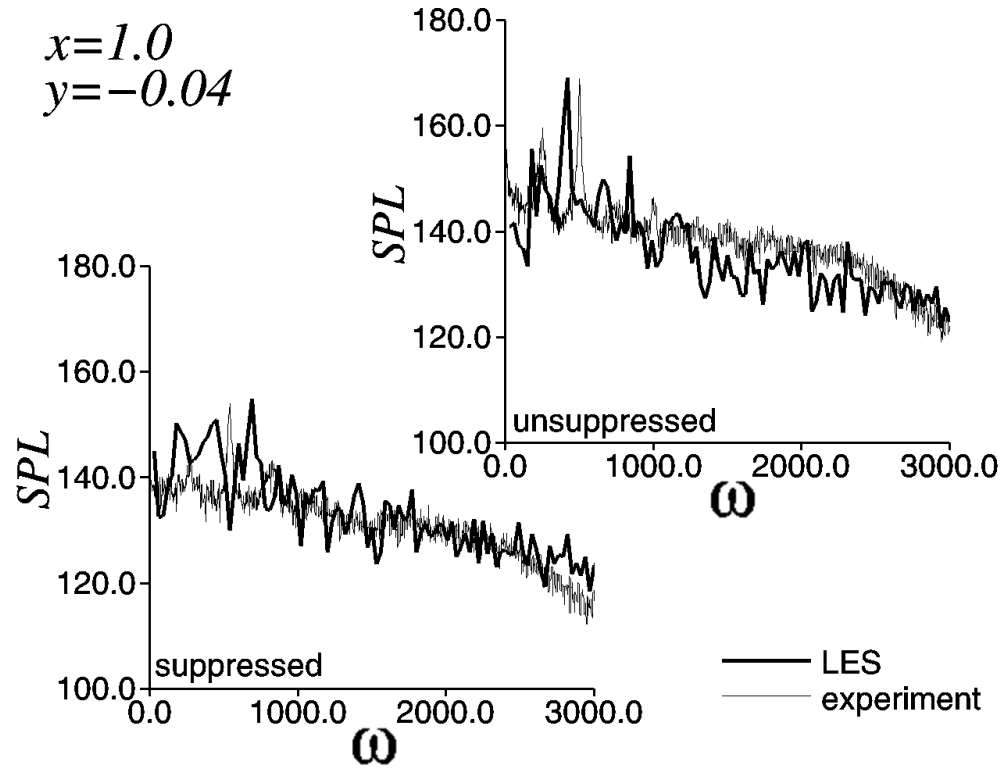


Figure 24: Spanwise-averaged fluctuating pressure frequency spectra on the cavity rear bulkhead at $y = -0.04$.

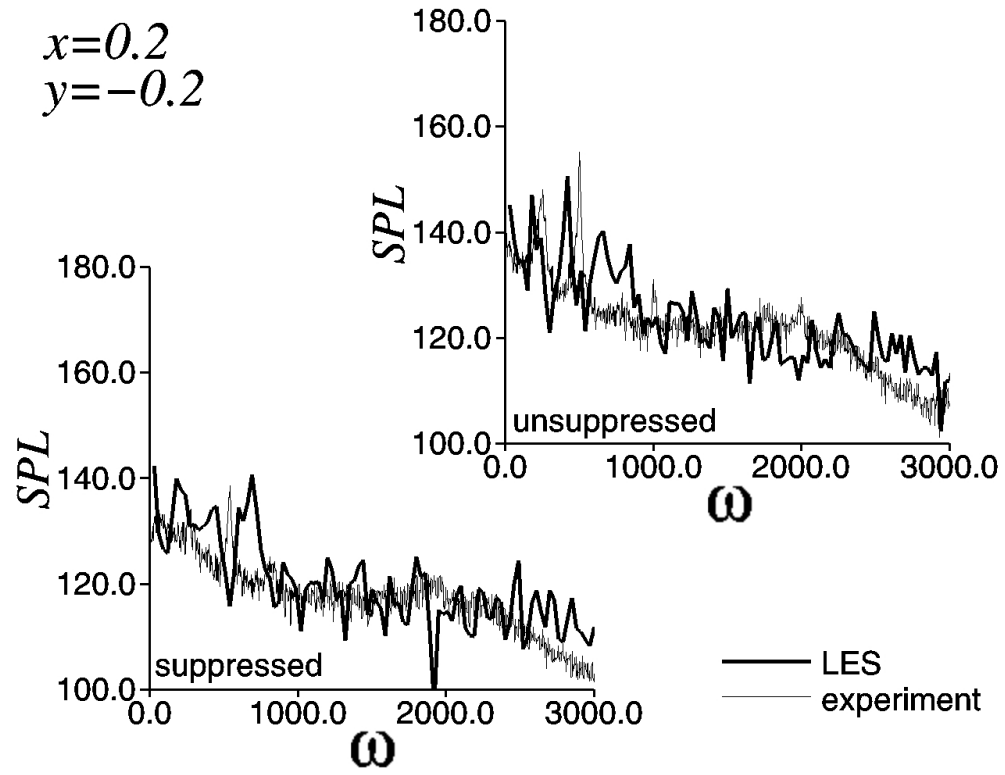


Figure 25: Spanwise-averaged fluctuating pressure frequency spectra on the cavity floor at $x = 0.2$.

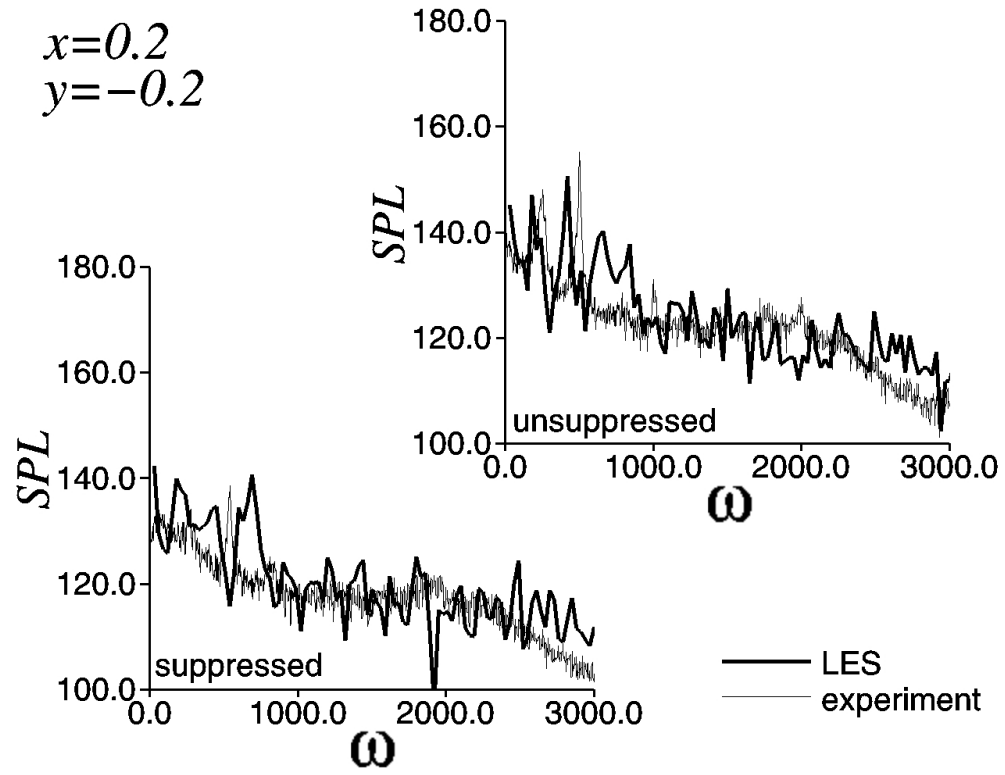


Figure 26: Spanwise-averaged fluctuating pressure frequency spectra on the cavity floor at $x = 0.5$.

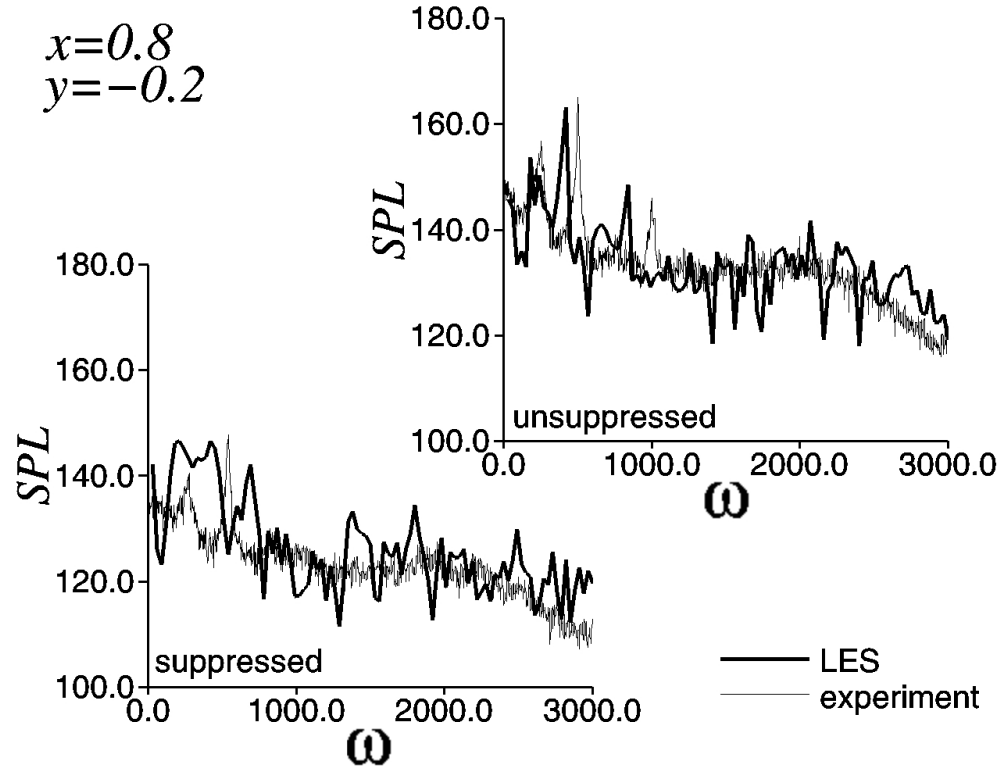


Figure 27: Spanwise-averaged fluctuating pressure frequency spectra on the cavity floor at $x = 0.8$.

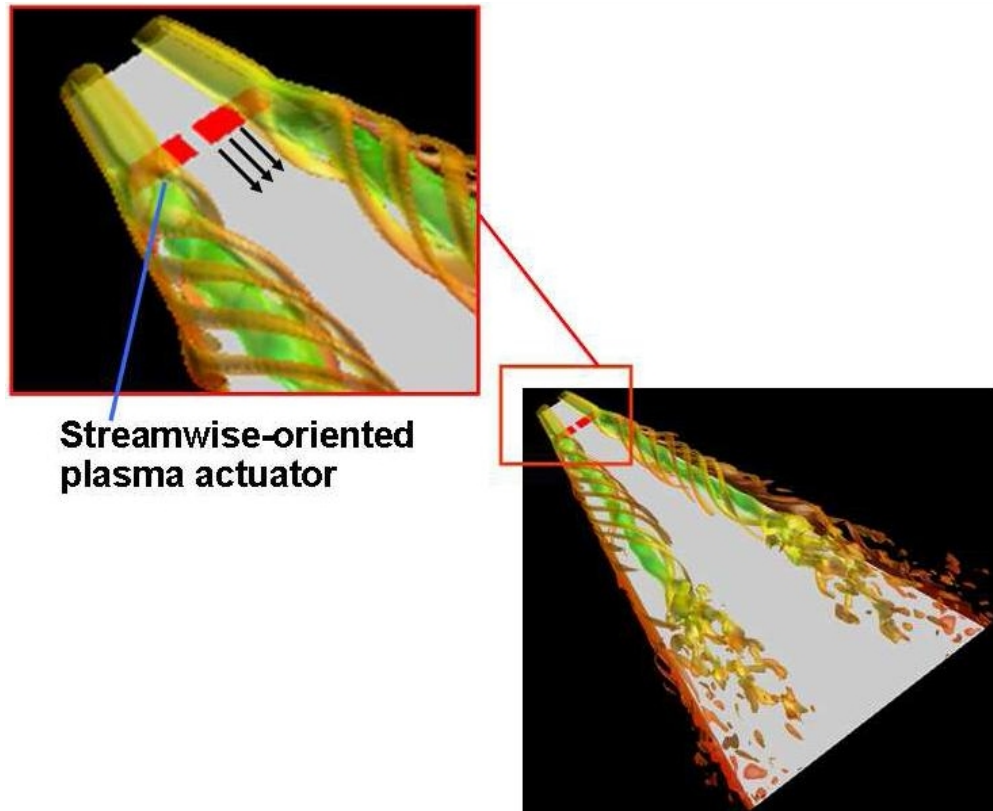


Figure 28: Schematic representation of delta wing actuator locations and flow features.

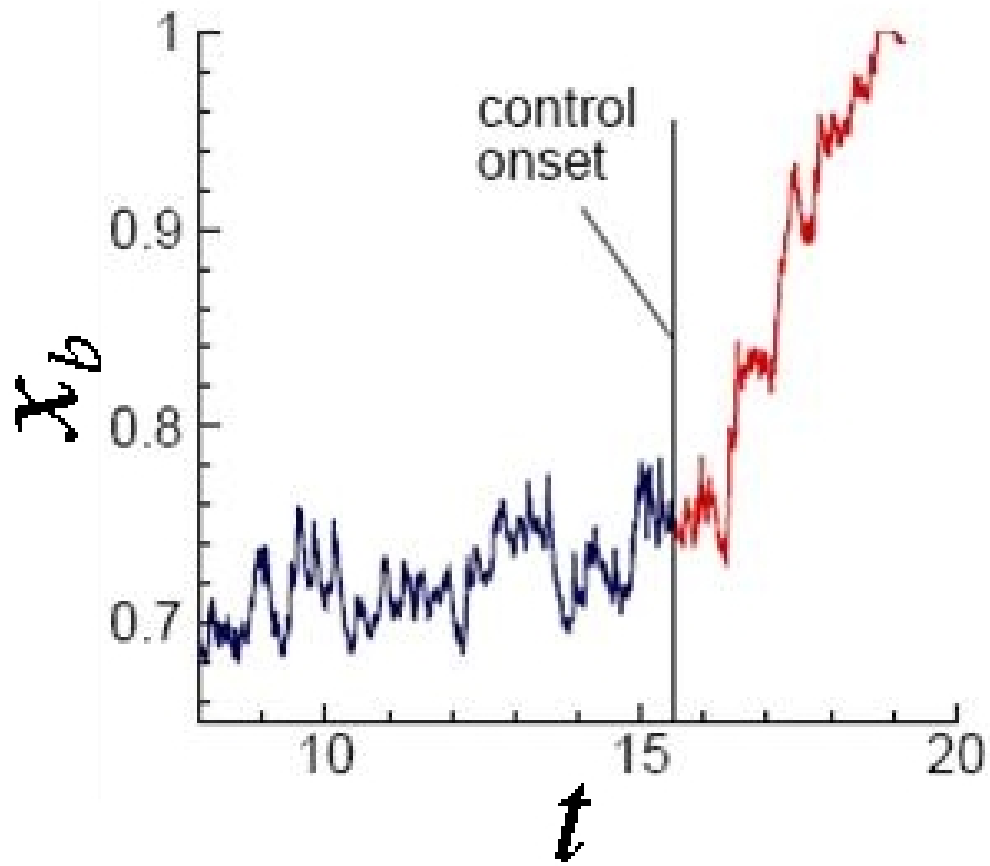


Figure 29: Time history of vortex breakdown location for $Re=25,000$ and $AOA=34$ deg.

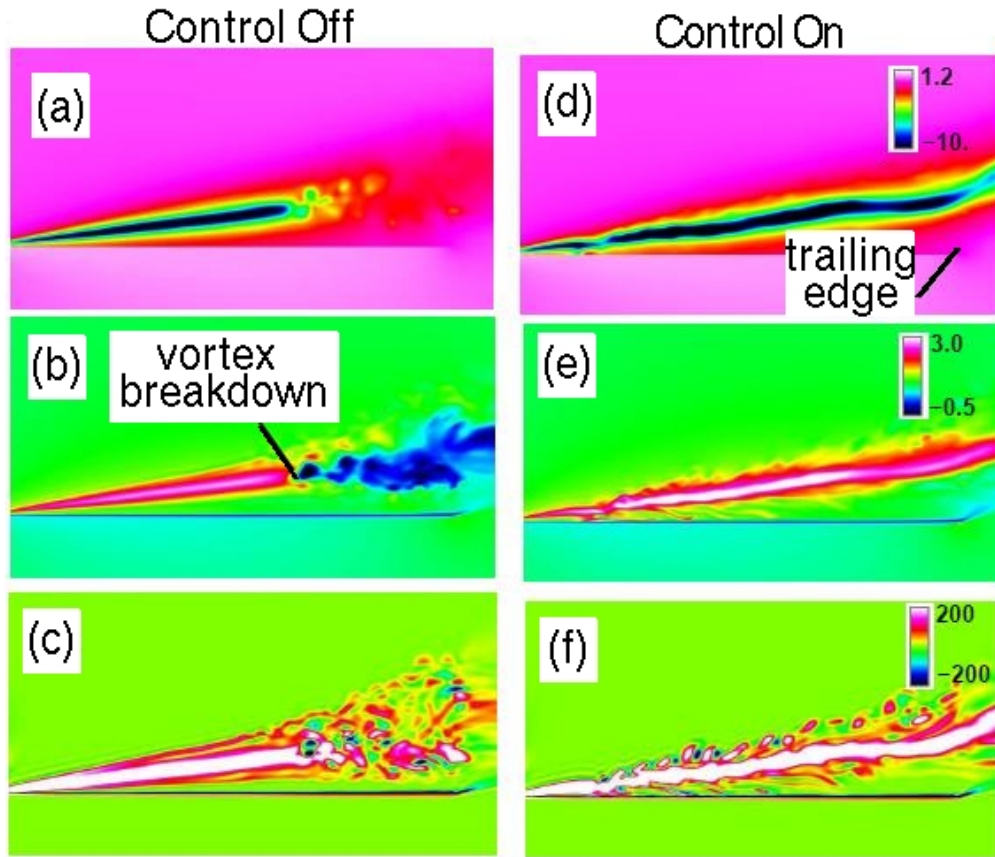


Figure 30: Instantaneous planar contours through the vortex core for $Re=25,000$ and $AOA=34^\circ$: (a) and (d) pressure coefficient, (b) and (e) streamwise velocity, (c) and (f) streamwise vorticity.

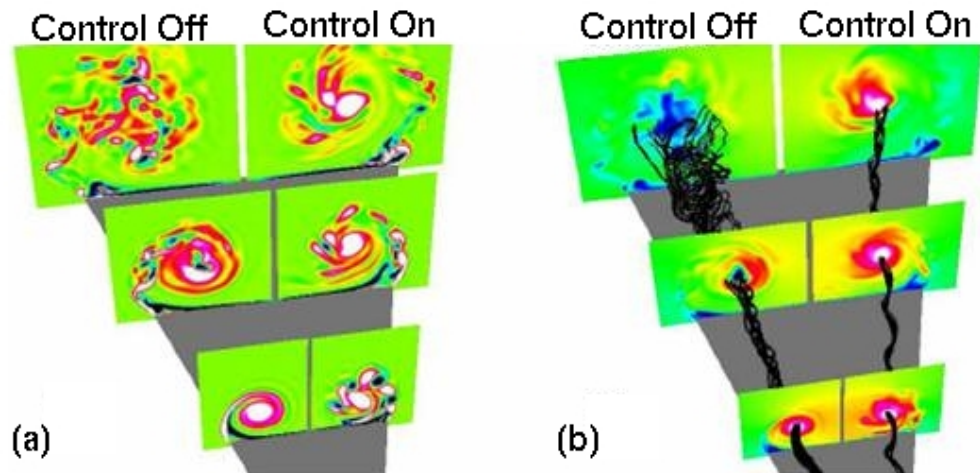


Figure 31: Instantaneous planar contours for $Re=25,000$ and $AOA=34$ deg: (a) streamwise vorticity, (b) streamwise velocity.

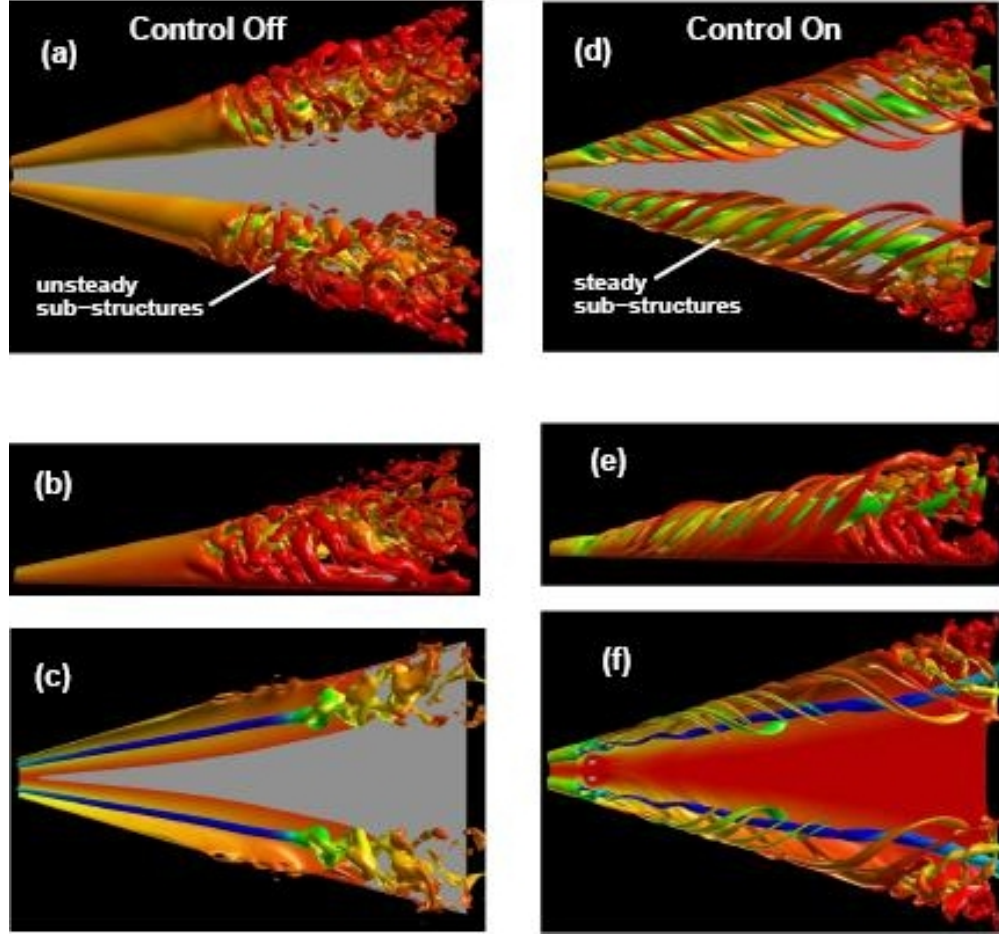


Figure 32: Instantaneous iso-surfaces for $Re=25,000$ and $AOA=34$ deg: (a), (b), (d), and (e) streamwise vorticity, (c) and (f) total pressure.

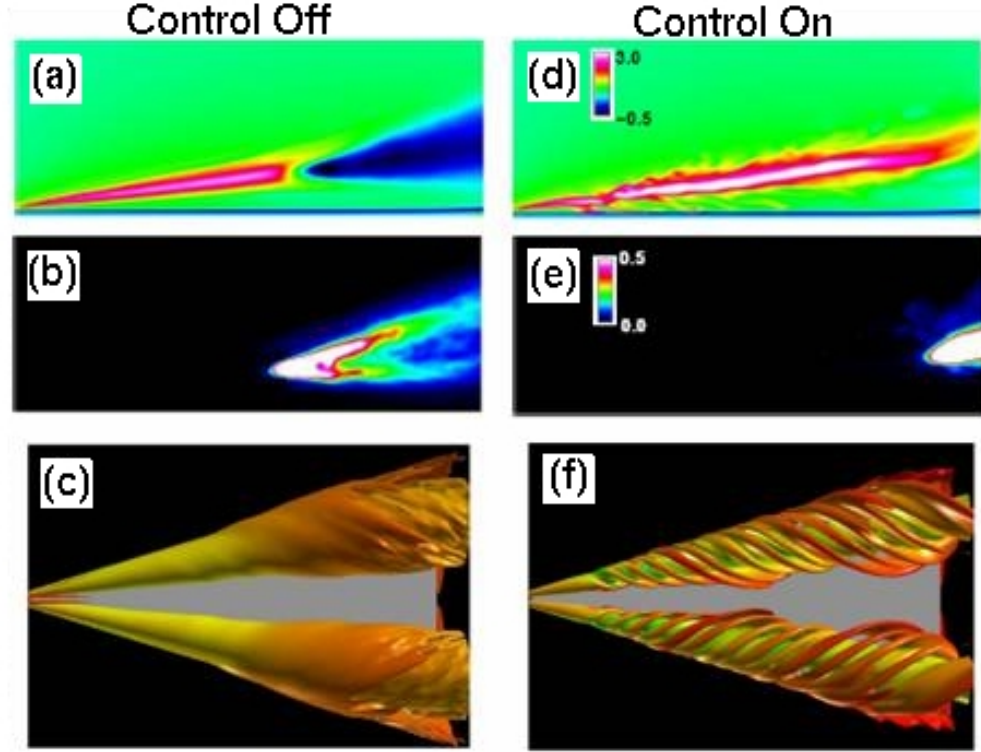


Figure 33: Time-mean flow quantities for $Re=25,000$ and $AOA=34$ deg: (a) and (d) planar contours of streamwise velocity through the vortex core, (b) and (e) planar contours of rms streamwise velocity fluctuations through the vortex core, (c) and (f) iso-surface of streamwise vorticity.

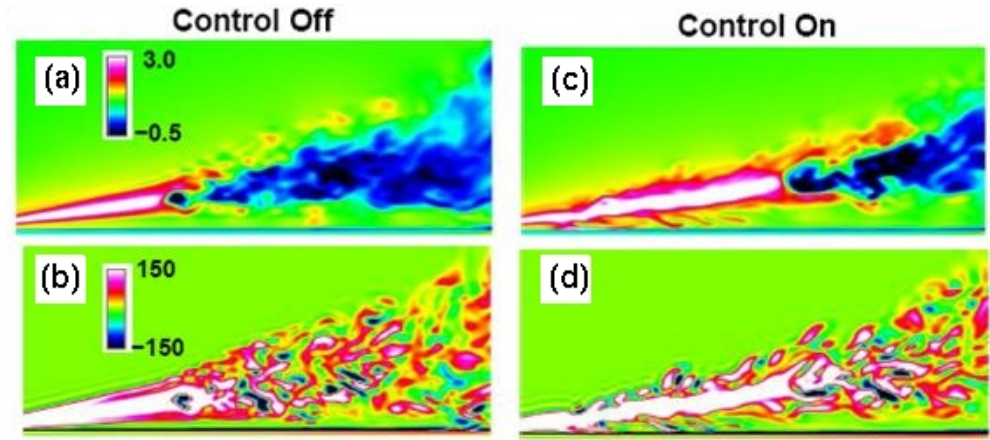


Figure 34: Instantaneous planar contours through the vortex core for $Re=25,000$ and $AOA=38$ deg: (a) and (c) streamwise velocity, (b) and (d) streamwise vorticity.

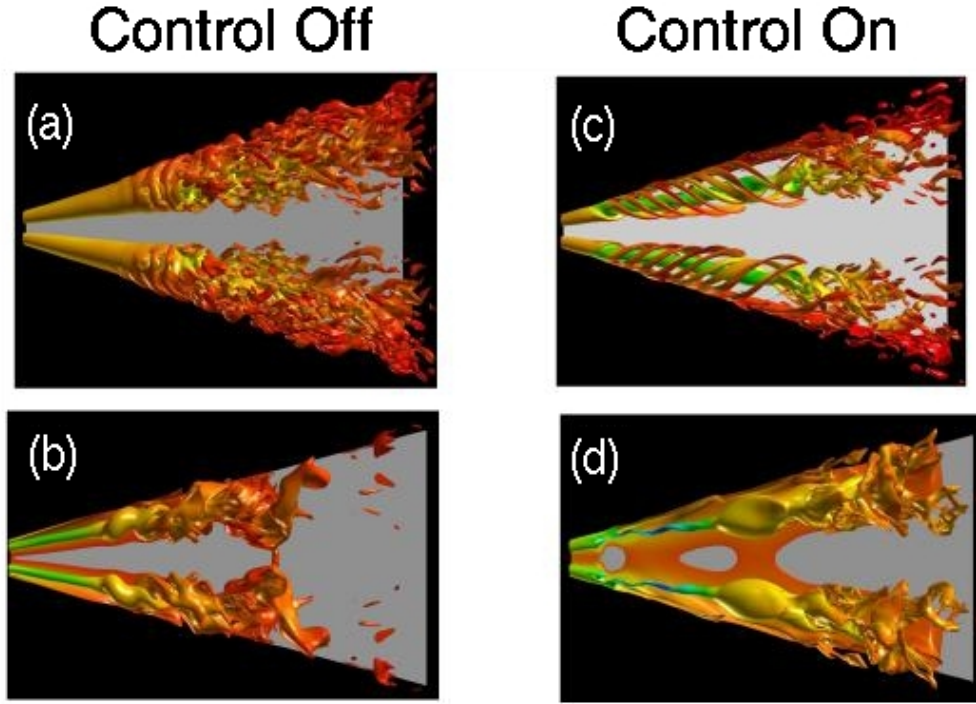


Figure 35: Instantaneous iso-surfaces at AOA=38 deg: (a) and (c) streamwise vorticity for $Re=25,000$, (b) and (d) total pressure for $Re=9,200$.

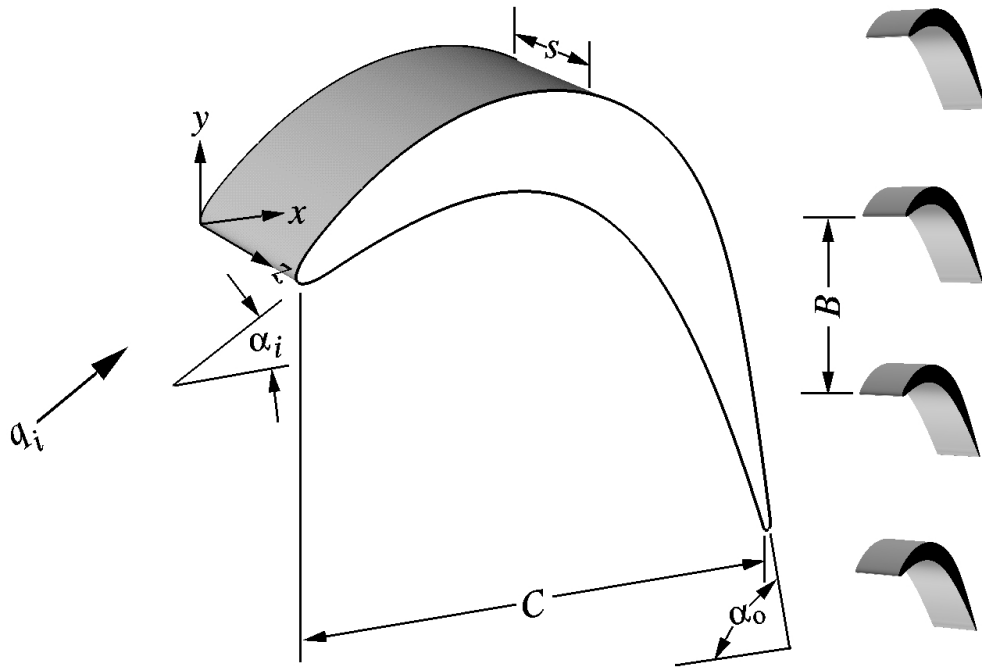


Figure 36: Schematic representation of the turbine blade configuration.

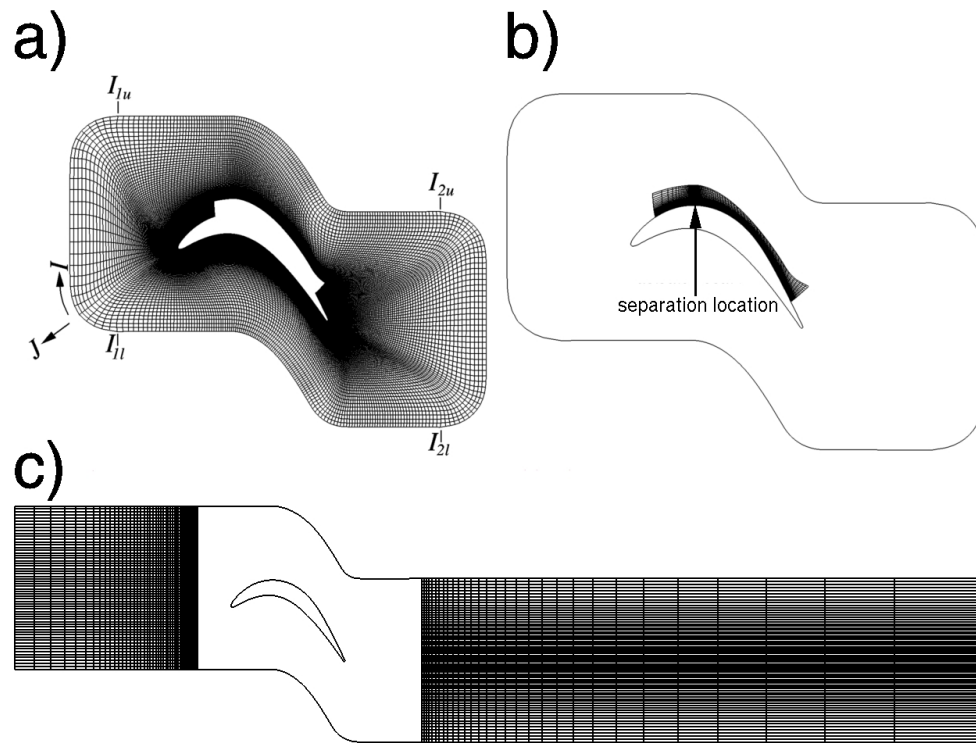


Figure 37: Turbine blade computational mesh system.

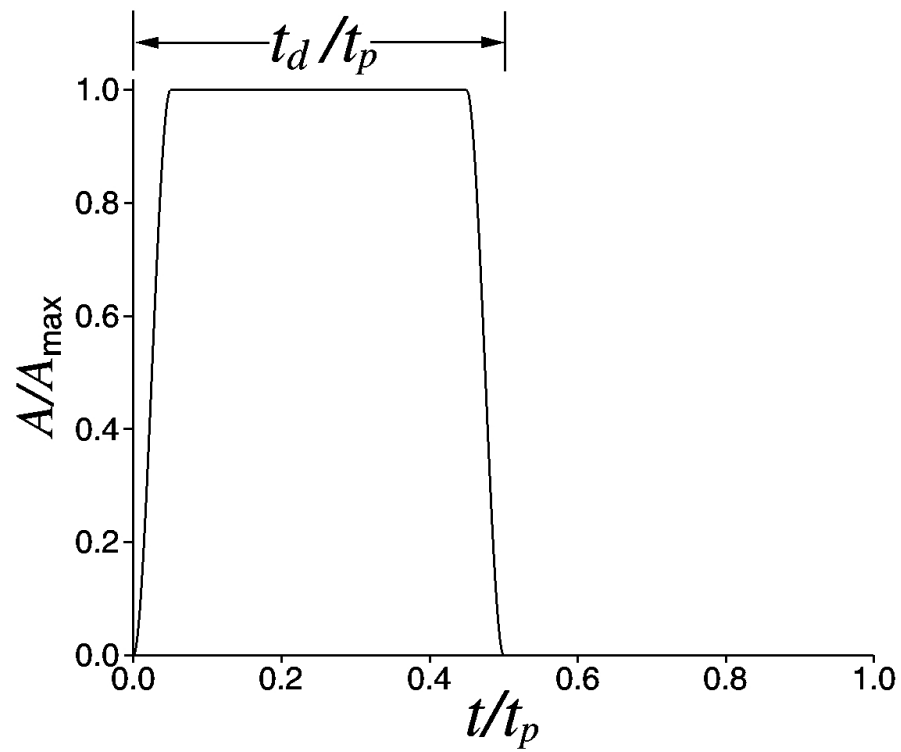


Figure 38: Duty cycle amplitude time history.

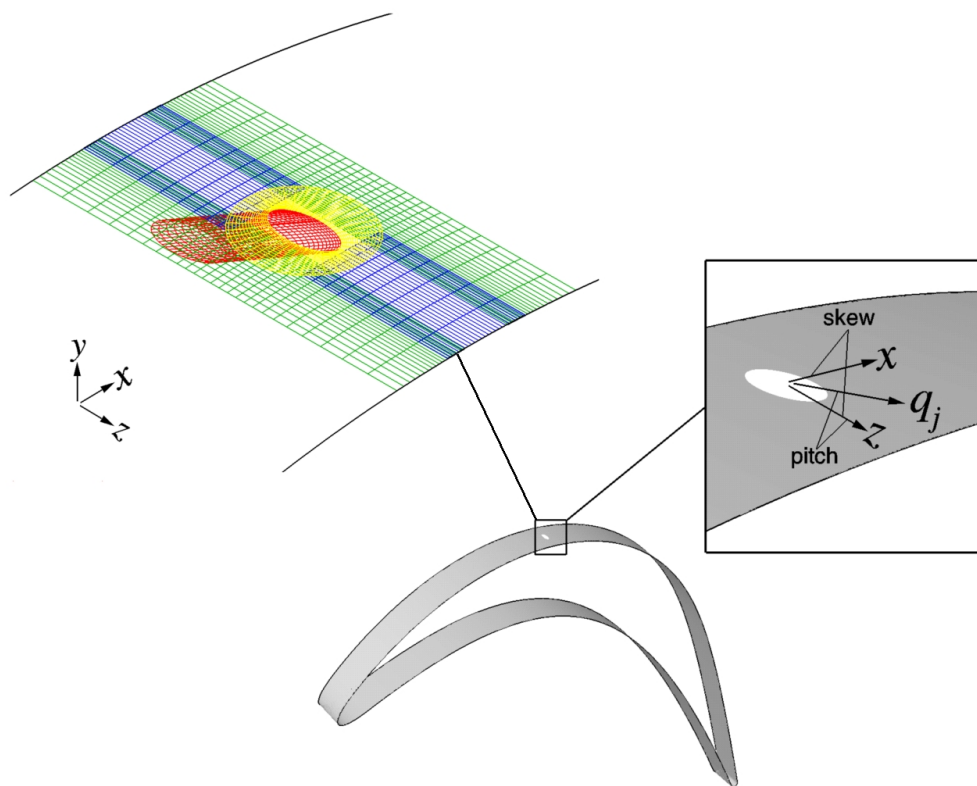


Figure 39: Vortex generator jet geometry and mesh system.

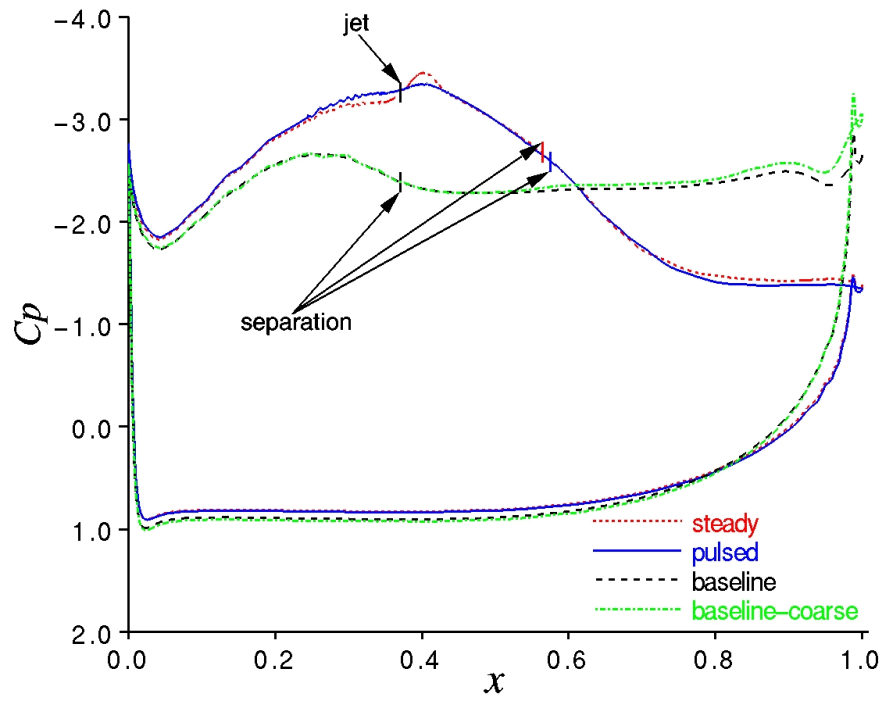


Figure 40: Time-mean surface pressure coefficient distributions for vortex-jet control.

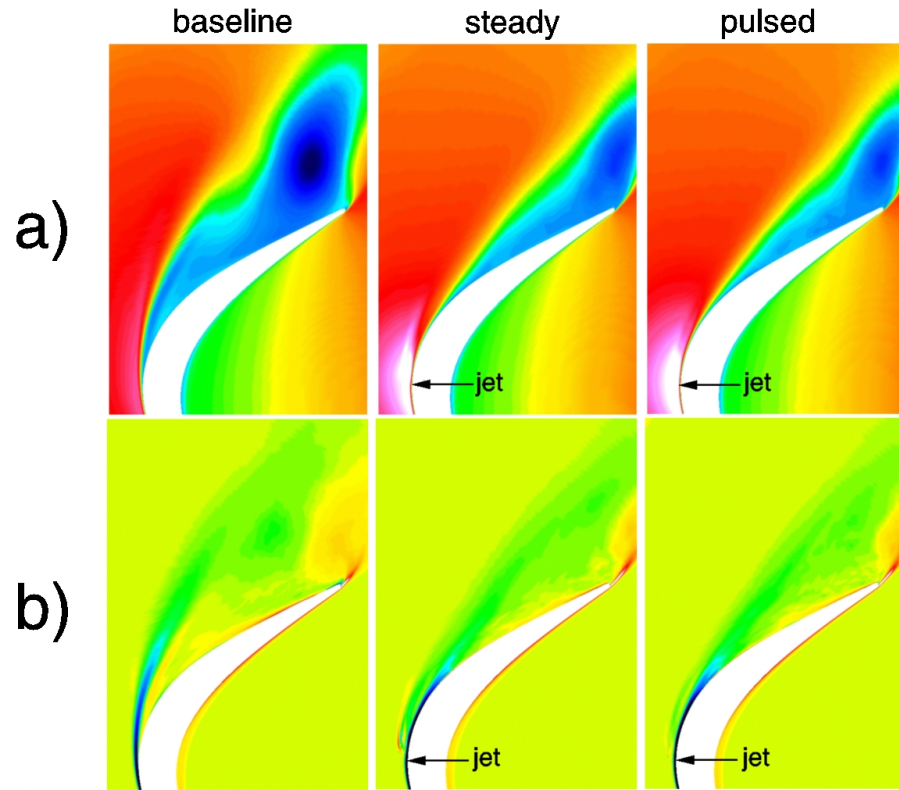


Figure 41: Time-mean planar contours for vortex-jet control: a) streamwise velocity, b) spanwise vorticity.

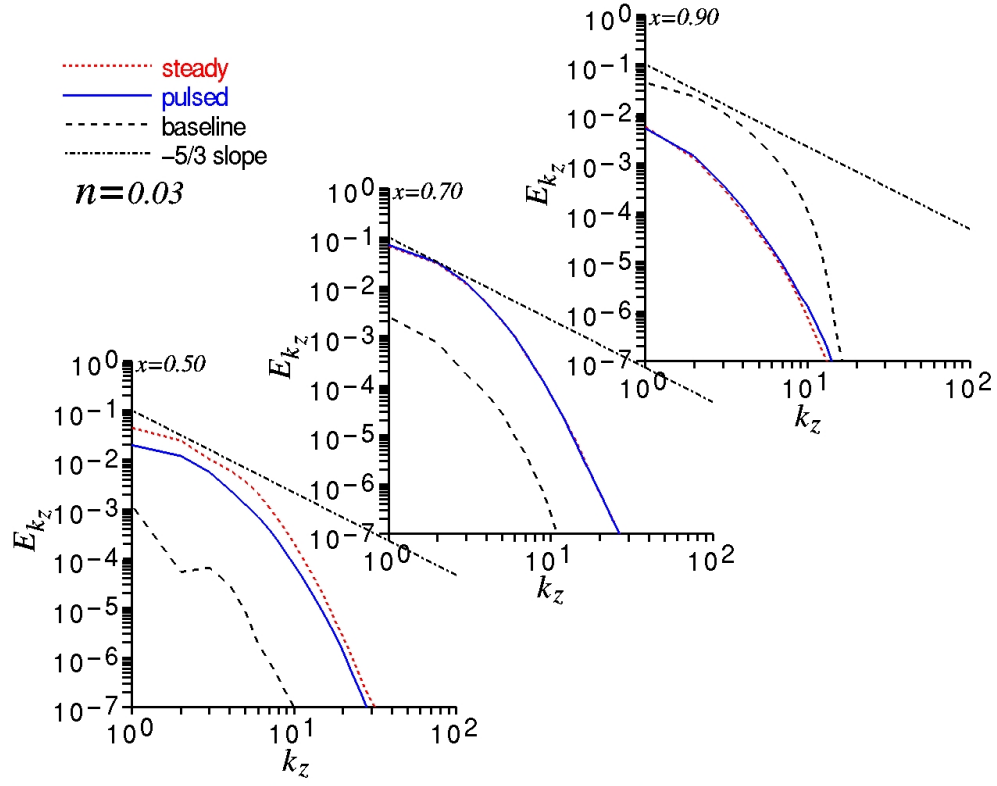


Figure 42: Time-mean turbulent kinetic energy spanwise wave-number spectra for vortex-jet control.

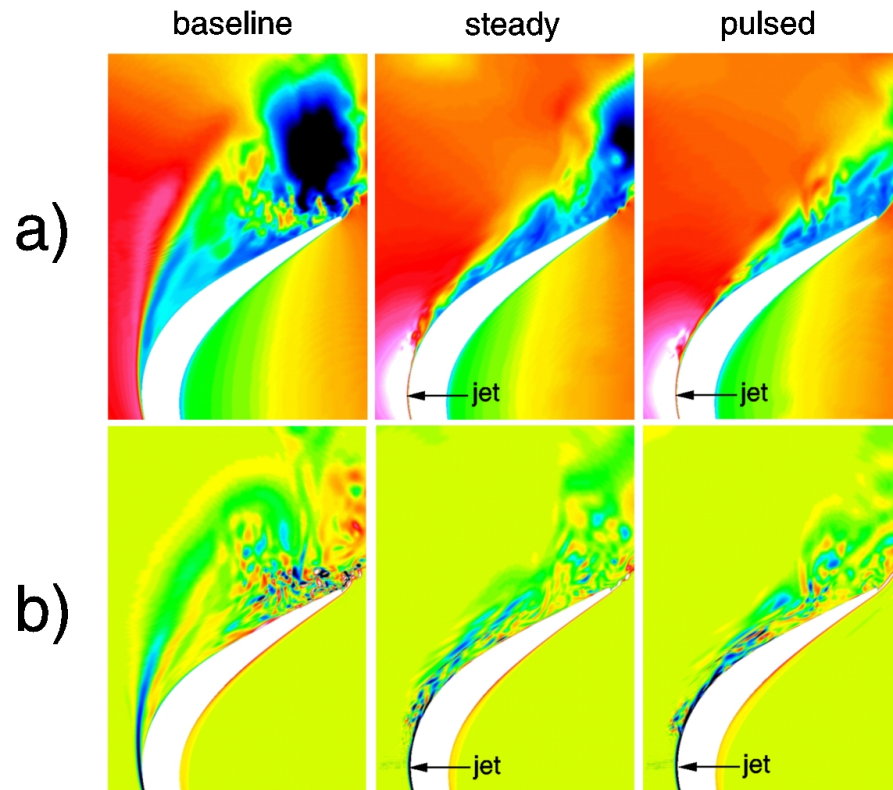


Figure 43: Instantaneous planar contours for vortex-jet control: a) streamwise velocity, b) spanwise vorticity.

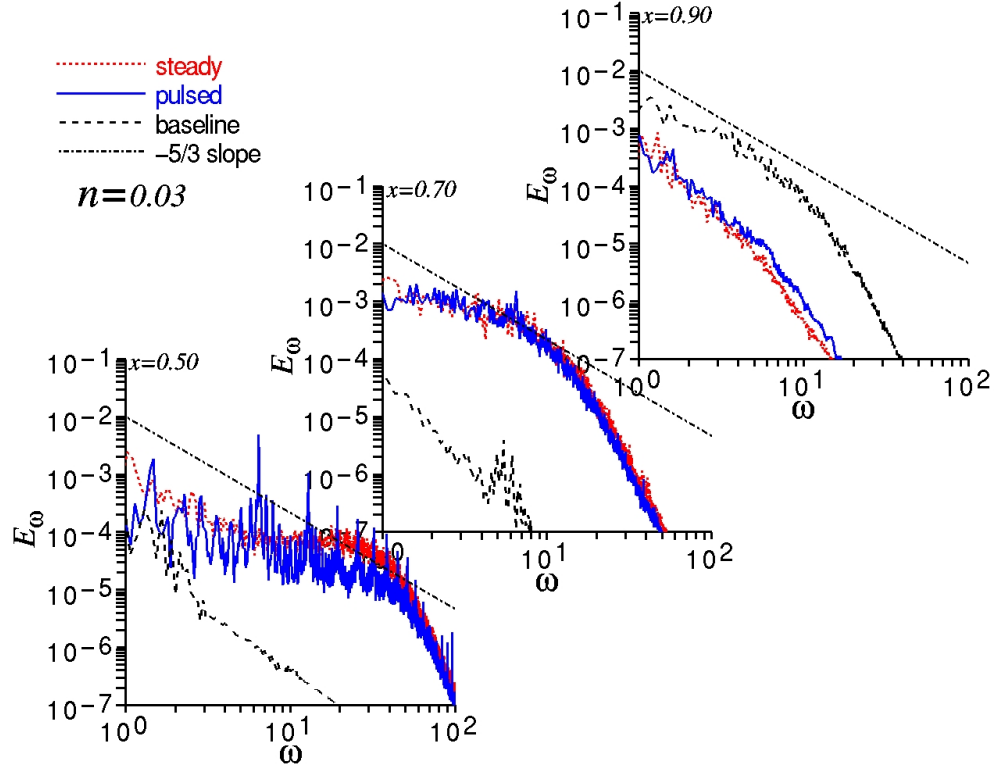


Figure 44: Turbulent kinetic energy frequency spectra for vortex-jet control.

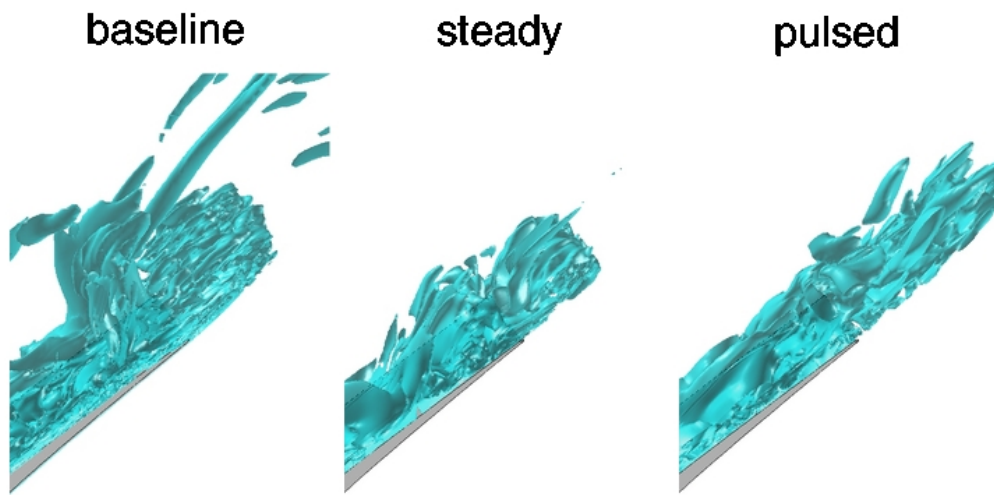


Figure 45: Instantaneous iso-surfaces of vorticity magnitude in the trailing-edge region for vortex-jet control.

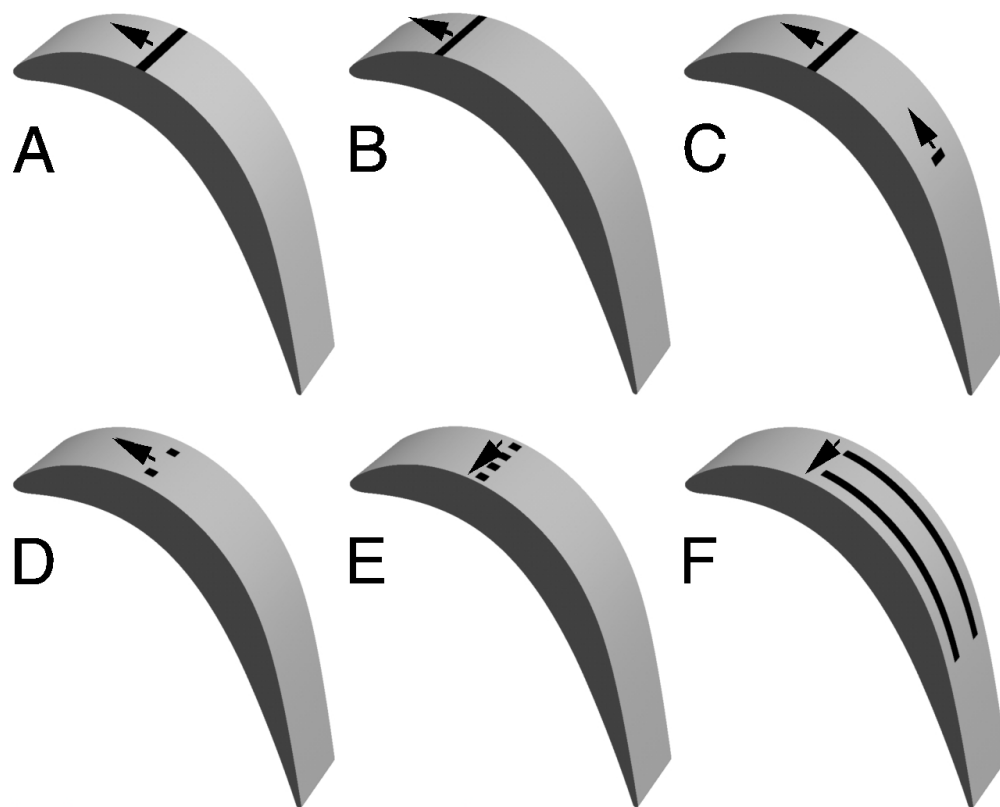


Figure 46: Plasma actuator configurations.

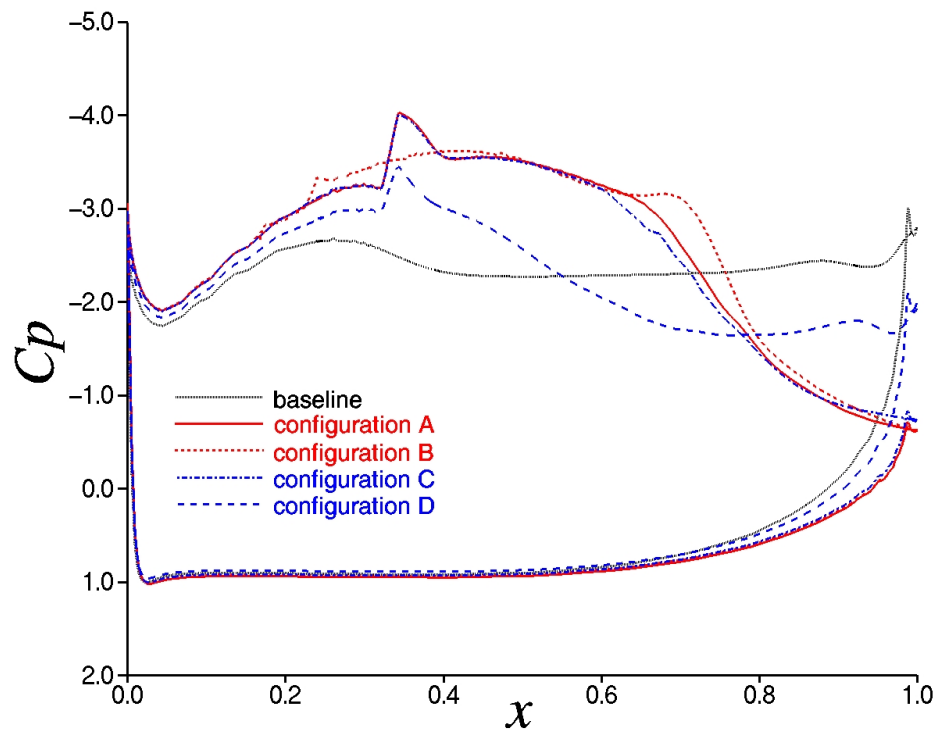


Figure 47: Time-mean surface pressure coefficient distributions for plasma control.

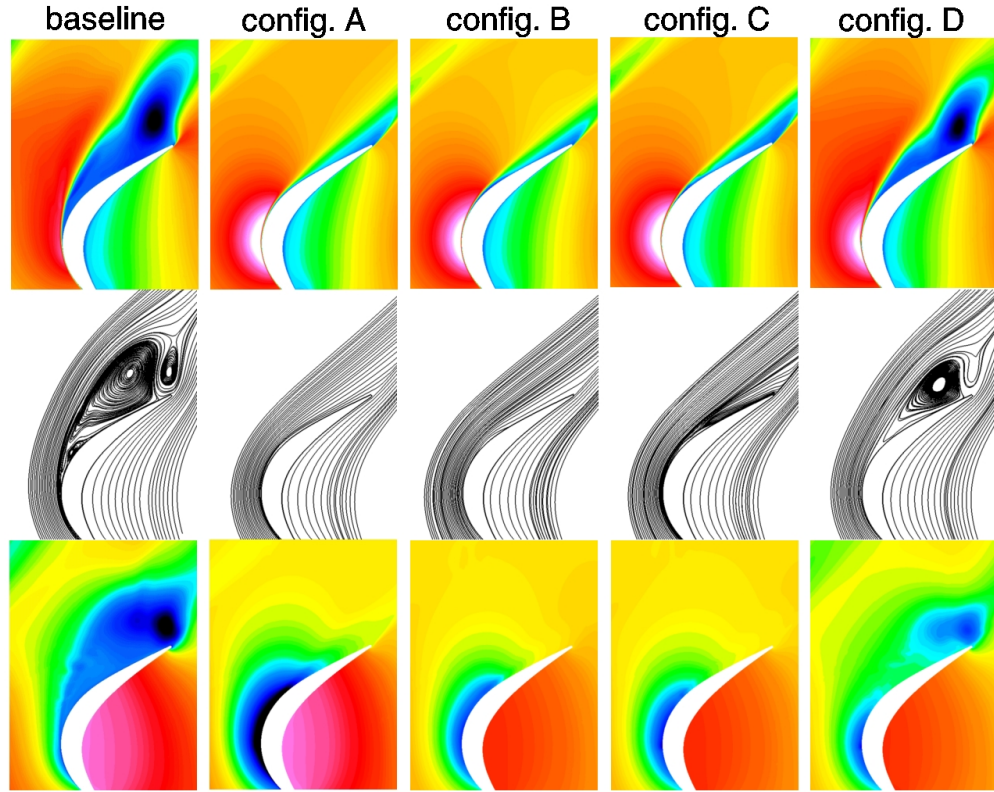


Figure 48: Time-mean results for plasma control: contours of streamwise velocity (top row), streamlines (middle row), contours of C_p (bottom row).

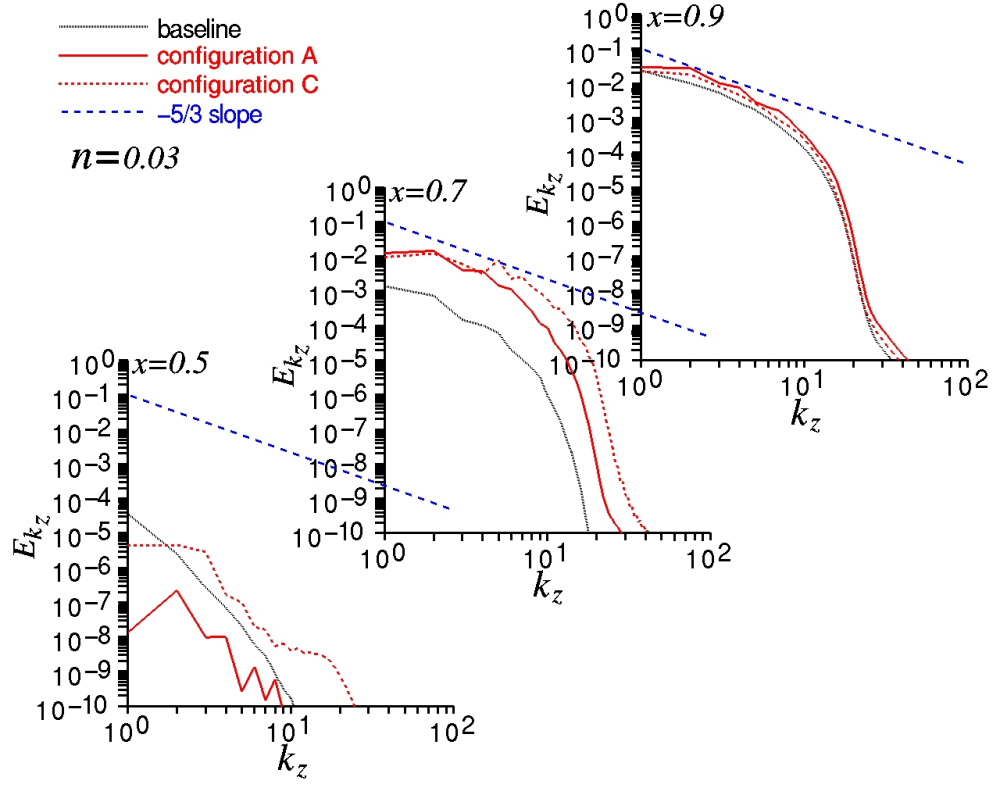


Figure 49: Time-mean turbulent kinetic energy spanwise wave-number spectra for plasma control.

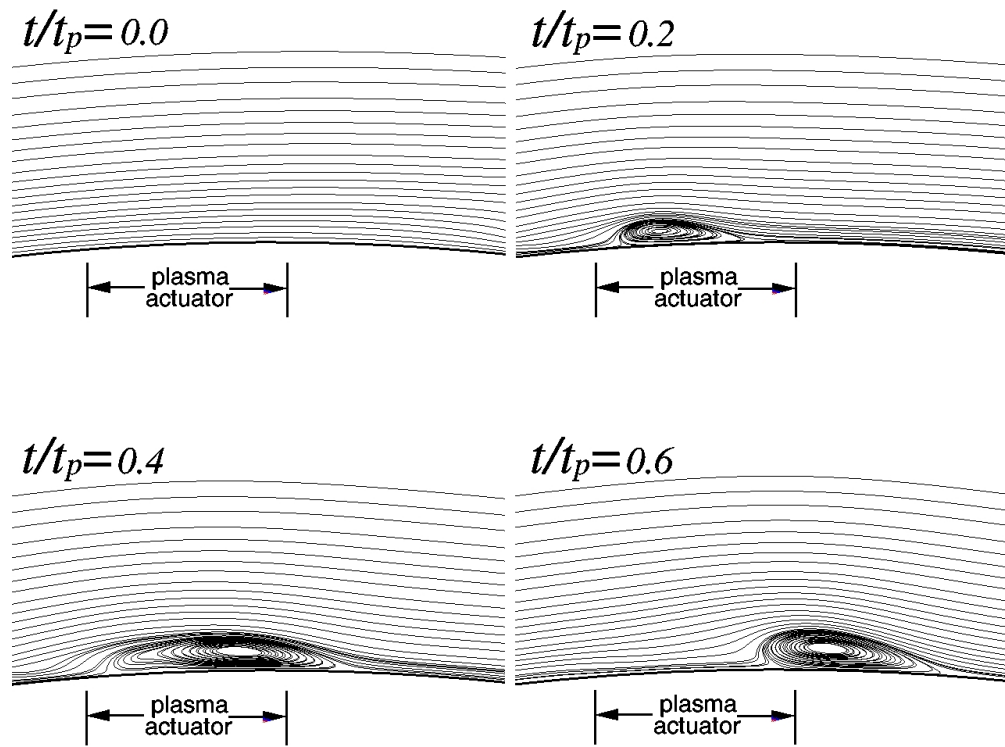


Figure 50: Instantaneous streamlines at the midspan for plasma control with configuration **A**.

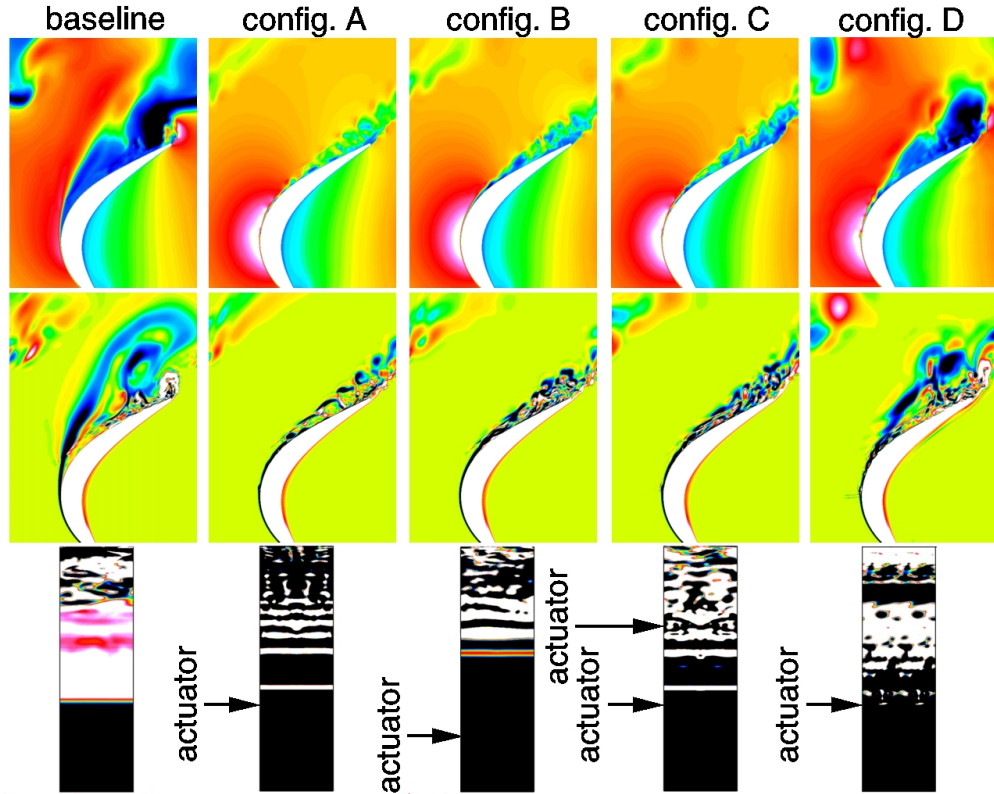


Figure 51: Instantaneous contours for plasma control: streamwise velocity (top row), spanwise vorticity (middle row), spanwise vorticity on the blade surface (bottom row).

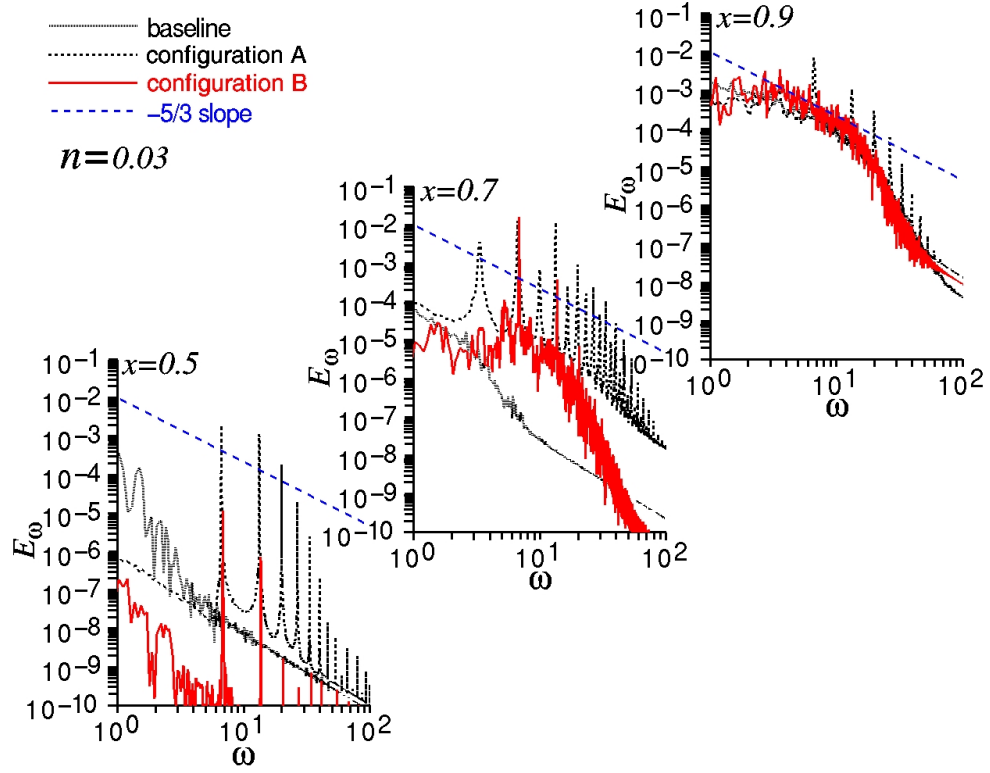


Figure 52: Turbulent kinetic energy frequency spectra for plasma control.

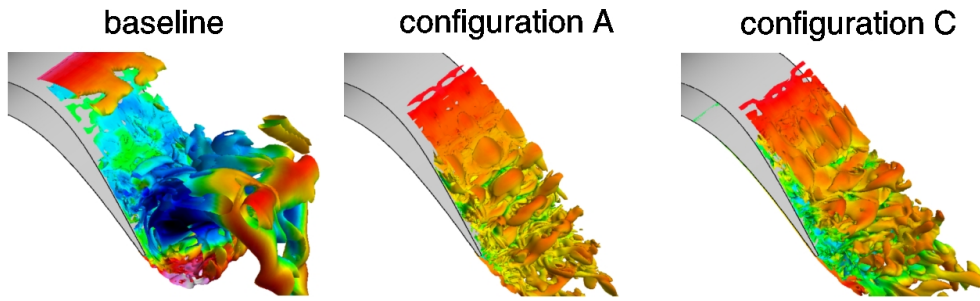


Figure 53: Instantaneous iso-surfaces of vorticity magnitude colored by streamwise velocity in the trailing-edge region for plasma control.

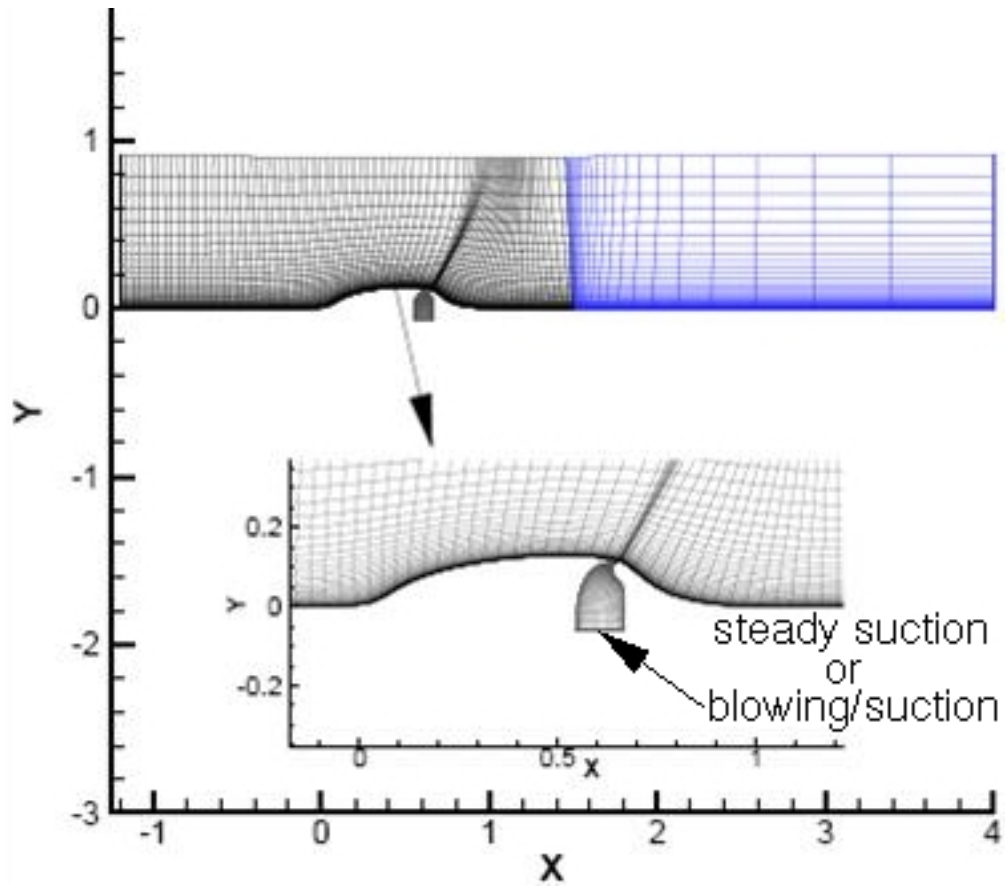


Figure 54: Computational mesh system for wall-mounted hump.

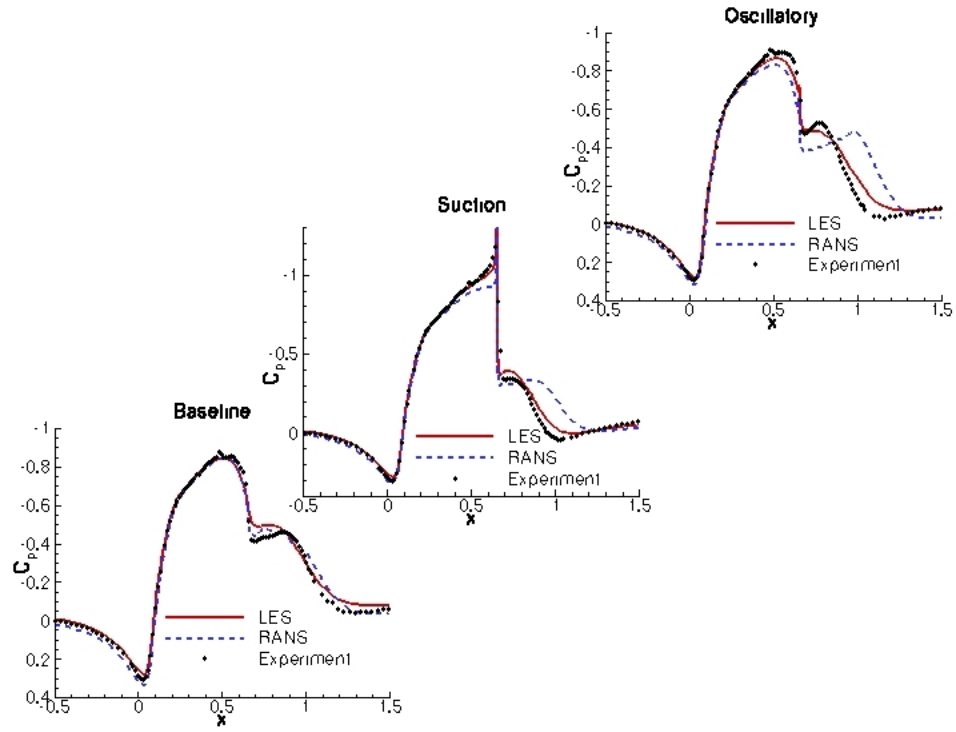


Figure 55: Time-mean surface pressure coefficient distributions.

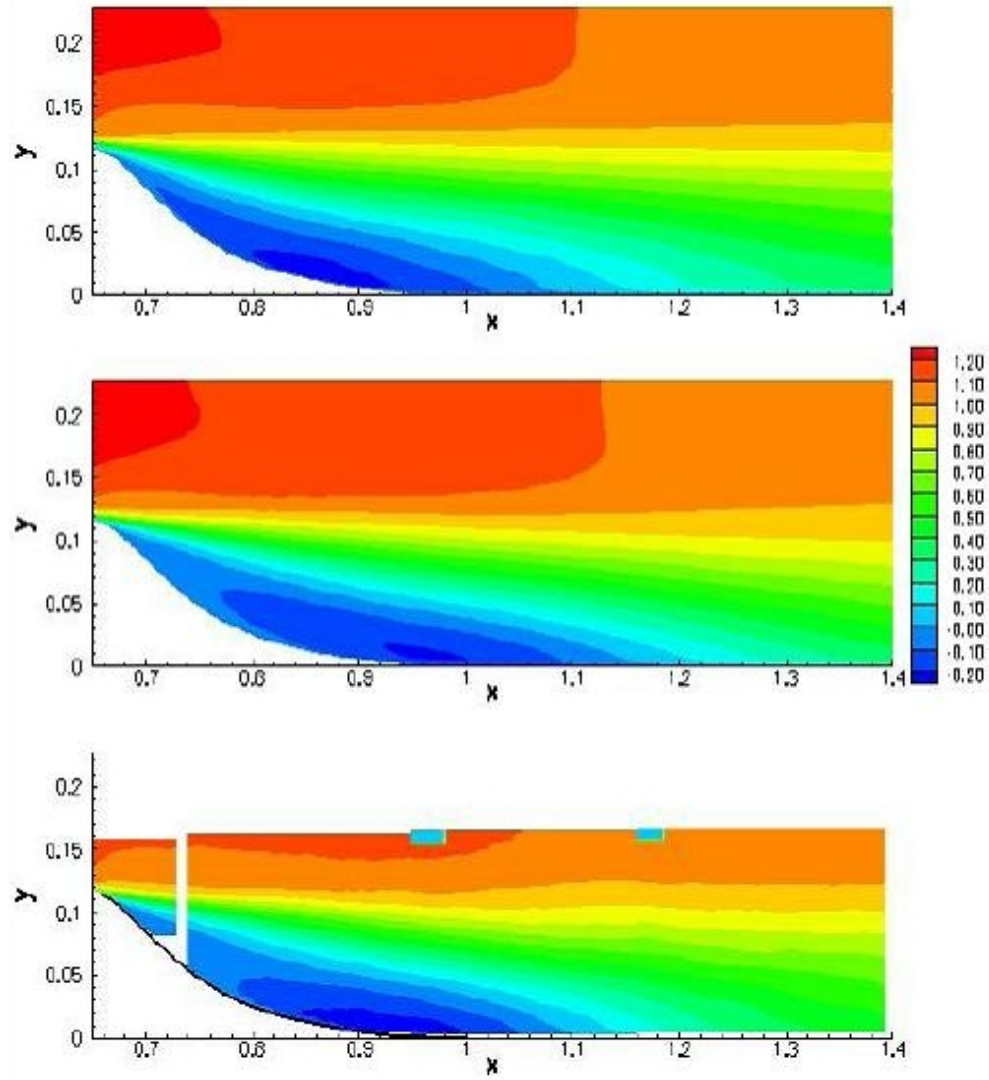


Figure 56: Time-mean streamwise velocity contours for the baseline case: LES (top), RANS (middle), experiment (bottom).

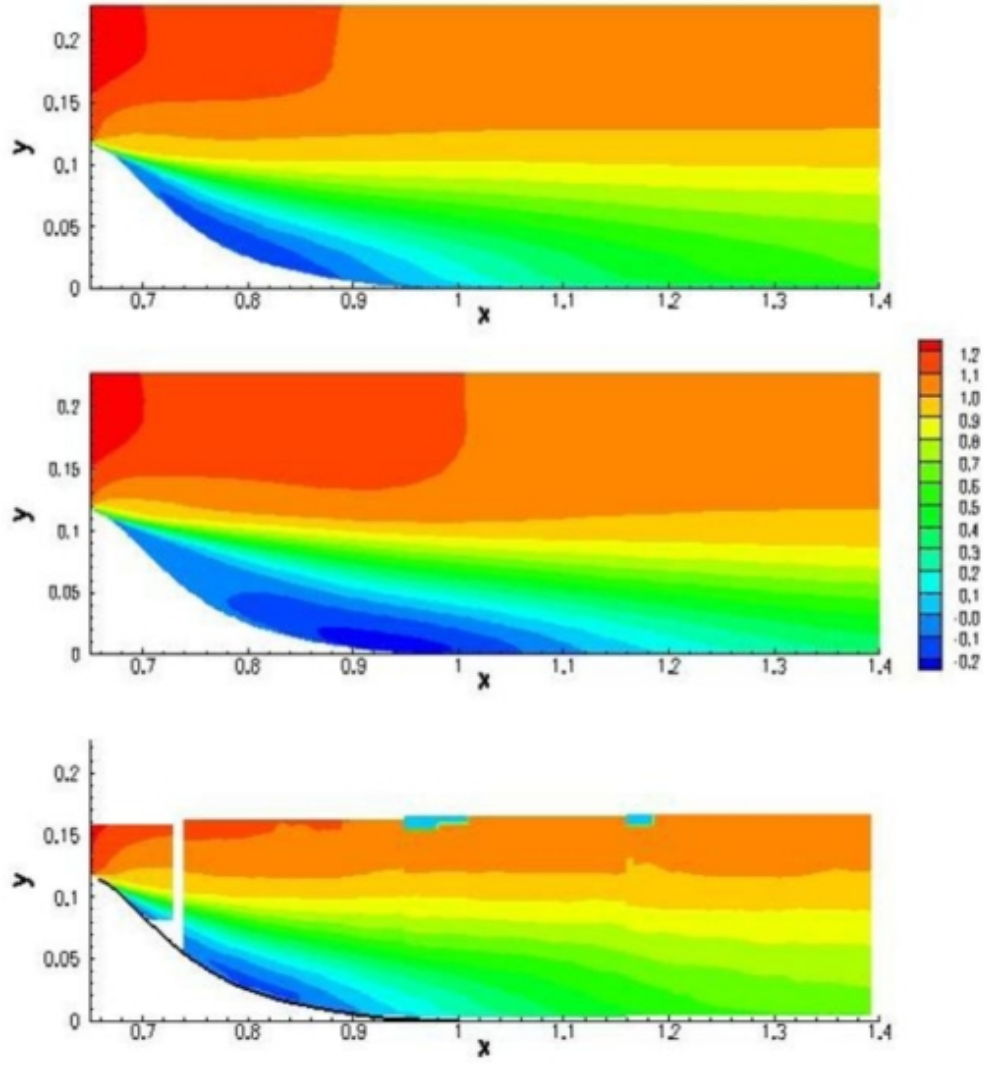


Figure 57: Time-mean streamwise velocity contours for the suction case: LES (top), RANS (middle), experiment (bottom).

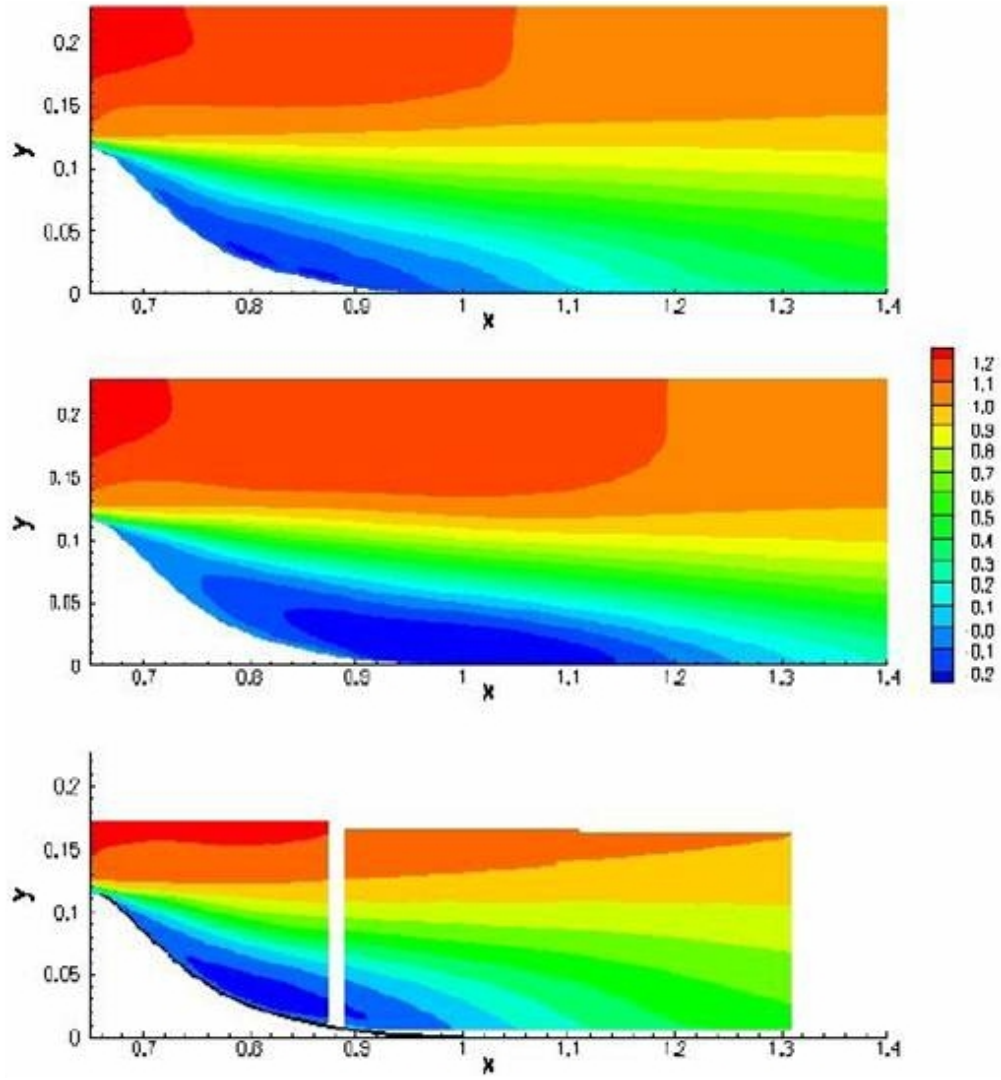


Figure 58: Time-mean streamwise velocity contours for the oscillating blowing/suction case: LES (top), RANS (middle), experiment (bottom).

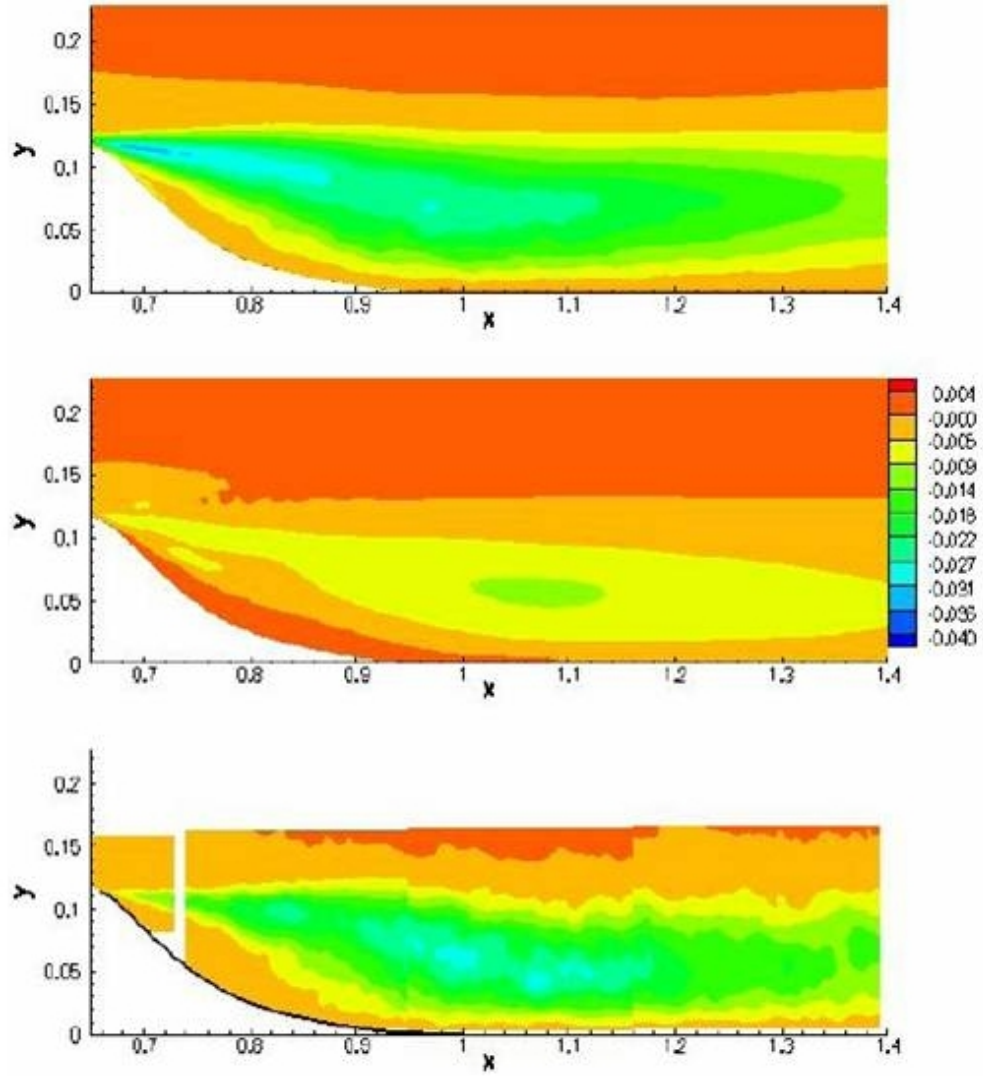


Figure 59: Time-mean Reynolds stress contours for the baseline case: LES (top), RANS (middle), experiment (bottom).

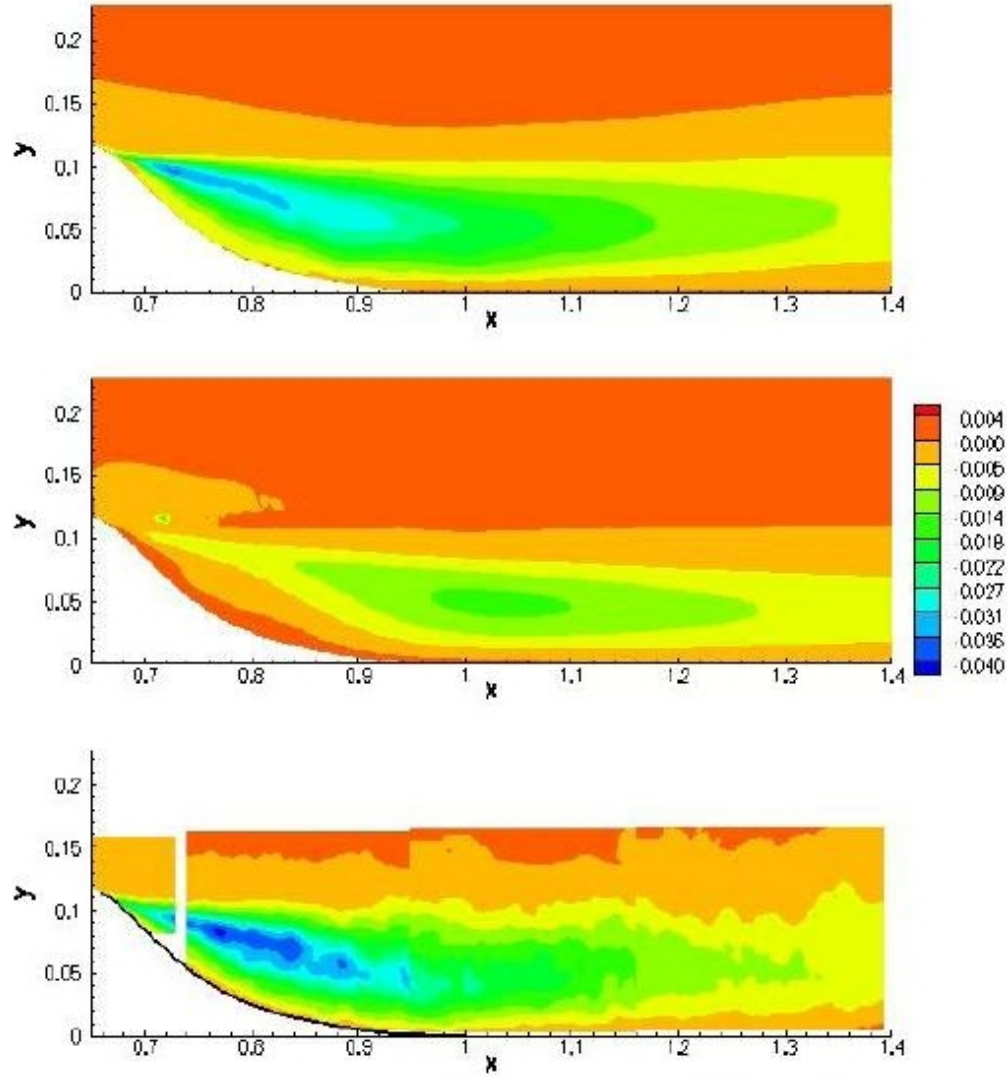


Figure 60: Time-mean Reynolds stress contours for the suction case: LES (top), RANS (middle), experiment (bottom).

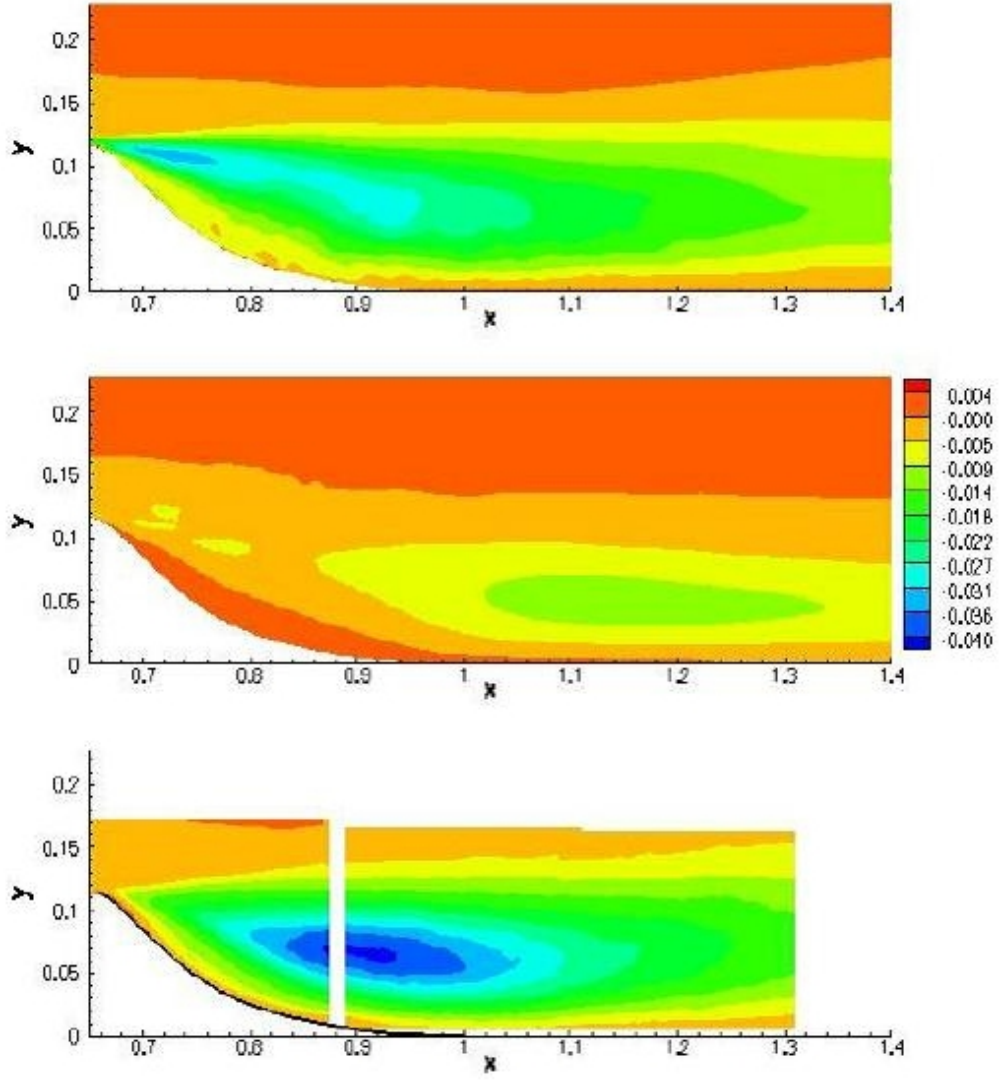


Figure 61: Time-mean Reynolds stress contours for the oscillating blowing/suction case: LES (top), RANS (middle), experiment (bottom).

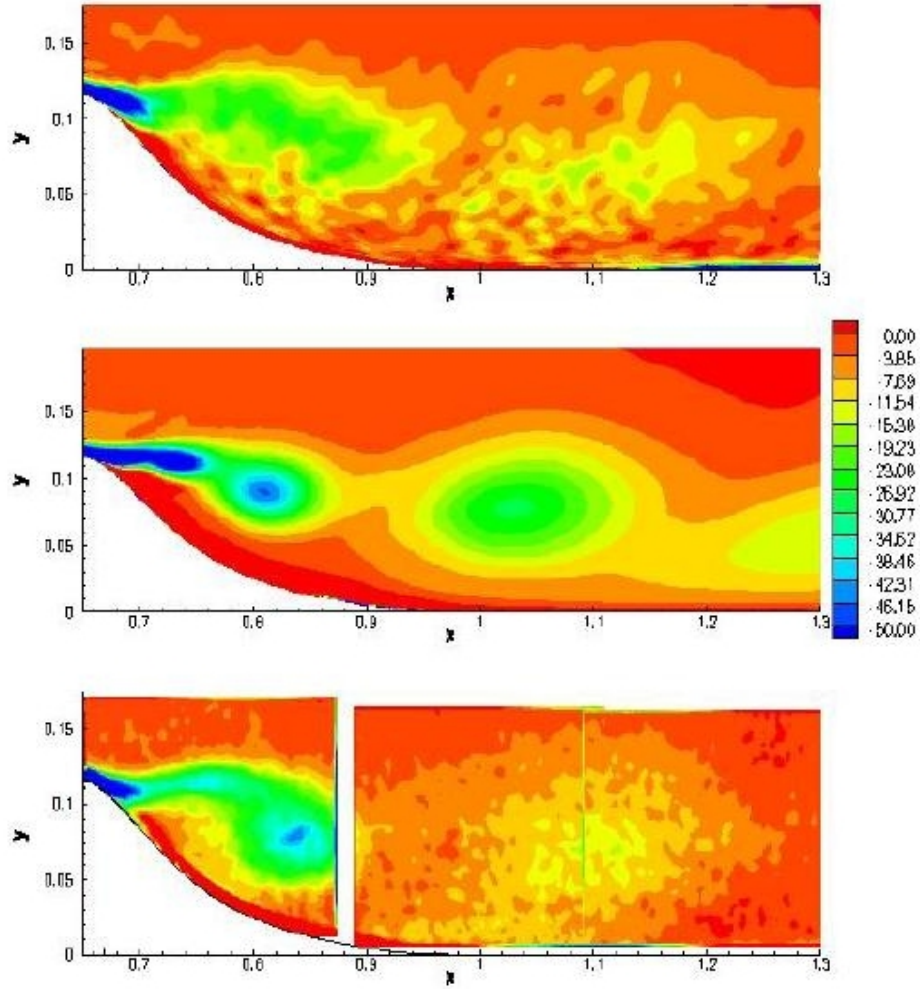


Figure 62: Phase-averaged spanwise vorticity contours at $\Theta=0$ deg for the oscillating blowing/suction case: LES (top), RANS (middle), experiment (bottom).

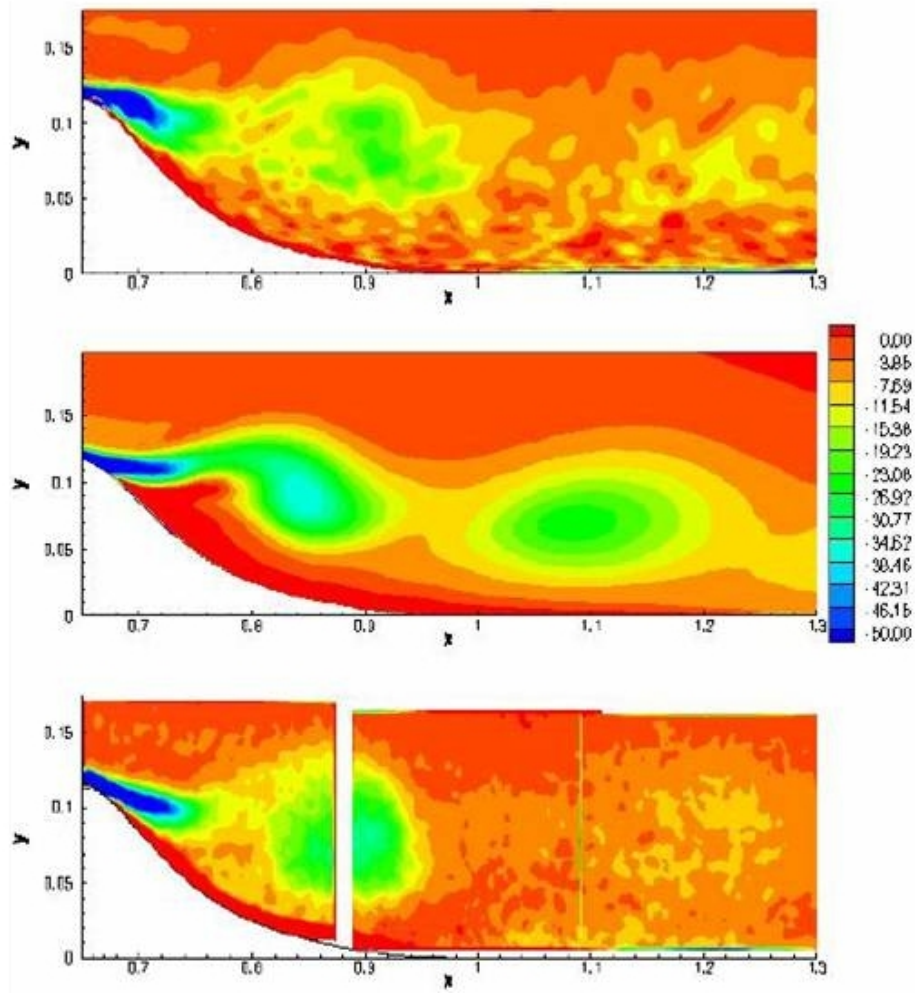


Figure 63: Phase-averaged spanwise vorticity contours at $\Theta=90$ deg for the oscillating blowing/suction case: LES (top), RANS (middle), experiment (bottom).

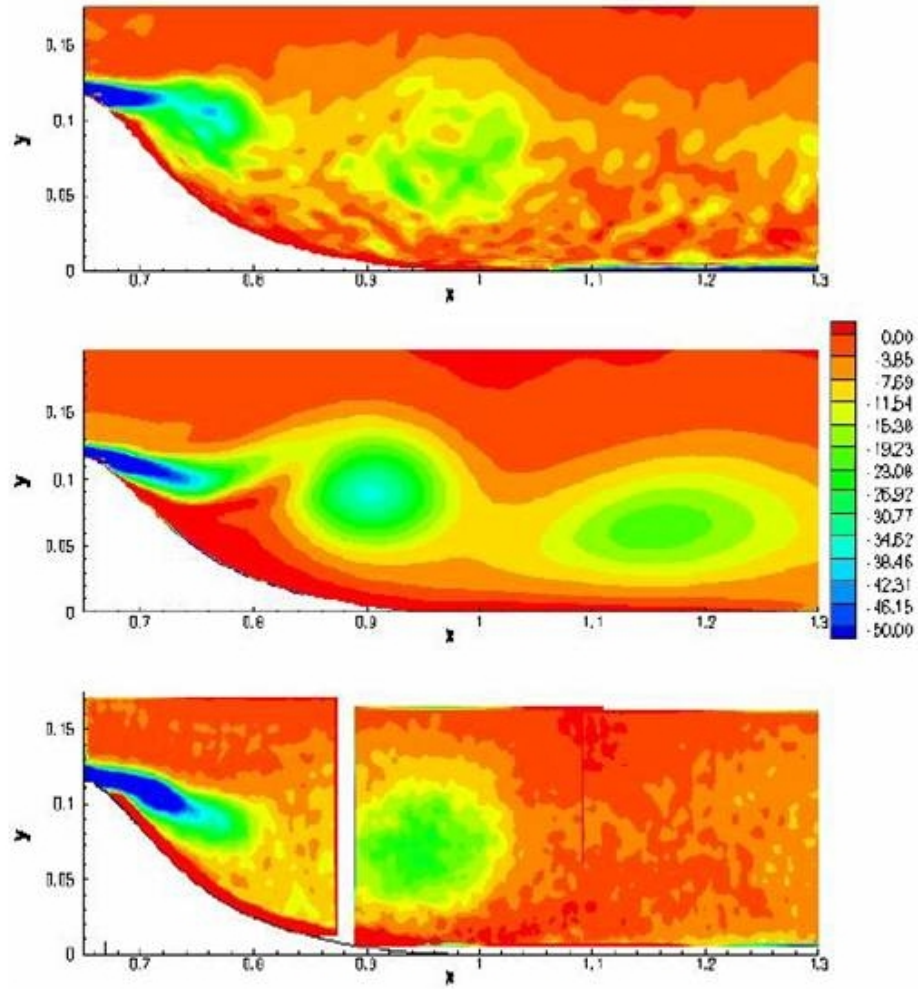


Figure 64: Phase-averaged spanwise vorticity contours at $\Theta=180$ deg for the oscillating blowing/suction case: LES (top), RANS (middle), experiment (bottom).

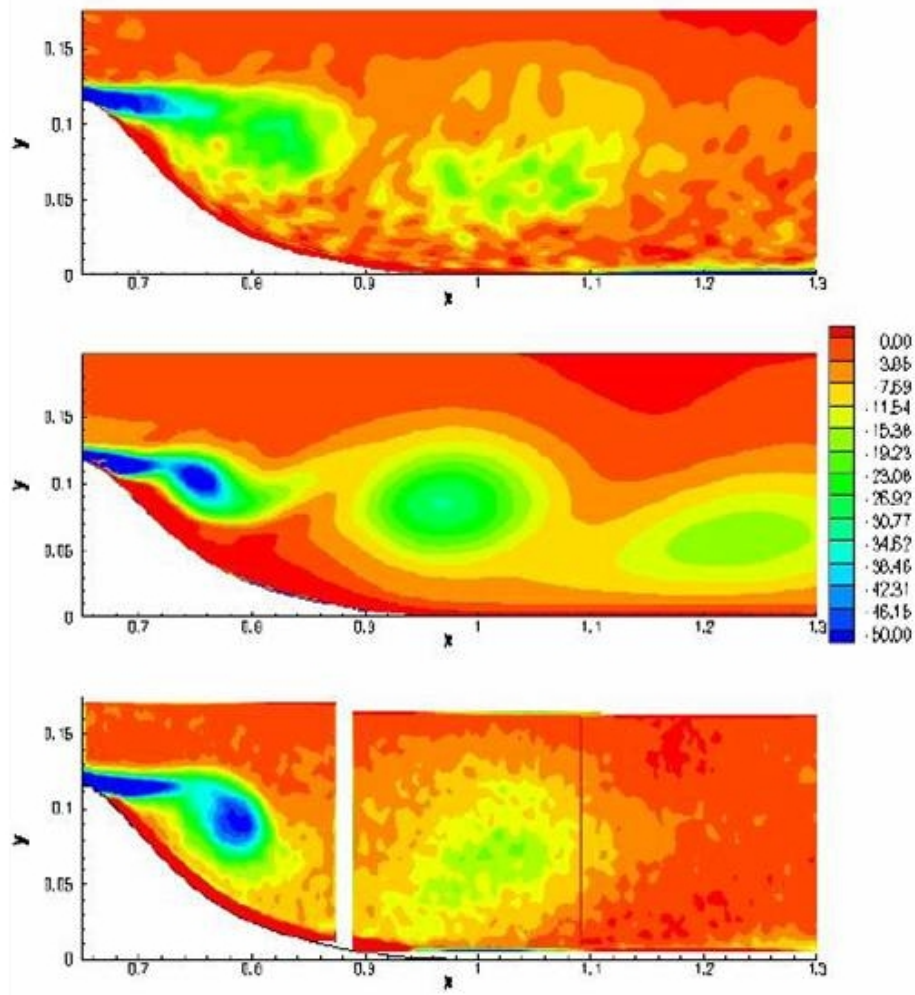


Figure 65: Phase-averaged spanwise vorticity contours at $\Theta=270$ deg for the oscillating blowing/suction case: LES (top), RANS (middle), experiment (bottom).

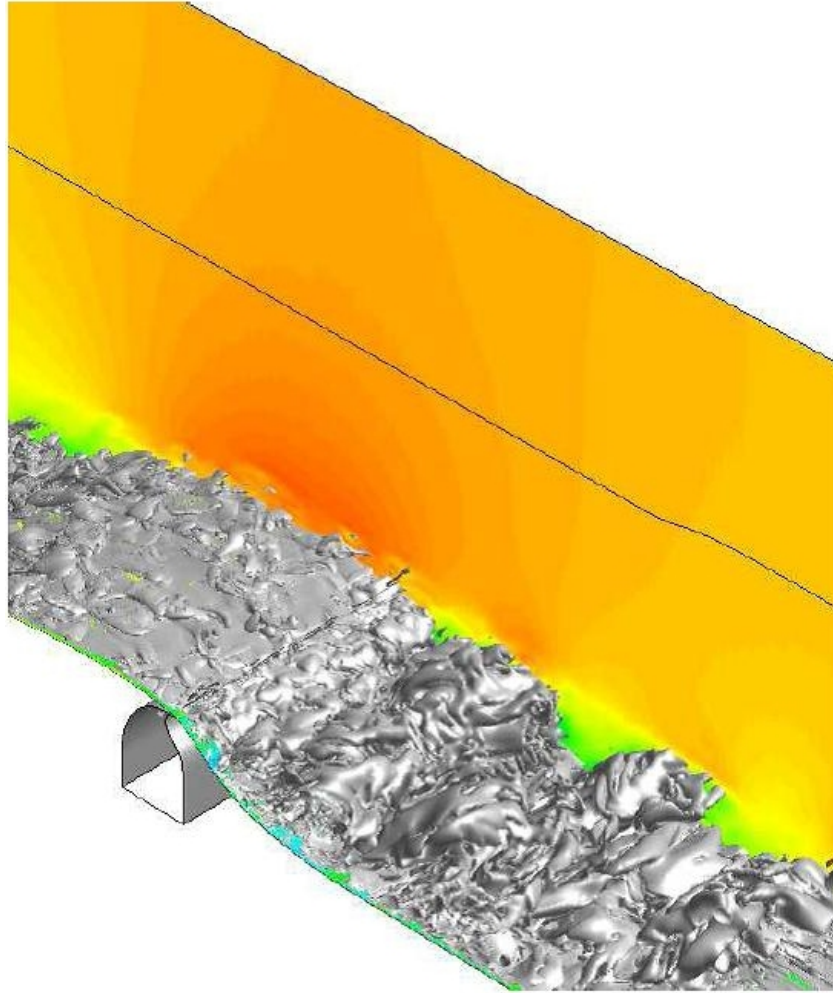


Figure 66: Instantaneous contours of streamwise velocity and iso-surface of vorticity magnitude for the oscillating blowing/suction case.

10. References

- [1] Speziale, C. G., “Turbulence Modeling for Time-Dependent RANS and VLES: A Review,” *AIAA Journal*, Vol. 41, No. 2, Feb. 1998, pp. 173–184.
- [2] Nichols, R. H. and Nelson, C. C., “Application of Hybrid RANS/LES Turbulence Models,” AIAA Paper 2003-0083, Jan. 2003.
- [3] Nelson, C. C. and Nichols, R. H., “Evaluation of Hybrid RANS/LES Turbulence Models Using an LES Code,” AIAA Paper 2003-3552, Jun. 2003.
- [4] Beam, R. and Warming, R., “An Implicit Factored Scheme for the Compressible Navier-Stokes Equations,” *AIAA Journal*, Vol. 16, No. 4, Apr. 1978, pp. 393–402.
- [5] Lele, S. A., “Compact Finite Difference Schemes with Spectral-like Resolution,” *Journal of Computational Physics*, Vol. 103, No. 1, Nov. 1992, pp. 16–42.
- [6] Gaitonde, D., Shang, J. S., and Young, J. L., “Practical Aspects of High-Order Accurate Finite-Volume Schemes for Electromagnetics,” AIAA Paper 97-0363, Jan. 1997.
- [7] Sherer, S. E., “Further Analysis of High-Order Overset Grid Method with Applications,” AIAA Paper 2003-3839, Jun. 2003.
- [8] Sherer, S. E. and Visbal, M. R., “Multi-Resolution Implicit Large Eddy Simulations Using a High-Order Overset-Grid Approach,” *International Journal for Numerical Methods in Fluids*, Vol. 55, Mar. 2007, pp. 455–482.
- [9] Gordnier, R. E. and Visbal, M. R., “Numerical Simulation of Delta-Wing Roll,” AIAA Paper 93-0554, Jan. 1993.
- [10] Jameson, A., Schmidt, W., and Turkel, E., “Numerical Solutions of the Euler Equations by Finite Volume Methods Using Runge-Kutta Time Stepping Schemes,” AIAA Paper 81-1259, Jun. 1981.
- [11] Pulliam, T. H., “Artificial Dissipation Models for the Euler Equations,” *AIAA Journal*, Vol. 24, No. 12, Dec. 1986, pp. 1931–1940.
- [12] Pulliam, T. H. and Chaussee, D. S., “A Diagonal Form of an Implicit Approximate-Factorization Algorithm,” *Journal of Computational Physics*, Vol. 39, No. 2, Feb. 1981, pp. 347–363.
- [13] Visbal, M. R. and Gaitonde, D. V., “High-Order-Accurate Methods for Complex Unsteady Subsonic Flows,” *AIAA Journal*, Vol. 37, No. 10, Oct. 1999, pp. 1231–1239.
- [14] Gaitonde, D. and Visbal, M. R., “High-Order Schemes for Navier-Stokes Equations: Algorithm and Implementation into FDL3DI,” Technical Report AFRL-VA-WP-TR-1998-3060, Air Force Research Laboratory, Wright-Patterson AFB, OH, Aug. 1998.
- [15] Visbal, M. R. and Gaitonde, D. V., “On the Use of High-Order Finite-Difference Schemes on Curvilinear and Deforming Meshes,” *Journal of Computational Physics*, Vol. 181, No. 2, Sep. 2002, pp. 155–185.
- [16] Visbal, M. R. and Gaitonde, D. V., “Very High-Order Spatially Implicit Schemes for Computational Acoustics on Curvilinear Meshes,” *Journal of Computational Acoustics*, Vol. 9, No. 4, Dec. 2001, pp. 1259–1286.
- [17] Thomas, P. D. and Lombard, S. K., “Geometric Conservation Law and Its Application to Flow Computations on Moving Grids,” *AIAA Journal*, Vol. 17, No. 10, Oct. 1979, pp. 1030–1037.
- [18] Visbal, M. R. and Rizzetta, D. P., “Large-Eddy Simulation on Curvilinear Grids Using Compact Differencing and Filtering Schemes,” *Journal of Fluids Engineering*, Vol. 124, No. 4, Dec. 2002, pp. 836–847.

- [19] Steger, J. L., Dougherty, F. C., and Benek, J. L., "A Chimera Grid Scheme," *Advances in Grid Generation*, edited by K. Ghia and U. Ghia, Vol. 5, The American Society of Mechanical Engineers, New York, NY, 1983, pp. 59–69.
- [20] Gaitonde, D. V. and Visbal, M. R., "Pade-Type Higher-Order Boundary Filters for the Navier-Stokes Equations," *AIAA Journal*, Vol. 38, No. 11, Nov. 2000, pp. 2103–2112.
- [21] Message Passing Interface Forum, "MPI: A Message-Passing Interface Standard," Computer Science Department Technical Report CS-94-230, University of Tennessee, Knoxville, TN, Apr. 1994.
- [22] Suhs, N. E., Rogers, S. E., and Dietz, W. E., "PEGASUS 5: An Automated Preprocessor for Overset-Grid Computational Fluid Dynamics," *AIAA Journal*, Vol. 41, No. 6, Jun. 2003, pp. 1037–1045.
- [23] Sherer, S. E. and Visbal, M. R., "Automated Preprocessing Tools for Use with a High-Order Overset-Grid Algorithm," AIAA Paper 2006-1147, Jan. 2006.
- [24] Visbal, M. R., Morgan, P. E., and Rizzetta, D. P., "An Implicit LES Approach Based on High-Order Compact Differencing and Filtering Schemes," AIAA Paper 2003-4098, Jun. 2003.
- [25] Fureby, C. and Grinstein, F. F., "Monotonically Integrated Large Eddy Simulation," *AIAA Journal*, Vol. 37, No. 5, May 1999, pp. 544–556.
- [26] Stolz, S. and Adams, N., "An Approximate Deconvolution Procedure for Large-Eddy Simulation," *Physics of Fluids*, Vol. 11, No. 7, Jul. 1999, pp. 1699–1701.
- [27] Mathew, J., Lechner, R., Foyi, H., Sesterhenn, J., and Friedrich, R., "An Explicit Filtering Method for Large Eddy Simulation of Compressible Flows," *Physics of Fluids*, Vol. 15, No. 8, Aug. 2003, pp. 2279–2289.
- [28] Gordnier, R. E., "Computation of Delta-Wing Roll Maneuvers," *Journal of Aircraft*, Vol. 32, No. 3, May 1995, pp. 486–492.
- [29] Visbal, M. R., "Computational Study of Vortex Breakdown on a Pitching Delta Wing," AIAA Paper 93-2974, Jul. 1993.
- [30] Visbal, M., Gaitonde, D., and Gogineni, S., "Direct Numerical Simulation of a Forced Transitional Plane Wall Jet," AIAA Paper 98-2643, Jun. 1998.
- [31] Rizzetta, D. P., Visbal, M. R., and Stanek, M. J., "Numerical Investigation of Synthetic-Jet Flowfields," *AIAA Journal*, Vol. 37, No. 8, Aug. 1999, pp. 919–927.
- [32] Rizzetta, D. P. and Visbal, M. R., "Direct Numerical Simulation of Flow Past an Array of Distributed Roughness Elements," *AIAA Journal*, Vol. 45, No. 8, Aug. 2007, pp. 1967–1976.
- [33] Gaitonde, D. V., Visbal, M. R., and Roy, S., "Control of Flow Past a Wing Section with Plasma-Based Body Forces," AIAA Paper 2005-5302, Jun. 2005.
- [34] Visbal, M. R. and Gaitonde, D. V., "Control of Vortical Flows Using Simulated Plasma Actuators," AIAA Paper 2006-0505, Jan. 2005.
- [35] Visbal, M. R., Gaitonde, D. V., and Roy, S., "Control of Transitional and Turbulent Flows Using Plasma-Based Actuators," AIAA Paper 2006-3230, Jun. 2006.
- [36] Rizzetta, D. P. and Visbal, M. R., "Numerical Investigation of Plasma-Based Flow Control for a Transitional Highly-Loaded Low-Pressure Turbine," AIAA Paper 2007-938, Jan. 2007.
- [37] Rizzetta, D. P. and Visbal, M. R., "Numerical Investigation of Transitional Flow Through a Low-Pressure Turbine Cascade," AIAA Paper 2003-3587, Jun. 2003.

- [38] Rizzetta, D. P., Visbal, M. R., and Blaisdell, G. A., "A Time-Implicit High-Order Compact Differencing and Filtering Scheme for Large-Eddy Simulation," *International Journal for Numerical Methods in Fluids*, Vol. 42, No. 6, Jun. 2003, pp. 665–693.
- [39] Rizzetta, D. P. and Visbal, M. R., "Application of Large-Eddy Simulation to Supersonic Compression Ramps," *AIAA Journal*, Vol. 40, No. 8, Aug. 2002, pp. 1574–1581.
- [40] Rizzetta, D. P. and Visbal, M. R., "Large-Eddy Simulation of Supersonic Cavity Flowfields Including Flow Control," *AIAA Journal*, Vol. 41, No. 8, Aug. 2003, pp. 1452–1462.
- [41] Morgan, P., Visbal, M., and Rizzetta, D., "A Parallel Overset Grid High-Order Flow Solver for Large Eddy Simulation," *Journal of Scientific Computing*, Vol. 29, No. 2, Nov. 2006, pp. 165–297.
- [42] Smagorinsky, J. S., "General Circulation Experiments with the Primitive Equations," *Monthly Weather Review*, Vol. 91, No. 3, Mar. 1963, pp. 99–165.
- [43] Germano, M., Piomelli, U., Moin, P., and Cabot, W. H., "A Dynamic Subgrid Scale Eddy Viscosity Model," *Physics of Fluids A*, Vol. 3, No. 7, Jul. 1991, pp. 1760–1765.
- [44] Rizzetta, D. P. and Visbal, M. R., "Large-eddy Simulation of Supersonic Boundary-layer Flow by a High-order Method," *International Journal of Computational Fluid Dynamics*, Vol. 18, No. 1, Jan. 2004, pp. 15–27.
- [45] Roth, J. R., "Aerodynamic Flow Acceleration Using Paraelectric and Peristaltic Electrohydrodynamic Effects of a One Atmosphere Uniform Glow Discharge Plasma," *Physics of Plasmas*, Vol. 10, No. 5, May 2003, pp. 2117–2128.
- [46] Roth, J. R., Sin, H., and Madham, R. C. M., "Flow Re-attachment and Acceleration by Paraelectric and Peristaltic Electrohydrodynamic (EHD) Effects," *AIAA Paper 2003-0531*, Jan. 2003.
- [47] Shyy, W., Jayaraman, B., and Anderson, A., "Modeling of Glow Discharge-Induced Fluid Dynamics," *Journal of Applied Physics*, Vol. 92, No. 11, Dec. 2002, pp. 6434–6443.
- [48] Corke, T. C. and Post, M. L., "Overview of Plasma Flow Control: Concepts, Optimization, and Applications," *AIAA Paper 2005-0563*, Jan. 2005.
- [49] Stanek, M. J., Raman, G., Kibens, V., Ross, J. A., Odedra, J., and Peto, J. W., "Control of Cavity Resonance Through Very High Frequency Forcing," *AIAA Paper 2000-1905*, Jun. 2000.
- [50] Ross, J. A., Peto, J. W., and Odedra, J., "Active Control of Cavity Resonance - Investigation of Acoustic Suppression Methods," *WAIS Report 257*, Defense Evaluation Research Agency, Nov. 1999.
- [51] Raman, G. Kibens, V., "High Frequency Excitation Cavity Experiments," *Boeing Report 00P0064*, The Boeing Company, Apr. 2000.
- [52] Odedra, J., Peto, J. W., and Ross, J. A., "Active Control of Cavity Resonance - Investigation of Acoustic Suppression Methods - Phase 2," *WAIS Report 260*, Defense Evaluation Research Agency, Jun. 2001.
- [53] Rizzetta, D. P. and Visbal, M. R., "Large-Eddy Simulation of Supersonic Cavity Flowfields Including Flow Control," *AIAA Paper 2002-2853*, Jun. 2002.
- [54] Rossiter, J. E. and Kurn, A. G., "Wind Tunnel Measurements of the Unsteady Pressures In and Behind a Bomb Bay(Camberra)," *Aeronautical Research Council Report CP 728*, Ministry of Aviation, Oct. 1962.
- [55] Rossiter, J. E., "Wind Tunnel Measurements on the Flow Over Rectangular Cavities at Subsonic and Transonic Speeds," *Aeronautical Research Council Report Reports and Memoranda 3438*, Ministry of Aviation, Oct. 1964.
- [56] Rockwell, D., "Three-Dimensional Flow Structures on Delta Wings at High Angles of Attack: Experimental Concepts and Issues," *AIAA Paper 93-0550*, Jan. 1993.

- [57] Gursul, I., "Review of Unsteady Vortex Flows over Slender Delta Wings," *Journal of Aircraft*, Vol. 42, No. 2, Mar.-Apr. 2005, pp. 299–319.
- [58] Visbal, M. R. and Gordnier, R. E., "On the Structure of the Shear Layer Emanating from a Swept Leading Edge at Angle of Attack," AIAA Paper 2003-4016, Jun. 2003.
- [59] Visbal, M. R., "Computational and Physical Aspects of Vortex Breakdown on Delta Wings," AIAA Paper 95-0585, Jan. 1995.
- [60] Riley, A. J. and Lowson, M. V., "Development of a Three-Dimensional Free Shear Layer," *Journal of Fluid Mechanics*, Vol. 369, Aug. 1998, pp. 49–89.
- [61] Mitchell, A., Molton, P., Barberis, D., and Delery, J., "Vortical Substructures in the Shear Layers Forming Leading-Edge Vortices," AIAA Paper 2001-2424, Jun. 2001.
- [62] Gordnier, R. E. and Visbal, M. R., "Unsteady Vortex Structure over a Delta Wing," *Journal of Aircraft*, Vol. 31, No. 1, Jan.-Feb. 1994, pp. 243–248.
- [63] Bons, J. P., Sondergaard, R., and Rivir, R. B., "Control of Low-Pressure Turbine Separation Using Vortex Generator Jets," AIAA Paper 99-0367, Jan. 1999.
- [64] Bons, J. P., Sondergaard, R., and Rivir, R. B., "Turbine Separation Control Using Pulsed Vortex Generator Jets," *Journal of Turbomachinery*, Vol. 123, No. 2, Apr. 2001, pp. 198–206.
- [65] Bons, J. P., Sondergaard, R., and Rivir, R. B., "The Fluid Dynamics of LPT Blade Separation Control Using Pulsed Jets," *Journal of Turbomachinery*, Vol. 124, No. 1, Jan. 2002, pp. 77–85.
- [66] Sondergaard, R., Rivir, R. B., and Bons, J. P., "Control of Low-Pressure Turbine Separation Using Vortex Generator Jets," *Journal of Propulsion and Power*, Vol. 18, No. 4, Jul.-Aug. 2002, pp. 889–895.
- [67] Sondergaard, R., Bons, J. P., Sucher, M., and Rivir, R. B., "Reducing Low-Pressure Turbine Stage Blade Count Using Vortex Generator Jet Separation Control," ASME Paper GT-2002-30602, Jun. 2002.
- [68] Rizzetta, D. P. and Visbal, M. R., "Numerical Study of Active Flow Control for a Transitional Highly-Loaded Low-Pressure Turbine," AIAA Paper 2005-5020, Jun. 2005.
- [69] Rizzetta, D. P. and Visbal, M. R., "Numerical Study of Active Flow Control for a Transitional Highly-Loaded Low-Pressure Turbine," *Journal of Fluids Engineering*, Vol. 128, No. 5, Sep. 2006, pp. 956–967.
- [70] Rizzetta, D. P. and Visbal, M. R., "Simulation of Plasma-Based Flow Control Strategies for Transitional Highly-Loaded Low-Pressure Turbines," AIAA Paper 2007-4216, Jun. 2007.
- [71] Rizzetta, D. P. and Visbal, M. R., "Numerical Investigation of Plasma-Based Flow Control for Transitional Highly Loaded Low-Pressure Turbine," *AIAA Journal*, Vol. 45, No. 10, Oct. 2007, pp. 2554–2564.
- [72] Rizzetta, D. P. and Visbal, M. R., "Numerical Simulation of Separation Control for Transitional Highly-Loaded Low-Pressure Turbines," *AIAA Journal*, Vol. 43, No. 9, Sep. 2005, pp. 1958–1967.
- [73] Rizzetta, D. P. and Visbal, M. R., "Numerical Simulation of Separation Control for a Highly-Loaded Low-Pressure Turbine," AIAA Paper 2004-2204, Jun.-Jul. 2004.
- [74] Rumsey, C., Gatski, T., Sellers, W., Vatsa, V., and Viken, S., "Summary of the 2004 CFD Validation Workshop on Synthetic Jets and Turbulent Separation Control," AIAA Paper 2004-2217, Jun. 2004.
- [75] Greenblatt, D., Paschal, K., Yao, C., Harris, J., Schaeffler, N., and Washburn, A., "A Separation Control CFD Validation Test Case, Part 1: Baseline and Steady Suction," AIAA Paper 2004-2220, Jun. 2004.
- [76] Greenblatt, D., Paschal, K., Yao, C., and Harris, J., "A Separation Control CFD Validation Test Case, Part 2: Zero Efflux Oscillatory Blowing," AIAA Paper 2005-0485, Jan. 2005.
- [77] Morgan, P. E., Rizzetta, D. P., and Visbal, M. R., "Large-Eddy Simulation of Flow Over a Wall-Mounted Hump," AIAA Paper 2005-484, Jan. 2005.

- [78] Morgan, P. E., Rizzetta, D. P., and Visbal, M. R., “Large-Eddy Simulation of Separation Control for Flow Over a Wall-Mounted Hump,” AIAA Paper 2005-5017, Jun. 2005.
- [79] Morgan, P. E., Rizzetta, D. P., and Visbal, M. R., “Large-Eddy Simulation of Separation Control for Flow Over a Wall-Mounted Hump,” *AIAA Journal*, Vol. 45, No. 11, Nov. 2007, pp. 2643–2660.
- [80] Morgan, P. E., Rizzetta, D. P., and Visbal, M. R., “Numerical Investigation of Separation Control for Flow Over a Wall-Mounted Hump,” AIAA Paper 2004-2510, Jun. 2004.
- [81] Visbal, M. R. and Gaitonde, D. V., “Shock Capturing Using Compact-Differencing-Based Methods,” AIAA Paper 2005-1265, Jan. 2005.
- [82] Croker, B. A. and Gaitonde, D. V., “A Filter Based Artificial Viscosity Method for Discontinuous Flows,” AIAA Paper 2007-4193, Jun. 2007.

List of Symbols

a, b, c	= coefficients of explicit terms in the compact difference formula
a_n	= coefficients of explicit terms in the compact filter formula
A	= duty cycle amplitude function
B	= nondimensional turbine inter-blade spacing, 4/3
C_p	= pressure coefficient
C_w	= integrated wake total pressure loss coefficient
d	= cavity depth
D_c	= plasma scale parameter
e_c	= electron charge, 1.6×10^{-19} coulomb
\mathbf{E}	= nondimensional electric field vector
E	= total specific energy
E_{k_z}, E_ω	= nondimensional turbulent kinetic energy wave number and frequency spectra
E_r	= reference electric field magnitude
E_x, E_y, E_z	= nondimensional components of the electric field vector
f	= dimensional imposed actuator pulsing frequency, Hz
$\mathbf{F}, \mathbf{G}, \mathbf{H}$	= inviscid vector fluxes
$\mathbf{F}_v, \mathbf{G}_v, \mathbf{H}_v$	= viscous vector fluxes
I, J, K	= grid indices of computational coordinates ξ, η, ζ
I_p, J_p, K_p	= indices of donor point stencil
\mathcal{J}	= Jacobian of the coordinate transformation
l	= characteristic length for nondimensionalization
M	= Mach number
p	= nondimensional static pressure
P_{ti}, P_{to}	= nondimensional inlet and outlet total pressure
Pr	= Prandtl number, 0.73 for air
q_c	= nondimensional charge density
q_i	= turbine blade inflow velocity magnitude
\mathbf{Q}	= vector of dependent variables
Q_i	= components of the heat flux vector
Re	= reference Reynolds number, $\rho_\infty u_\infty l / \mu_\infty$
R_n	= R_i, R_j, R_k - interpolation coefficients
s	= nondimensional local span
S	= scaled spatial coordinate for wave number analysis
\mathbf{S}	= source vector
t	= nondimensional time
t_d	= portion of fundamental period over which actuator is active
t_p	= nondimensional actuator fundamental period
T	= nondimensional static temperature
\mathcal{T}	= spectral transfer function
u, v, w	= nondimensional Cartesian velocity components in the x, y, z directions
u_1, u_2, u_3	= u, v, w
U, V, W	= contravariant velocity components
x, y, z	= nondimensional Cartesian coordinates in the streamwise, vertical, and spanwise directions
x_1, x_2, x_3	= x, y, z
α, β	= coefficients of implicit terms in the compact difference formula
α_f, β_f	= coefficients of implicit terms in the compact filter formula
α_i, α_o	= turbine inflow and outflow blade angles
γ	= specific heat ratio, 1.4 for air
δ_{ij}	= Kronecker delta function
$\delta_{\xi 2}, \delta_{\eta 2}, \delta_{\zeta 2}$	= 2nd-order explicit and nth-order compact finite-difference operators in ξ, η, ζ
$\delta_{\xi n}, \delta_{\eta n}, \delta_{\zeta n}$	= boundary-layer thickness

ΔQ	$= Q^{p+1} - Q^p$
Δ_n	$= \Delta_i, \Delta_j, \Delta_k$ - interpolation offsets
Δt	$=$ time step size
Δx	$=$ spatial step size
θ_0	$=$ boundary-layer momentum thickness
Θ	$=$ angle for phase averaging
μ	$=$ nondimensional molecular viscosity coefficient
ξ, η, ζ	$=$ nondimensional body-fitted computational coordinates
$\xi_t, \xi_x, \xi_y, \xi_z,$ $\eta_t, \eta_x, \eta_y, \eta_z,$ $\zeta_t, \zeta_x, \zeta_y, \zeta_z$	$=$ metric coefficients of the coordinate transformation
ρ	$=$ nondimensional fluid density
ρ_c	$=$ electron charge number density, $1 \times 10^{11}/\text{cm}^3$
σ	$=$ order-of-accuracy of interpolation formula
τ_{ij}	$=$ components of the viscous stress tensor
ϕ	$=$ general function
ω	$=$ dimensional or nondimensional frequency
Ω	$=$ scaled spatial wave number
Ω'	$=$ modified scaled spatial wave number

Subscripts

b	$=$ breakdown location
i	$=$ grid point index number
m	$=$ Fourier mode number
max	$=$ maximum value
min	$=$ minimum value
p	$=$ receiving interpolation point
n	$=$ numerical approximation
∞	$=$ dimensional reference value

Superscripts

n	$=$ time level
p	$=$ subiteration level
\sim	$=$ Fourier component
\cdot	$= d/dS$
$\hat{}$	$=$ filtered value
\sim	$=$ interpolated value
—	$=$ time-mean quantity
$'$	$=$ fluctuating component